# Magnetic Properties of Arrays of Magnetite Particles Produced by the Method of Electron Beam Lithography (ELB)

by

James Gagwane King

Doctor of Philosophy

University of Edinburgh

August 1996

# DECLARATION

This thesis has been composed solely by myself. The work presented is my own unless otherwise acknowledged.

# ABSTRACT

This study involves the production of arrays of parallelepiped magnetite particles in the size range 0.1 - 1 μm. This was achieved by utilising electron beam lithography techniques which are often employed in the design of semi-conductor devices. These particles are required in order to understand the mechanism of reversal of magnetisation for pseudo-single-domain (PSD) particles important to paleomagnetic studies. The samples used by previous researchers are magnetite powders. In such samples, despite attempts to disperse the particles onto non-magnetic matrix, there is no way of eliminating particle clumping, and magnetostatic interaction.

Low temperature magnetic measurements obtained using samples of cubic arrays of magnetite particles shows that the effect of particle clumping is to increase the amount of saturation isothermal remanence (SIRM) lost at the Verwey transition. The dependence of SIRM lost at the Verwey transition on particle size in the PSD size range, is consistent with the vortex domain structure predicted from unconstrained 3-D micromagnetic studies. The results shows that 'true' magnetic memory is a stress related phenomenon.

Magnetic properties of cubic arrays of magnetite particles measured at room temperature are not consistent with the mechanism of magnetic reversal by coherent rotation of atomic magnetic moments, but are generally in good agreement with that of vortex nucleation and propagation. The method of domain classification using the coercivity ratio often used in rock magnetism, is shown to be not useful in classifying PSD in the submicron size range.

Magnetic properties of rectangular parallelepiped magnetite particles are more complex than expected from the simple demagnetisation shape anisotropy contribution. The effects of decreasing inter-particle spacing of chains of elongated particles is to increase the coercivity of the sample. This observation is particularly important to the interpretation of paloemagnetic studies of magnetite/non-magnetic matrix inter-growth and as well fossils of magnetotactic bacteria.

# Acknowledgements

I would like to thank my supervisor, Dr. Wyn Williams for extending his good links with various universities to me. Thus making it possible for me to use their highly specialised equipment which was vital to this study. I also thank him for the advice and encouragement throughout this study.

In the initial part of this study, I used thin film deposition equipment at the Department of Physics (Heriotwatt University), and many thanks to Dr. John Wilson. I carried out electron beam lithography experiments at the Department of Electronics and Electrical Engineering (EEE) of the University of Glasgow. I would like to thank Prof. Wilkinson of EEE department for allowing me to use their equipment, for making it possible for me to attend a 2 weeks course on the introduction to electron beam lithography techniques, and for the helpful discussions and support throughout the duration of the experimental work. I also benefited from discussions with Drs Steve Thoms and Douglas MacIntyre and as well all the members of the nanostructures group of the EEE department. Ashish Mildla of EEE department and Dr. Babak then at Physics and Astronomy Department, (Glasgow, University), kindly provided me with the silicon membranes.

Domain observation and further thin film deposition experiments were carried out at the department of Physics and Astronomy (Glasgow University). I would like to thank Prof. John Chapman, Dr Stephen McVitie and Mr Donald McDonald for the help they provided in making these experiments possible. Room temperature magnetic measurements were mainly carried out using an AGFM at the University of North Wales and I would like to thank Drs Kevin O'Grady, Puerto Morales and Mr John Cambridge for the help they provided during the duration of these experiments. Dr. Morales also kindly provided me with acircular narrow size distribution maghemite powder samples, which I later converted to magnetite and use in part of this study.

I would also like to thank Drs Steve Elphick and Nicholas Odling of Geology and Geophysics (Edinburgh University) for their help in making the annealing experiments possible. Low temperature magnetic measurements were done using the SQUID magnetometer at the Department of Chemistry (Edinburgh University), and many thanks to Drs Andrew Harrison and Gavin

Whittaker. Thanks also to Adrian Muxworthy (Oxford University) for interesting discussions during his research visits to our department.

In 1994 I benefited from using the equipment at the Institut für Allgemeine und Angewandte Geophysik, Munich, Germany. Many thanks to Dr. Franz Heider for making the trip possible and to all the members of the department for their warm hospitality. I would like to thanks the members of the Institute of Rock Magnetism, University of Minnesota for the use of their equipment during my research visit to their institution.

Finally I would like to thank MmaWandipa & kids, my parents in Nkange and the rest of the family members for their encouragement throughout this study.

The sponsorship provided by the University of Botswana and later the British Overseas Development Agency, is highly appreciated. The research study was supported by an EPSERC grant.

# Contents

# List of abbreviations

| | |
|---|---|
| PSD | pseudo-single-domain |
| SIRM | saturation isothermal remanent magnetisation |
| AGFM | alternating gradient force magnetometer |
| SQUID | superconducting quantum interference device |
| $m_{orbit}$ | orbital magnetic moment |
| $m_{spin}$ | spin magnetic moment |
| e | electron charge |
| h | Plank's constant |
| $m_l$ | magnetic quantum number |
| $m_s$ | spin quantum number |
| $\mu_B$ | Bohr magneton |
| $\mathbf{S}_i$ and $\mathbf{S}_j$ | electron spin vectors |
| H | magnetic field |
| **H** | magnetic field vector |
| Fe | iron |
| $E_{ex}$ | exchange energy |
| $J_E$ | exchange integral |
| $E_k$ | magnetocrystalline anisotropy energy |
| $M_S$ | spontaneous (or saturation) magnetisation |
| $K_1$ | first magnetocrystalline anisotropy constant |
| $K_2$ | second magnetocrystalline anisotropy constant |
| $E_\sigma$ | magnetoelastic energy |
| $\lambda_s$ | magnetostriction constant |
| $\sigma$ | stress |
| $E_{ext}$ | external field energy |
| $\mu_o$ | permeability of free space |
| $E_D$ | magnetostatic energy |
| $\mathbf{H}_D$ | resultant field vector due to the contribution of all atomic moments in the volume of a particle |
| $E_T$ | total magnetic energy |
| SD | single-domain |
| MD | multidomain |
| EBL | electron beam lithography |

| | |
|---|---|
| TEM | transmission electron microscope |
| XRD | X-ray diffraction |
| Fe | iron |
| $Fe_2O_3$ | hematite |
| $Fe_3O_4$ | magnetite |
| PMMA | poly methyl methacrylate |
| SEM | scanning electron microscope |
| $Fe_2SiO_4$ | Fayalite |
| CATS | computer aided transcription system |
| WAM | wavemaker - a computer program |
| $Si_3N_4$ | silicon nitride |
| MFM | magnetic force magnetometer |
| **B** | magnetic induction |
| SPM | superparamagnetism |
| $T_v$ | Verwey transition temperature |
| NRM | natural remanent magnetisation |
| DC | direct current |
| $H_c$ | coercivity (or coercive force) |
| $H_{cr}$ | remanence coercivity |
| SW | Stoner and Wohlfarth theory |
| $M_r(H)$ | isothermal remanence magnetisation |
| $M_d(H)$ | demagnetisation remanence |
| af | alternating field |
| $\delta$-$Fe_2O_3$ | maghemite |
| SPM-SD | boundary between superparamagnetic domain and single-domain |
| $\tau$ | relaxation time |
| $f_o^{-1}$ | frequency factor |
| $\upsilon$ | particle volume |
| k | Boltzmann's constant |
| T | absolute temperature |
| $N_a$ | demagnetisation factor along the particle's major axis |
| $N_b$ | demagnetisation factor along the particle's minor axis |
| q | a particle's axial ratio (minor axis / major axis) |
| MiBK | an organic solution whose chemical formula is $[(CH_3)_2CHCH_2COCH_3)$ |
| IPA | isopropyl alcohol |

| | |
|---|---|
| SD-2D | boundary between single-domain and two domain structures |
| SD-PSD | boundary between single-domain and pseudo-single-domain structures |
| 3-D | three dimension |
| 1-D | one dimension |
| $CaF_2$ | calcium fluoride |
| $M_{rs}$ | saturation remanence |
| 2-D | two domain |
| MPMS2 | a magnetometer |

# Chapter 1 Introduction

## 1.1 A brief historical review of geomagnetism and rock magnetism

The lodestone (a piece of rock made of the mineral magnetite) is believed to have been used as a compass by the Chinese as early as 2500 BC. The power of this stone to attract iron was reported by the Greek philosopher Thames as early as 600 BC. The discovery of the dipole nature of the lodestone (i.e. the existence of two regions which attracted a piece of iron more strongly than the rest of the body) was made by Peregrines about 1269 AD. It was William Gilbert in 1600 AD who realised that the earth is a huge magnet and hence explained the mystery behind the success of the loadstone's use as a compass. The observation that some rocks are magnetised parallel to the direction of the Earth's magnetic field was made independently by both Delesse in 1849 and Melloni in 1855. The evidence of the geomagnetic reversal came from the studies of lava flow baked contact done by David (1904) and Brunhes (1906). It was in the late 1950's and early 1960's that a proposal long made by Wegener in 1912 that continents has drifted in geological time, was supported by magnetic evidence. Seaborne magnetic surveys of part of the North Pacific revealed strips of ocean floor alternately with normal and reverse magnetism, thus providing evidence for sea-floor spreading and plate tectonics.

It is clear from the brief historical account presented above that the mineral magnetite has played an important role in the study of magnetism in general and rock magnetism in particular. Despite the long study, the magnetic behaviour of fine particles (submicron to a few microns) of magnetite, is still not well understood. Hence the present study. In the next sections the physical basis of rock magnetism is presented.

## 1.2 Physical principles of magnetism

The observed magnetic behaviour of certain minerals can be traced to the spinning and orbiting atomic electrons. It can be shown using a semi-classical approach (e.g. Anderson et. al., 1985, pp. 434), that the orbital magnetic moment ($\boldsymbol{m}_{orbit}$) and spin magnetic moment $\boldsymbol{m}_{spin}$), of an electron are given by

$$m_{orbit} = \frac{-m_l eh}{4\pi m} \quad (1.1)$$

$$m_{spin} = \frac{-m_s eh}{2\pi m} \quad (1.2)$$

where $e$ is the electron charge, $m$ is the electron mass, $h$ is Plank's constant, $m_l$ is magnetic quantum number (an integer) and $m_s$ is spin quantum number whose value = +/- 1/2. The quantity $\frac{eh}{4\pi m}$ is known as the Bohr magneton ($\mu_B$).

### 1.2.1 Diamagnetism

Upon application of a field (H) to a material, the field interacts with the electrons in such a way that their orbital motion changes. The change in the velocity of the electron results in an induced magnetisation whose direction is opposite to that of the applied field. This phenomenon is known as diamagnetism. Since all matter contains electrons moving in orbits, diamagnetism occurs in all substances. However due to its weakness compared to other types of magnetism (which are discussed below), it cannot be observed in their presence. Examples of minerals which exhibit this behaviour include quartz, feldspar and calcite. With the exception of diamagnetism, all other magnetism results because of permanent atomic magnetic moments.

### 1.2.2 Paramagnetism

The presence or absence of atomic moments in an atom depends on its electronic structure. The type of coupling between such moments determine the type of magnetisation. In paramagnetism, the atomic moments are randomly oriented as a result of thermal agitation. It is only after the application of a sufficiently large field that the atomic moments align in the direction of the field. Upon removal of such a field, thermal agitation again randomises atomic moments and hence such material cannot have

remanent magnetisation. Examples include olivine, pyroxene, garnet, biotite and carbonates of iron and manganese.

### 1.2.3 Ferro/Ferri/Antiferro/magnetism and Imperfect ferromagnetism

In ferromagnetism there is spontaneous alignment of atomic moments in the same direction as a result of exchange interactions (equation 1.3). A schematic diagram showing the various types of magnetism is shown in Figure 1.1.

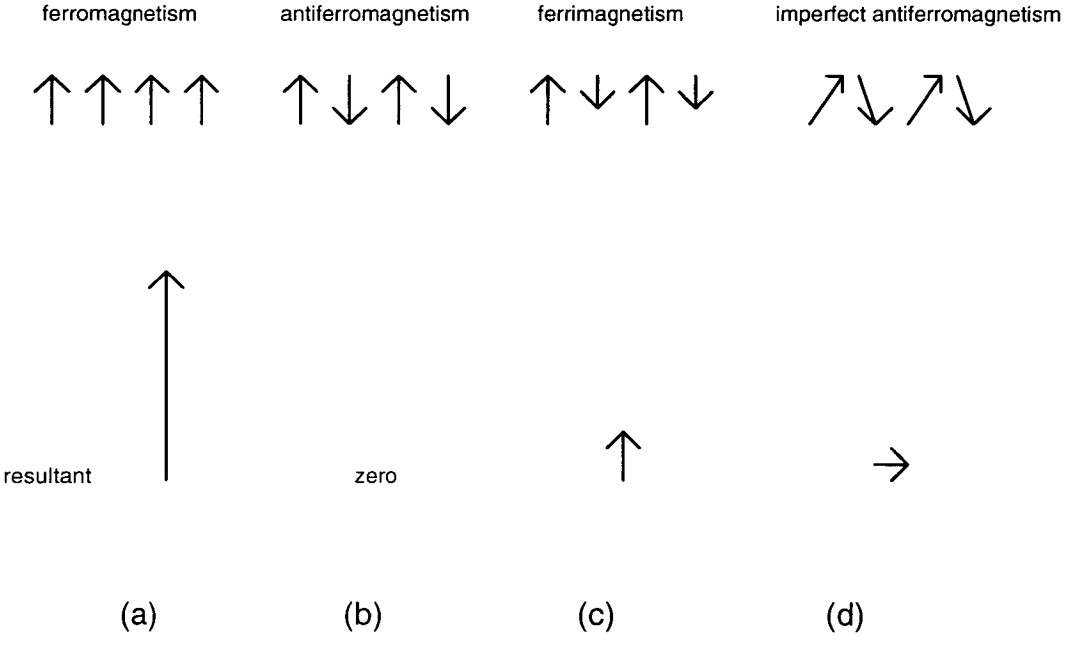


**Figure 1.1** Schematic diagram showing atomic moment arrangement in various type of magnetism.

Iron (Fe) is a good example of a ferromagnetic material. If the atomic moments are aligned in an anti-parallel direction, the result is antiferromagnetism [Figure 1.1 (b)]. Such materials have zero net magnetic moments and hence are non-magnetic. If the anti-parallel atomic arrangement is not perfect [Figure 1.1 (d)], a small net moment results, a behaviour known as imperfect antiferromagnetism (e.g. Thompson and Oldfield, 1986). Hematite is an example of a mineral displaying this

behaviour. In ferrimagnetism, the atomic arrangements are still antiparallel as in antiferromagnetism, but the antiparallel moments are not equal. Hence there is a net magnetic moment [Figure 1.1 (c)]. A good example of a mineral which exhibits this behaviour is magnetite.

Magnetite ($Fe^{2+}O^{2-}.Fe_2^{3+}O_3^{2-}$) has a close-packed face centred cubic crystal structure (Figure 1.2). Its structure is often referred to as inverse spinel. The crystal structure contains two sites which are often referred to as A and B sites. The A site is tetrahedrally co-ordinated while the B site is octahedrally co-ordinated. Cations occupying site A have a magnetic moment which is antiparallel to those in B site. The two B sites available per unit formula of magnetite are each occupied by a $Fe^{2+}$ ion and a $Fe^{3+}$ ion. The other $Fe^{3+}$ ion in the formula occupies the A site. In total there are 9 $\mu_B$ and 5 $\mu_B$ in the B and A sites respectively, hence the net magnetic moment is 4 $\mu_B$. Magnetite is said to be non-stoichiometric if the total available A and B sites in the sample are not occupied by $Fe^{2+}$ and $Fe^{3+}$ ions according to the ratio of the formula. Otherwise it is stoichiometric.

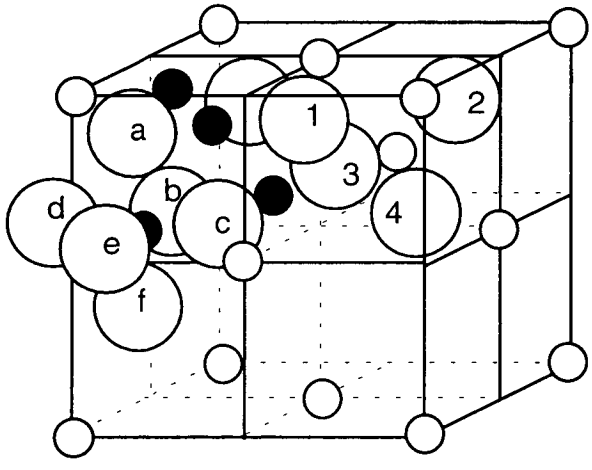


**Figure 1.2** A schematic diagram of a unit cell of magnetite crystal structure. The oxygen ions are shown as large circles while small circles are for $Fe^{3+}$ in tetrahedral sites (i.e. A site). The oxygen ions labelled 1, 2, 3, and 4 can be seen surrounding such an ion. Octahedral sites (i.e. B site) such as the one shown surrounded by oxygen ions labelled a, b, c, d, e, and f, contain either $Fe^{3+}$ or $Fe^{2+}$ ions. The ions are shown for only 2 sub-cubes of the total 8 sub-cubes forming a unit cell. ( redrawn After Lax and Button, 1962).

## 1.3 Magnetic domain Theory

Magnetic domains are a result of the competition between various energy contributions to the total magnetic energy of a sample. The energy contributions are : exchange, magnetocrystalline anisotropy, magnetostatic, magnetoelastic and external field energies.

### 1.3.1 Exchange energy ($E_{ex}$)

Heisenberg (1928) demonstrated that the exchange energy between two adjacent spin vectors $\mathbf{S}_i$ and $\mathbf{S}_j$ is given by

$$E_{ex} = -2J_E\mathbf{S}_i \cdot \mathbf{S}_j \qquad (1.3)$$

where $J_E$ is a quantity known as the exchange integral, $\mathbf{S}_i$ and $\mathbf{S}_j$ are the electron spin vectors.

### 1.3.2 Magnetocrystalline anisotropy energy ($E_k$)

This energy is due to the coupling between the spin and orbital magnetic moments of an electron. This coupling results in the alignment of atomic spins in certain crystal axes directions (the so-called 'easy' magnetisation directions). To rotate the spins away from the easy direction requires the application of energy. It is this energy which is the magnetocrystalline anisotropy energy. For a cubic material such as magnetite, the energy associated with a particular orientation of spontaneous magnetisation ($M_S$) is given by

$$E_k = K_1(\alpha_1^2\alpha_2^2 + \alpha_2^2\alpha_3^2 + \alpha_3^2\alpha_1^2) + K_2(\alpha_1^2\alpha_2^2\alpha_3^2) + \text{----} \qquad (1.4)$$

where $K_1$ and $K_2$ are the first and second magnetocrystalline anisotropy constants for the given material and $\alpha_1$, $\alpha_2$ & $\alpha_3$ are the direction cosines of the angles between $M_S$ and the crystal axes [100], [010] and [001],

respectively. Higher powers than $\alpha^2$ are usually neglected. Also neglected is the contribution of $K_2$.

### 1.3.3 Magnetoelastic energy ($E_\sigma$)

The spin-orbit coupling of atomic electrons discussed in the section above do strain the lattice of a magnetic material. This was first observed by Joule in 1842. Joule observed that the dimensions of an unmagnetised material changes when it becomes magnetised, a phenomenon called magnetostriction. Conversely the application of stress or accumulation of strain in a sample results in changing the spin-orbit coupling of atomic electrons and hence the direction of magnetisation. From Morrish (1965, pp. 325), for a cubic material such as magnetite, if the magnetostriction anisotropy is isotropic, the magnetoelastic anisotropy is given by

$$E_\sigma = \frac{-3}{2} \lambda_s \sigma \cos^2\theta \qquad (1.5)$$

where $\lambda_s$ is the magnetostriction constant and $\theta$ is the angle between the stress ($\sigma$) and the magnetisation.

### 1.3.4 External field energy ($E_{ext}$)

The external field energy is due to the interaction of the applied field vector (**H**) and the magnetisation vector **M** [defined as the ratio of the magnetic moment of a small volume at some point to that volume (e.g. Morrish, 1965, pp. 5)], is given by

$$E_{ext} = -\mu_o \int \mathbf{M} \bullet \mathbf{H} \, dv \qquad (1.6)$$

where the volume integral is over the whole particle.

### 1.3.5 Magnetostatic energy ($E_D$)

This energy is equivalent to the work required to assemble magnetic dipoles into a given configuration. The magnetostatic energy is given by

$$E_D = \frac{1}{2}\mu_o \int \mathbf{M} \bullet \mathbf{H}_D dv \qquad (1.7)$$

where $\mathbf{H}_D$ is the resultant field vector due to the contribution of all atomic moments in the volume of the particle.

## 1.4 Magnetic domain calculations

The total magnetic energy for a given cubic particle is given by

$$E_T = E_{ex} + E_k + E_\sigma + E_{ext} + E_D \qquad (1.8)$$

The type of domain structure which is stable at room temperature for a given sample is determined by minimising equation 1.8. $E_\sigma$ is usually ignored since it is about two orders of magnitude smaller than the next smallest energy $E_k$. Due to the non-linearity of equation 1.8, it is not possible to solve it analytically, hence numerical methods are required. Due to the huge computer time required to calculate the magnetostatic energy, it has not been possible in the past to minimise equation 1.8 without making a lot of simplifications. Most of the early work on domain prediction was obtained by the method of guessing a simple structure for a particle with a simple shape and then analytically solving equation 1.8 for the minimum total energy. This often means solving for the two most important energy competitors namely: $E_{ex}$ and $E_D$.

Figure 1.3 show examples of some hypothetical domain configurations. It can be envisioned that in Figure 1.3 (a), the exchange energy is lower than in (b) and (c) since in the latter there is a region where the atomic magnetic moments are not aligned. This region is shown by thick lines, and is known as the **domain wall**. See Figure 1.3 (d) for a schematic representation of the atomic magnetic moments within the domain wall. Domain configuration shown in Figure 1.3 (c) has virtually zero

magnetostatic energy, but this is achieved at the expense of an increase in the exchange energy. It is such visual intuition which was used to guide researchers into selecting the most probable stable domain structure before recent developments in high speed computer technology made unconstrained 3-D micromagnetic calculations possible.

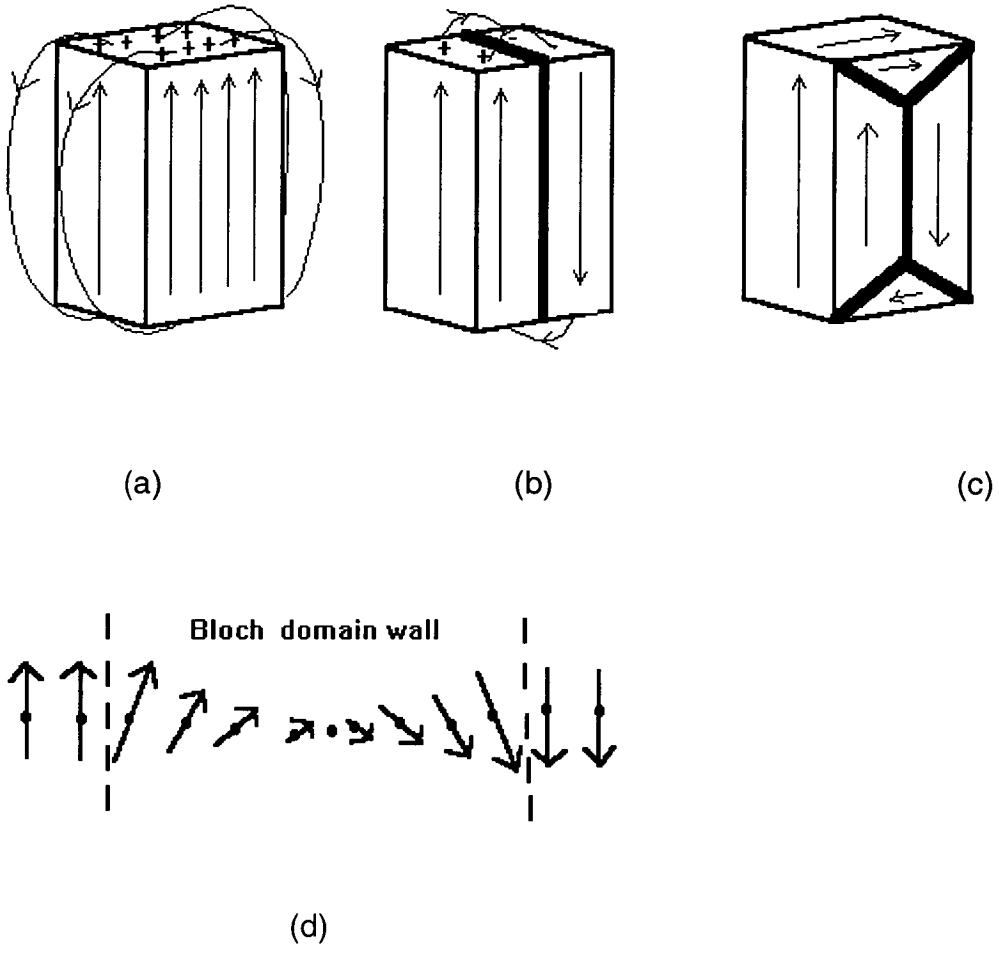


**Figure 1.3** Examples of hypothetical domain configurations, (a) large magnetostaic energy in SD, (b) decreased magnetostatic energy in two domains, (c) very low magnetostatic energy in two domains and two closure domains. A schematic diagram of a Bloch domain wall is shown in (d).

In the numerical approach (commonly referred to as the micromagnetic approach), the particle is divided into many regularly shaped regions and the magnetisation within each region is assumed to be constant.

An example of a picture for a domain structure obtained from 3-D micromagnetic calculation is shown in Figure 1.4.

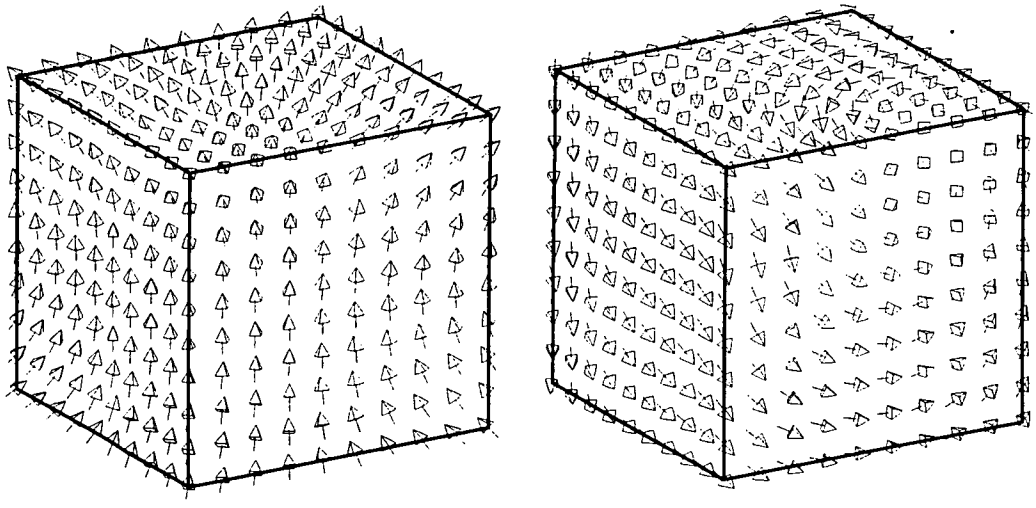

(a) (b)

**Figure 1.4** An example of a picture showing domain configuration obtained using an unconstrained 3-D micromagnetic calculation for a 0.1 μm cube. The structure shown in (a) is an initial zero-field magnetisation state after it was saturated in the [001] direction while (b) is when a field of 14 mT is applied in the [-001] direction. The domain configuration in (a) is often referred to as the 'flower' state while that in (b) is the 'vortex' state. (after Williams and Dunlop, 1995).

## 1.5 The thesis objectives

The domain structure of the magnetic minerals of rocks lies at the heart of magnetic stability criteria upon which paleomagnetism has been founded. By measuring the magnetic remanent magnetisation (NRM), Earth's processes such as geomagnetic field reversals, continental drift and pollution accumulation, may be revealed. In order to make accurate deductions of such processes from measured data, knowledge of the behaviour of the particles responsible for storing such magnetisation is required. The search for such knowledge is the preoccupation of rock magnetists. Rock magnetists use natural and artificially produced magnetic minerals to systematically measure the magnetic behaviour of such particles and compare with theoretical predictions.

The mineral which is the subject of this study is magnetite an important paleomagnetic carrier. Fine particles of magnetite of size less than 0.03 μm don't exhibit any remanence at room temperature because their total magnetic energy is less than the ambient thermal energy (Néel, 1955). This behaviour is known as superparamagnetism. The mechanism of magnetisation reversal for magnetite particles larger than superparamagnetic particles, but less than about 0.05 μm [i.e. single-domain (SD) particles], is well described by the coherent rotation of atomic moments (Stoner & Wohlfarth, 1948). The mechanism of reversal for larger (>15 μm) magnetite particles [i.e. Multidomain particles (MD)] is reasonably described by the movement of well defined domain walls. The mechanism of magnetisation reversal for particles whose size is in between that of SD and MD particles, remains poorly understood. Before the behaviour of pseudo-single-domain particles (PSD) was noticed to be different from that of MD, a sharp drop in the remanent-carrying ability was expected immediately above the critical SD size. No experimental observation supported this expected behaviour. Experimental results showed a gradual decrease in coercivity ($H_c$) over many decades of grain size (e.g. Dunlop, 1981; Heider et. el., 1987).

In an attempt to explain this observed discrepancy, several theories based on the mechanism of reversal of SD and/or MD have been proposed by various researchers. These include the possibility that atomic magnetic moments of domain walls behave as SD (e.g. Dunlop, 1977), that the net moment is due to an odd number of domains (e.g. Dunlop, 1983), and failure of domain wall nucleation (e.g. Halgedahl and Fuller, 1983).

According to recent unconstrained 3-D micromagnetic calculations (e.g. Williams and Dunlop, 1989, 1995; Thomson, et. al., 1994; Fabian et. al., 1996), conventional domains cannot form in submicron grains in the PSD size range; instead, there is a continuous spatial variation of magnetisation within each grain, the so-called vortex state. Due to their small size, observing domains of submicron PSD particles of magnetite is a very difficult task, and has not yet been done successfully. The experimental evidence of the mechanism of magnetisation reversal for these particles is hence by inference from magnetic measurements such as hysteresis parameters obtained using magnetite powders.

Until this study, magnetite samples used in experimental studies of rock magnetism were often synthetic powders obtained by crushing either natural magnetite material (e.g. Day et al., 1977 and Dankers & Suguira, 1981) or synthetic magnetite crystals (e.g. Dunlop, 1986 & Heider and Bryndzia, 1987). In such magnetite powders, there is often a significant distribution of particle size and shape in a given sample. In addition, despite attempts to disperse magnetic powder particles into non-magnetic matrix, there is no way of ensuring that there is no grain clumping, or inter-particle magnetostatic interaction. The contribution of these effects to the measured magnetic properties of PSD is not known.

The main objectives of this study were to produce samples of non-interacting and also interacting parallelepiped magnetite particles, and to measure their magnetic properties and compare with theory. This is to be achieved via electron-beam lithography (EBL) nanoengineering technology which is often used to design semiconductor devices.

## 1.6 Thesis outline

In chapter 2, the various methods which are capable of producing a thin film of magnetite are discussed and the most suitable method for the production of arrays of magnetite using the EBL method identified. Also presented are the results of preliminary test experiments done using the method of photolithography. The production of suitable magnetite powders used for comparison purposes is also presented. The method of preparation of parallelepiped and cubic arrays of magnetite particles is presented in chapter 3. Results of attempts made to observe magnetic domains using transimission electron microscope (TEM) are reported in chapter 4. In

chapter 5 the results of low temperature magnetic measurements are presented. Room temperature magnetic properties for equant and elongated magnetite particles are presented in chapters 6 and 7 respectively. Finally, chapter 8 contains conclusions and suggestions for further work.

# Chapter 2 Sample preparation methods for magnetite powders and thin films

## 2.1 Introduction

The methods which utilise **electron beam lithography (ELB)** to produce arrays of magnetite particles, described in chapter 3, require the deposition of a thin film of magnetite, or alternatively iron which can be converted to magnetite. In this chapter the different methods which are capable of producing a magnetite thin film are discussed. Experiments done in order to find the best method are reported. Also presented are the methods used to produce magnetite powders. Magnetite powders with a narrow size range were produced so that their magnetic properties can be compared to those of arrays of magnetite particles produced by the EBL method. The nature and quality characteristics of the magnetite samples obtained using mainly XRD and electron microscopy are presented.

## 2.2 A brief review of methods of production of a magnetite thin film

A thin film of magnetite can be formed on a substrate either directly by reactive iron (Fe) deposition or indirectly by first depositing Fe or hematite ($Fe_2O_3$) and later converting it to magnetite by thermal treatment in an appropriate environment. The methods of deposition which are capable of producing magnetite thin films directly are (i) reactive evaporation, (ii) reactive sputtering and (iii) chemical vapour deposition.

In the reactive evaporation process, Fe is evaporated in a vacuum with an oxygen pressure of about 1-5 x $10^{-4}$ mbar. Oxidation occurs during the condensation of the evaporated Fe on a heated substrate (temperature usually greater than 250$^{o}$ C). The degree of oxidation depends on the ratio of the number of oxygen molecules to those of Fe atoms impacting on the substrate. This method has been used to produce polycrystalline (e.g. Bando et al., 1978) and single crystal magnetite (e.g. Fujii et al., 1989, 1994 and Shiguematsu et. al., 1980).

In the reactive sputtering technique, ions created by the ionisation of a gas strikes the Fe target causing some of its atoms to be released. The process is that of momentum transfer. The environment is usually a 1:1 ratio mix of Ar:$O_2$ resulting in a total pressure of about 0.4 - 3 x $10^{-2}$ mbar. The

substrate is maintained at a temperature of 500° C. Successful production of polycrystalline magnetite (e.g. Kim and Olivera, 1994, Ishii et al., 1980) and highly oriented or single crystal magnetite thin films (e.g. Margulies et. al., 1994) has been reported.

The process of chemical vapour deposition of magnetite thin films involves either reducing or decomposing a volatile compound of a suitable Fe halide onto a heated substrate (usually at a temperature of around 500-1100° C), hence forming a magnetite film there (e.g. Pulliam, 1967). As pointed out by Bando et. al., 1978, the complexity involved in controlling the many environmental parameters have limited the use of this method.

None of the methods of deposition of magnetite discussed above is reported to have resulted in films whose characteristics were consistent with that of pure magnetite when the substrate temperature was lower than about 200° C. It is not clear why this is the case. The temperature above 200° C is far higher than the temperature at which presently available high resolution electron radiation-sensitive organic resists used in EBL start to flow (the so-called glass transition temperature). For example the glass transition temperature for **poly methyl methacrylate (PMMA)** is 120° C. If the **lift-off** process (see chapter 3) is to be used, any patterns made on the resist will be lost upon heating the substrate above 200° C. In an attempt to avoid this problem, and also the problem of lack of saturation by magnetite thin films deposited directly on a substrate at a high temperature (e.g. Margulies et al., 1994, 1996), reactive evaporation of magnetite experiments were carried out with the substrate at various temperatures including room temperature. The main aim was to see if good quality magnetite can be obtained at a substrate temperature lower than that of the glass transition temperature of PMMA. In the following section the results of this experiment are presented.

## 2.3 An attempt to deposit a magnetite thin film directly onto a substrate at temperatures lower than 120° C

The experiment was done using an electron-beam heated evaporation system at the Department of Physics (Heriot Watt University). The equipment is schematically shown in Figure 2.1. The substrate holder was adjusted directly above the crucible to the desired height. The substrates used were glass, aluminium and silicon. Small pieces of Fe cut

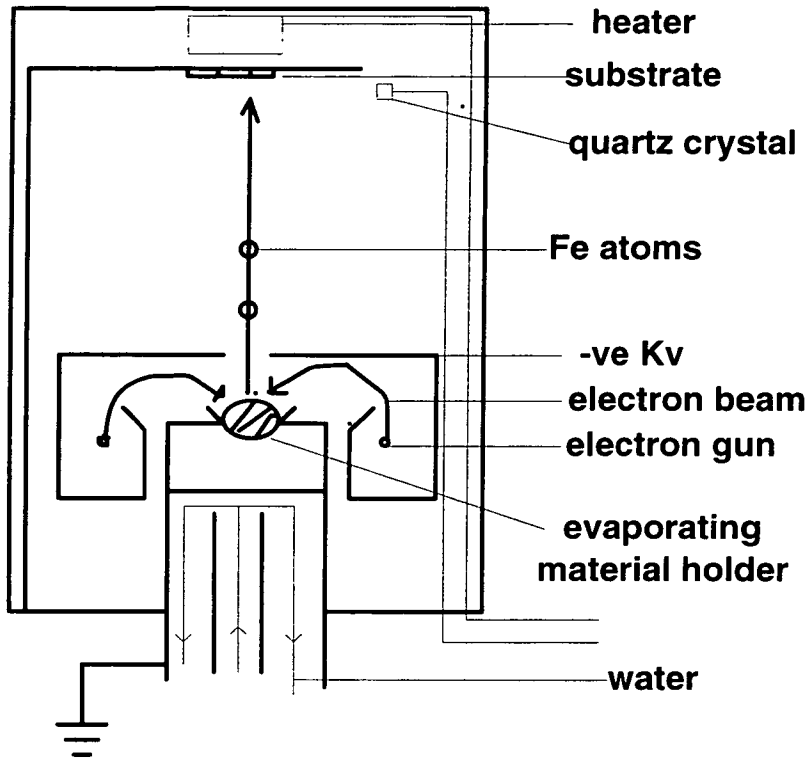


**Figure 2.1** Schematic diagram showing the vacuum evaporation equipment used in part of this study.

from a 99.99% purity foil (Johnson Matthey) were placed into the crucible. By changing the voltage and current applied to the filament, the rate of deposition was varied. The deposition rate and film thickness were measured by a quartz crystal oscillator. The oxygen environment within the chamber was controlled by a massflow meter. The substrate was heated by a 500 watt tungsten lamp. A temperature controller was used to maintain the temperature to within +/- $10^{o}$ C of the desired value. The logical sequence of the experimental run was to start with the substrate at a temperature higher than $200^{o}$ C where good quality magnetite is known to form, and then to gradually decrease the temperature.

### 2.3.1 Results

$Fe_3O_4$ was obtained by evaporating Fe onto a substrate at a temperature higher than $140^{o}$ C under an oxygen pressure of 0.8 - 4 x $10^{-4}$ mbar. The deposition rate varied from 0.1 to 5 nanometer per second (nm/s). Increasing the rate of deposition to more than 5 nm/s when the substrate temperature was lower than about $140^{o}$ C resulted in films which didn't adhere well to the substrate. They all failed the sticky tape test. This test is done by placing a sticky tape on top of a film and then pulling it up. If the film comes out with the tape then it has failed the test, otherwise it is considered to have passed. No $Fe_3O_4$ single phase was obtained if the substrate temperature was lower than about $140^{o}$ C. Due to the above mentioned difficulties, the experiment didn't achieve the desired aim of producing good quality $Fe_3O_4$ at lower than the glass transition temperature of PMMA resist which is around $120^{o}$ C.

An unusual result of general interest to the preparation of magnetite thin films obtained in this experiment is the production of octahedral grains (Figure 2.2). This is the first reported case of octahedral grains in a magnetite thin film. Octahedral magnetite grains are usually found in natural rocks and in artificial powders produced by hydrothermal methods. Interesting as this observation may seem, it was not of immediate interest to the present study since the grain orientation and inter-grain spacing is not controllable. That is, the particles are in a form similar to those of artificially produced magnetite powders which are often used in rock magnetic studies. In such powders, the effect of magnetostatic is not known.


**Figure 2.2** SEM picture of a magnetite thin film (0.5 µm thick). The film was produced in an oxygen environment of 2 x $10^{-4}$ mbar at a substrate temperature of 300 $^{o}$C. The picture shows octahedral magnetite grains similar to those often found in igneous rocks.

## 2.4 Methods capable of producing magnetite thin films indirectly

All the methods discussed above under section 2.2 can be used to produce either an Fe or $Fe_2O_3$ film at room temperature. Besides the above mentioned methods, an Fe thin film can also be formed by **electrochemical deposition (electroplating)**.

### 2.4.1 Electrochemical deposition

The application of the electrochemical deposition method involves the deposition of Fe onto $Al_2O_3$ pores. $Al_2O_3$ pores are formed when aluminium is made the anode in an electrochemical cell with a suitable acid electrolyte. In this application a potential is applied between two electrodes one of which is porous $Al_2O_3$ in a solution with Fe ions. The ions then migrate onto the $Al_2O_3$ pores and get neutralised and remain there. Thus by controlling the deposition condition, Fe can be deposited to the required thickness (AlMawlani et al., 1991, Dunlop et al., 1993).

Since the material of main interest to this study is not Fe or $Fe_2O_3$ but $Fe_3O_4$, a brief description of ways of converting either Fe or $Fe_2O_3$ to $Fe_3O_4$ is given in Table 2.1.

## 2.5 Choosing the method for use in this study

As in most other experimental work, the choice of the method to use depends on many factors. These include availability of equipment, reproducibility of results, simplicity and speed of the experiment. Based on the above requirements, the method of annealing in argon described in Table 2.1 above seems to be the most suitable. An attempt was made to use this method several times without success. It is not clear why the method did not work.

In this study two annealing processes which convert Fe directly into $Fe_3O_4$ were used. These processes will be referred to as either **method 1 or method 2**.

| Method | Brief description | Reference example |
|---|---|---|
| **Annealing in vacuum** | An Fe thin film is annealed at 450-550 $^{o}C$ in air or $O_2$ to convert it to $Fe_2O_3$. The $Fe_2O_3$ layer is then covered with a second layer of Fe (about 12% of the original Fe) and annealed at 350-400 $^{o}C$ in a vacuum of better than $10^{-7}$ mbar. The result after more than 8 hours is a thin film of magnetite. | Feng et al. 1972 |
| **Annealing in Argon** | An Fe film is oxidised in oxygen gas at 400 $^{o}C$ for 1 hr in atmospheric pressure to convert it to $Fe_2O_3$. The $Fe_2O_3$ film is then reduced to $Fe_3O_4$ films at 340 $^{o}C$ in argon gas saturated with methanol vapour at room temperature. A $Fe_2O_3$ film (0.24 μm thick) is reported (Sato et al., 1990) to have been completely converted to $Fe_3O_4$ in 1 hour by annealing in this environment. | Sato et al., 1990 |
| **Annealing in wet Hydrogen** | $Fe_2O_3$ produced either directly or indirectly by thermal treatment of Fe as described in processes (a) or (b) above is reduced to $Fe_3O_4$ by annealing at 500 $^{o}C$ in an atmosphere of 2.3:1 ratio mix of $H_2$:$H_2O$. | Borrelli et al., 1972 |

**Table 2.1** Processes which are capable of converting Fe or $Fe_2O_3$ to $Fe_3O_4$.

### 2.5.1 Method 1

While running experiments described under section 2.3 above, an attempt was made to check if an Fe thin film could not be converted to $Fe_3O_4$ by annealing in a similar environment to that used to produce $Fe_3O_4$ by reactive evaporation. The samples were annealed in a chamber which was first filled with $N_2$ before being evacuated to a pressure of about $10^{-7}$ mbar. Oxygen was then introduced so that a total pressure of about $2 \times 10^{-4}$ mbar was obtained. A massflow meter was used to maintain this pressure while a temperature controller was used to keep the temperature at 300 +/- 10° C during the duration of the experiment. An X-ray diffraction (XRD) pattern of an Fe thin film annealed for 3.5 hours in this environment matched those for Fe and $Fe_3O_4$ only. It was therefore clear that part of the Fe has changed to $Fe_3O_4$. Further annealing in the same environment led to an increase in the intensity of the lines for $Fe_3O_4$ and a decrease in those for Fe. After 11.5 hours of annealing, no trace of Fe could be detected by XRD (Figure 2.3). In general, the grain size of the deposited Fe thin films were in the size range 10 - 40 nanometer (nm). Figure 2.4 shows a SEM picture of typical grains of the deposited Fe films.

Method 1 was later abandoned in favour of method 2 mainly because it produced $Fe_3O_4$ particles with high coercivities similar to those due to stressed grains (see chapter 6). Due to the rapid cooling of the sample at the end of the annealing process which was necessary in this method to avoid oxidation to $Fe_2O_3$, the particles may be under stress.

Abel et al., 1983, used a similar method except that in their method the background pressure was not $N_2$ but air. The oxygen pressure in their experiment was about $6.5 \times 10^{-3}$ mbars and temperature was 350° C. They reported that the resulting $Fe_3O_4$ thin film was under stress and proposed that annealing at higher temperature may reduce the stress.

### 2.5.2 Method 2

The second method (hereafter referred to as method 2), places the Fe samples in a vertical furnace at atmospheric pressure (Figure 2.5). A $CO_2$:$H_2$ ratio mix of 100:6 was passed over the sample to maintain an oxygen fugacity within the stability field of $Fe_3O_4$ at 600° C throughout the

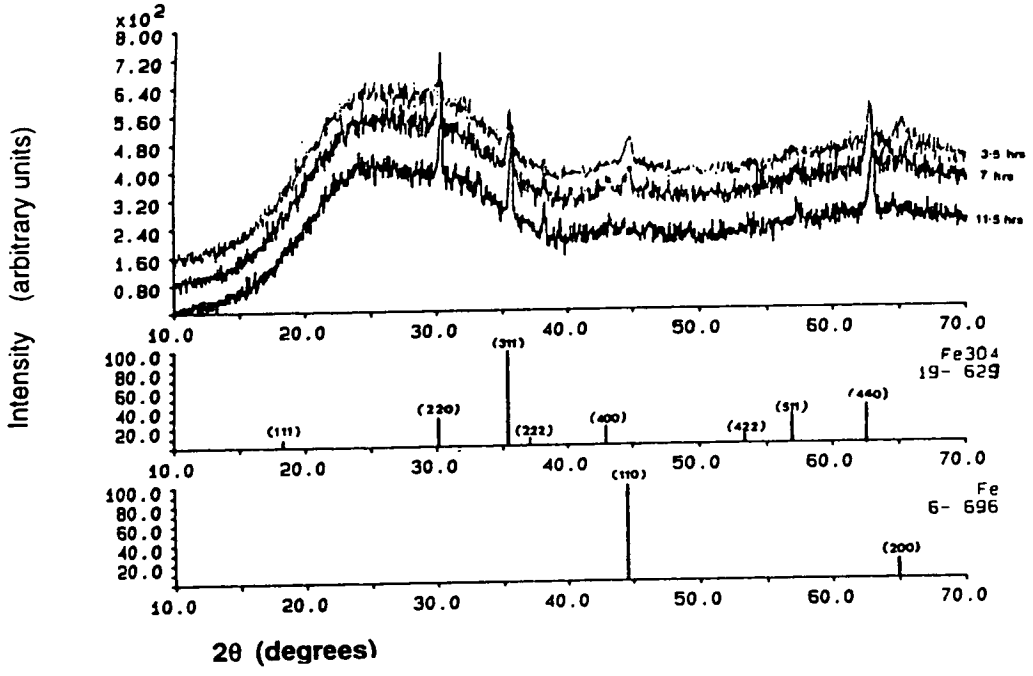


**Figure 2.3** XRD intensity patterns showing the conversion of Fe to $Fe_3O_4$ during annealing using method 1.

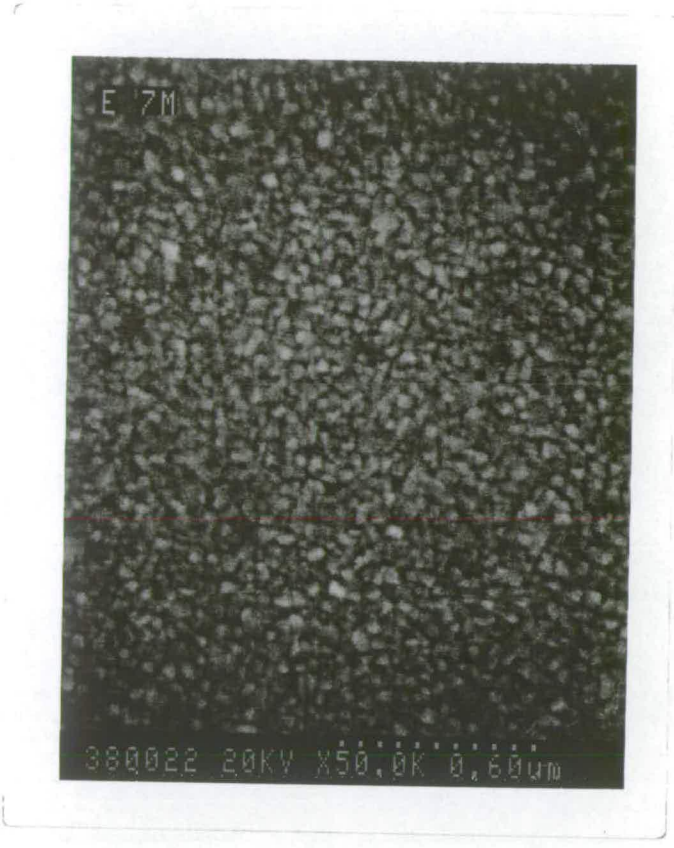


**Figure 2.4** SEM picture of typical grains of the Fe deposited at room temperature. The Fe film has a thickness of 0.5 µm and the grains are about 20 - 40 $\mu$m in size.

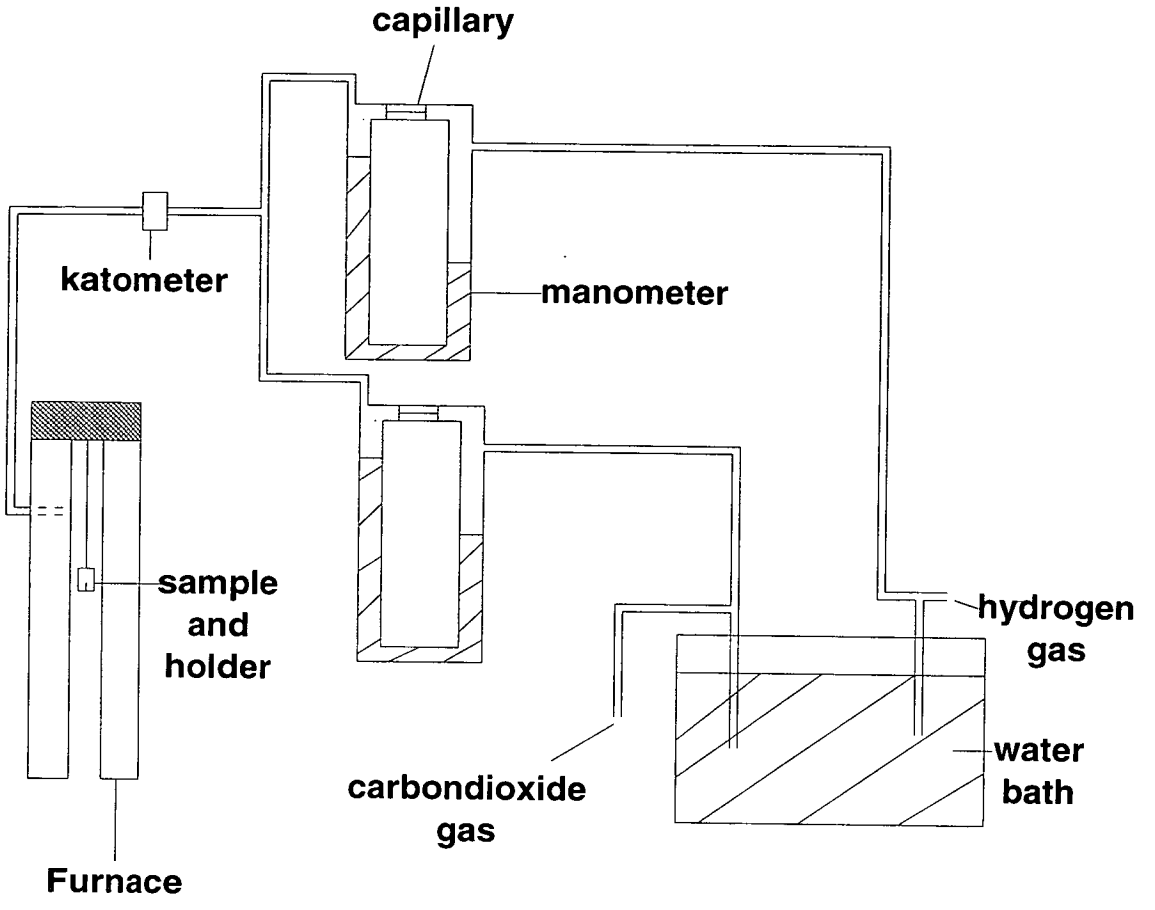


**Figure 2.5** Schematic diagram showing the vertical furnace used to convert samples of iron to magnetite by annealing **Method 2**.

duration of the annealing process. This ratio was found with the help of phase equilibrium diagrams of Muan and Osborn (1965). The temperature was controlled to an accuracy of +/- 1° C. Before selecting the annealing temperature of 600° C for use in this method, several temperatures were tried. These varied between 1100° C down to 300° C. XRD patterns for all $Fe_3O_4$ films obtained by annealing Fe films at a temperature above 800° C were found to contain a trace of $Fe_2SiO_4$ (fayalite). The Fe films annealed at lower than 800° C did not show any trace of fayalite (Figure 2.6). Fayalite is a result of the oxidation of Fe and silicon at the film-substrate boundary. To avoid fayalite in the $Fe_3O_4$ particles, an annealing temperature below 800° C had to be selected.

At 600° C after 4 hrs a 1 μm thick Fe film was fully converted to $Fe_3O_4$, while at 300° C it took around 16 hrs, I chose former temperature for further work. It was observed that a thin film of Fe could be converted to $Fe_3O_4$ by subjecting it to any temperature between 400° C to 800° C without varying the $CO_2$:$H_2$ gas ratio mix of 100:6. This observation together with the rapid drop in the rate of conversion of Fe to $Fe_3O_4$ with decreasing temperature, made possible slow cooling of the sample without oxidising to $Fe_2O_3$. Sample cooling was done by gradually pulling the sample holder from the furnace centre at a rate of about 0.5 cm/minute.

When a polycrystalline Fe thin film composed of grains such as those shown in Figure 2.4 was annealed using annealing method 1, the resulting $Fe_3O_4$ thin film was still polycrystalline. However, when method 2 was used, the grains joined together as they grew in size. Figures 2.7 and 2.8 show SEM pictures of the grains for a thin film (0.5 μm thickness), retrieved from the annealing furnace after 1 hour and 4 hours respectively. It can be seen from Figure 2.7 that the grains have increased in size and joined together compared to those of Fe (Figure 2.4). A magnetite thin film obtained after the conversion of Fe to magnetite was complete (i.e. after 4 hours), was composed of large platelet grains, several microns in diameter (see figure 2.8). From the XRD data (Figure 2.6), it can be concluded that the crystal orientation of these grains is random.

It should be noted here that since the size of each platelet grain is several micrometers, none of the magnetite particles of main interest to this study, namely: 0.1 - 1 μm, should be polycrystalline. In chapter 6, it will be shown that the magnetite thin films produced using the annealing technique described in this section, readily saturate in fields of less than 500 mT. This

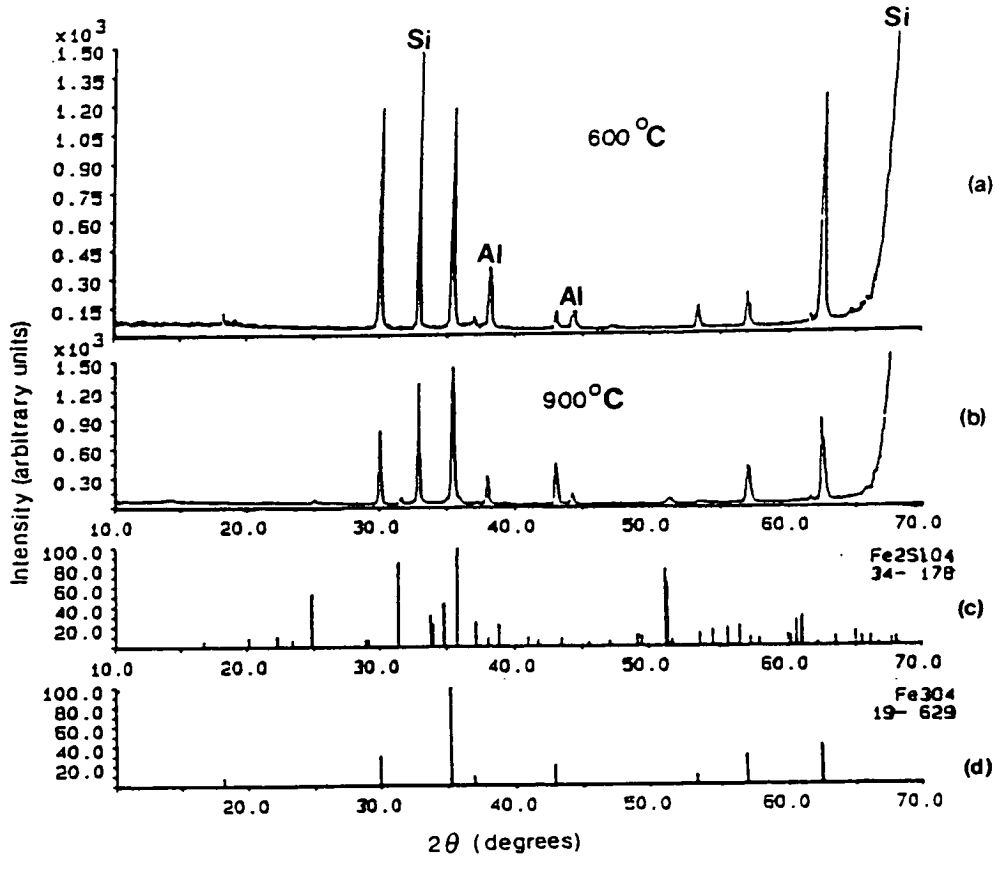


**Figure 2.6** XRD pattern for an Fe thin film of 0.5 μm annealed at (a) 600 °C and (b) 900 °C compared to (c) XRD patterns for Fayalite ($Fe_2SiO_4$) and (d) magnetite ($Fe_3O_4$). The lines labelled Si and Al are for the silicon substrate and the aluminium of the sample holder respectively.

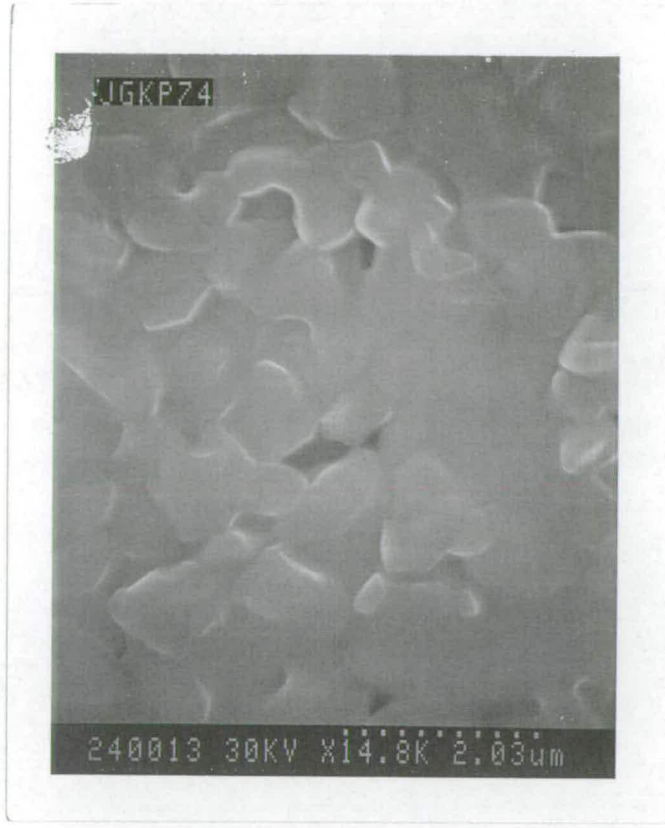


**Figure 2.7** SEM picture of a thin film of Fe (thickness 0.5 μm) after annealing for 1 hour in carbon-dioxide hydrogen gas mix at 600 $^{o}$C (Method 2, section 2.5.2). It is evident from this picture that the Fe grains which were like those shown in Figure 2.4, have grown in size and joined together.

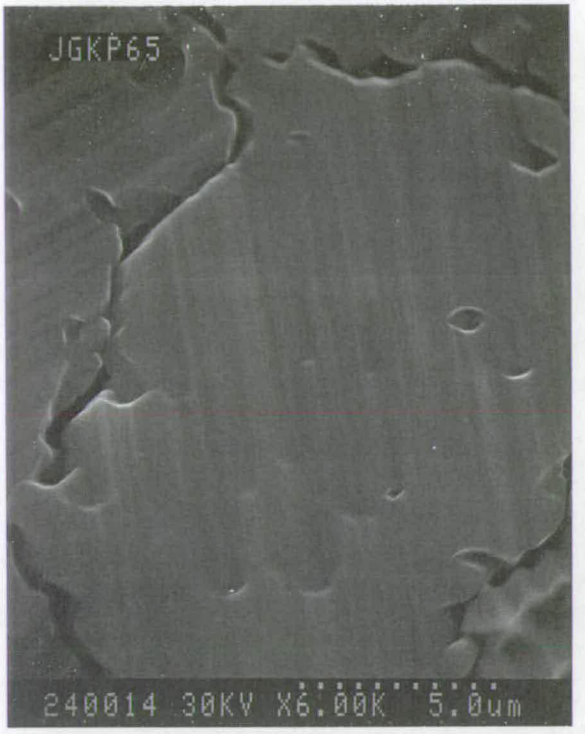


**Figure 2.8** SEM picture of a thin film of Fe (thickness 0.5 μm) after annealing for 4 hours (total conversion of Fe to $Fe_3O_4$ complete) in carbon-dioxide hydrogen gas mix at 600 $^{o}$C (Method 2, section 2.5.2). The platelet magnetite grains are several microns in diameter.

behaviour is in contrast to that of magnetite thin films produced by Margulies et al., 1996, which do not saturates even in fields as high as 7 000 mT.

## 2.6 Magnetite powders used it this study - a brief description

Magnetite powders with a narrow size range were prepared using the **hydrothermal recrystallisation method** similar to that described by Heider and Bryndzia, 1987. Also used was the **gel ageing method,** similar to that described by Sugimoto and Matijevic, 1980. In addition samples of maghemite ($\gamma Fe_2O_3$) of differing aspect ratios were annealed in an carbon-dioxide and hydrogen gas mix ratio of 100:16 at 350$^o$ C.

### 2.6.1 Hydrothermal recrystallisation method

Commercially obtained magnetite (Johnson and Matthey) was placed in a platinum or gold capsule together with a mineraliser ($NH_4Cl$ or distilled water) and sealed. The capsule was then placed into a vertically mounted vessel (usually referred to as a bomb). The bomb was made of NiMONiC, which acts as a suitable buffer for the correct oxygen fugacity for the production of magnetite. The bomb was subjected to a compressed argon pressure of 2 Kbar at a suitable temperature and left under these conditions for 7 days. At the end of the experiment, the bomb is quenched and the magnetite washed with distilled water.

Figure 2.9 (a) and (b) shows SEM pictures of typical hydrothermally produced magnetite particles obtained at a bomb temperature of 550$^o$ C using distilled $NH_4Cl$ and water as a mineralizer respectively. XRD patterns for these samples matched those for magnetite alone with no trace of other iron oxides such as hematite and maghemite.

### 2.6.2 Gel ageing method

Spherical shaped grains of 0.2 μm average size were produced by adding a solution of $KNO_3$ and KOH to $FeSO_4.7H_2$ at 95$^o$ C. During this process nitrogen gas was bubbled through the solution to avoid the formation of hematite. After 4 hours the black precipitated gel was washed several times with distilled water. XRD patterns matched those for magnetite alone.

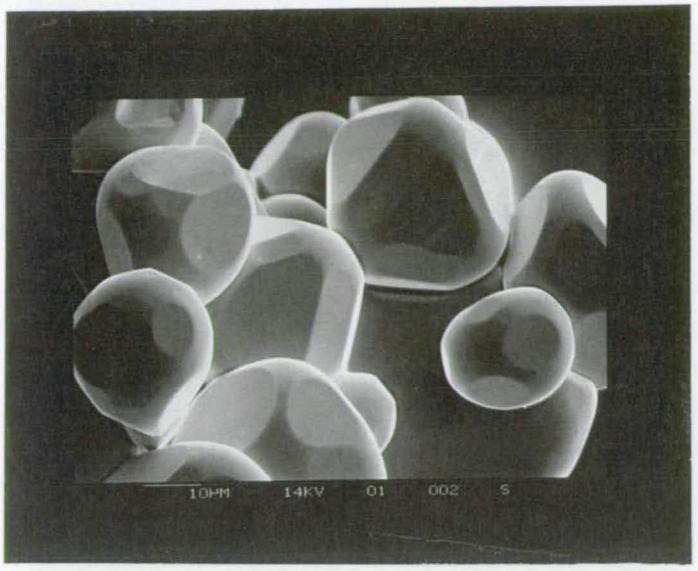


(a)


(b)

**Figure 2.9** SEM pictures of typical magnetite which was produced by the method of hydrothermal recrystallisation (a) using $NH_4Cl$ as a mineraliser and (b) using distilled water.

Acicular maghemite single crystal particles with a narrow size distribution (< 10% standard deviation) were kindly provided by Dr Morales of University of Wales (Bangor). In the following section the process of converting these acicular maghemite samples to magnetite is described.

### 2.6.3 Conversion of maghemite to magnetite by annealing

Maghemite samples G3 and G6 are comprised of prolate spheroidal particles with aspect ratios of 3 and 6 respectively. The average particle diameter of G3 is 0.12 μm while that of G6 is 0.084 μm. The samples were prepared from uniform hematite particles obtained by homogeneous hydrolysis in solution. Fig 2.10 shows an electron microscope picture of G3 particles. For more details on the method of preparation and characterisation of these maghemite samples the interested reader is referred to a paper by Morales et. al., 1994.

These maghemite samples were converted to magnetite by annealing at a temperature of 350$^{o}$ C in an environment of carbon-dioxide to hydrogen gas mix ratio of 100:16. Except for the temperature and gas mix ratio, the annealing method and apparatus used are the same as that of method 2 described above. Total conversion from maghemite to magnetite was complete after 24 hrs. This was confirmed by an XRD pattern which matched those for magnetite alone. No significant increase in the particle size of sample G3 was observed when it was converted to magnetite. Figure 2.11 shows a SEM picture of typical particles of magnetite obtained by converting the maghemite sample G3. Samples G3 and G6 were renamed JG3 and JG6 after conversion to magnetite.

## 2.7 Summary

Different possible ways of producing a thin film of magnetite have been presented. It has been shown that methods which are capable of producing a thin film of magnetite directly are not suitable for the production of arrays of magnetite particles. This is mainly due to the higher than resist flow temperature to which a substrate must be subjected to in order for stoichiometric magnetite be produced, as well avoiding stresses and other high substrate temperature reactive deposition parameters which cause magnetite thin films to not saturate even in fields as high as 7 000 mT

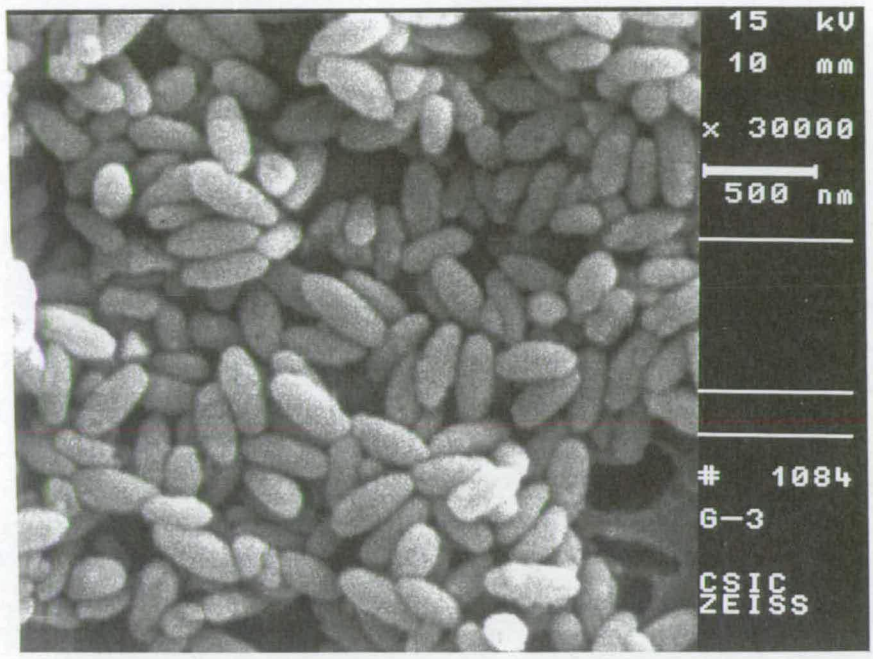


**Figure 2.10** Electron microscope picture of particles of the maghemite sample G3.

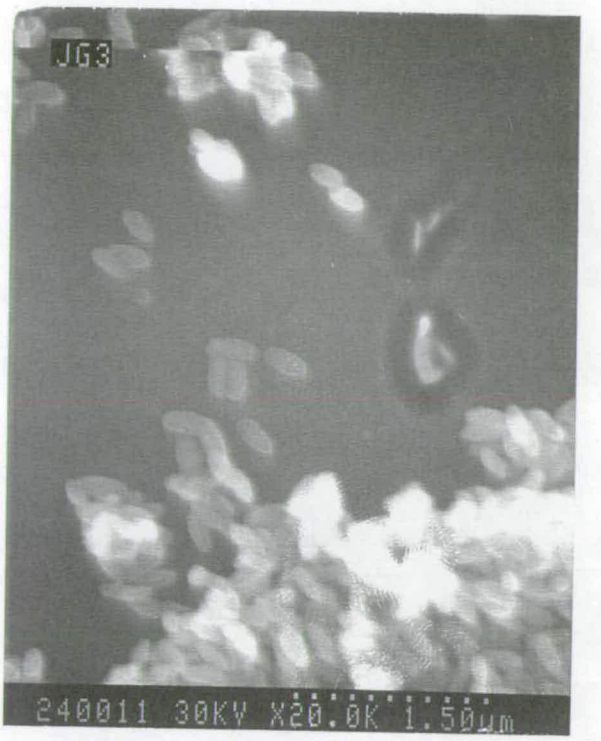


**Figure 2.11** SEM picture of magnetite obtained by annealing maghemite sample G3 in a carbon-dioxide and hydrogen gas mix of ratio 100:16 at 350 $^{o}$C. The particles do not show any significant increase in size when compared to those of Figure 2.10.

(e.g. Murgulies, 1994, 1996). The method which avoids these problems was found to be that which deposits Fe at room temperature with a later annealing stage in a carbon-dioxide and hydrogen mix environment. Various methods of preparing magnetite powders were used to produce equant or elongated magnetite powder particles.

# Chapter 3 The production of magnetite arrays using electron beam lithography

## 3.1 Introduction

In this chapter the methods of photolithography and electron beam lithography are introduced. Preliminary tests were done using the method of photolithography because its cheaper. The reasons for selecting a particular lithography process where there is a choice are discussed. Problems encountered in the fabrication of arrays of magnetite are also discussed. The nature and quality characteristics of the fabricated magnetite samples done using mainly XRD and electron microscopy are presented. The method of production of magnetite particle via the electron beam lithography and some of the magnetic properties of the samples described in chapters 5 and 6 of this thesis, have been accepted for publication in Geophysical Research Letters (King et. al., in press)

## 3.2 A brief description of the electron beam lithography process

The term 'lithography' is a Greek word which means 'writing on stone' (Hatzakis, 1988), however in the present context it refers to the whole process described below including the tools used. There are mainly two possible processes, namely: lift-off and etching.

### 3.2.1 The lift-off process

This is illustrated in Figure 3.1. In this process, an electron radiation sensitive layer (often polymeric) is spun on a substrate which is usually made of material with high electrical conductivity to avoid charging during electron beam exposure [Fig 3.1 (a)]. The sample is then baked for several hours above the glass transition temperature (about $120^{o}$ C) to promote adhesion to the substrate. The electron radiation sensitive layer often referred to as a 'resist', can be divided into two groups namely: (i) positive and (ii) negative resists. Upon placing the sample into a chemical known as the developer and exposure to an electron beam of the appropriate energy, the exposed area is removed by the developer for a positive resist while for a negative resist the unexposed area is removed [Figure 3.1 (b)]. After depositing a thin

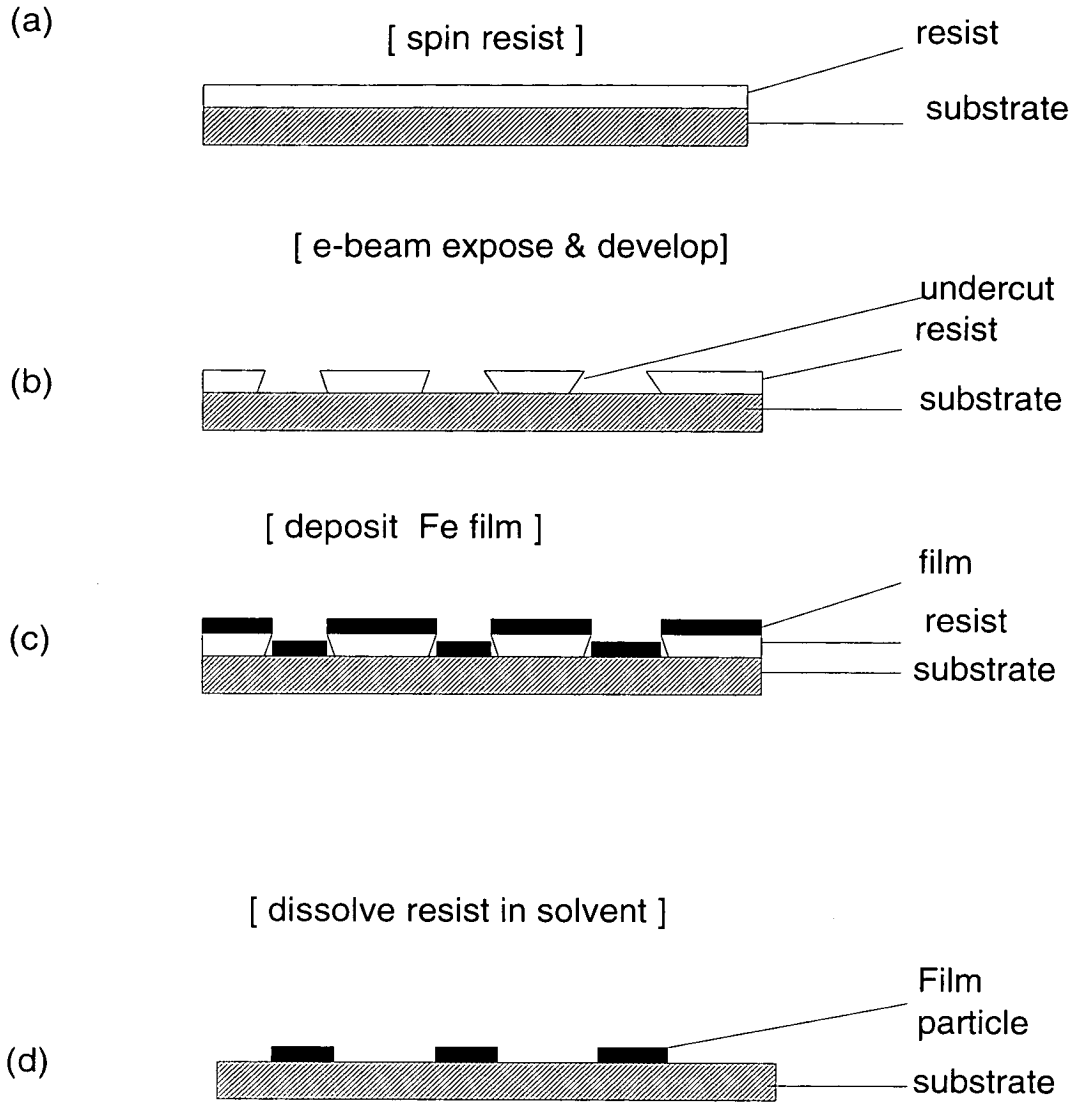


**Figure 3.1** Schematic representation of the electron beam lithography **lift-off** process showing the end result after (a) spinning of the resist, (b) e-beam exposure and development, (c) Fe deposition and (d) resist dissolving.

film of the material of interest [Figure 3.1 (c)], the resist is dissolved in an organic solvent. For example, acetone or chlorobenzene is used to dissolve the high resolution resist PMMA. The end result is a template like the one shown in Figure 3.1 (d).

### 3.2.2 The etching process

This is illustrated in Figure 3.2. A thin film of the material of interest is deposited on the substrate before spinning the resist and baking it [Figure 3.2 (a)]. Upon exposure and development, the pattern shown in Figure 3.2 (b) results. A dry or wet etch can then be applied. This is a process where the areas of the thin film not protected by resist get removed by either placing in a solution which etch the film but not the resist (the so-called wet etch) or by bombarding the sample with a beam of ions/atoms or a gas which selectively etch the film while leaving the resist alone. Figure 3.2 (c) shows a typical end result of such a process. After removing the resist by dissolving in an appropriate solvent, a template such as that shown in Figure 3.2 (d) remain.

## 3.3 Reasons for the choice of lift-off over etching process

The particles in the SD and PSD size range which are of interest in the present study, requires the use of a high resolution resist. PMMA which offers the highest resolution available among conventional resists is not suitable for the etching process.

## 3.4 Photolithography production of magnetite lines

### 3.4.1 A brief description of the process of photolithography

In this process, desired patterns are made on a plate (often using electron beam lithography). The pattern is composed of light transparent and opaque areas. This plate (called a mask) can be used to make a pattern on a photo sensitive resist by exposure to a high energy light beam (e.g. ultraviolet light). Upon exposure to this light the opaque areas protect the resist from light exposure while the transparent areas do not. After developing the resist with a correct developer, the result is the imprint of the

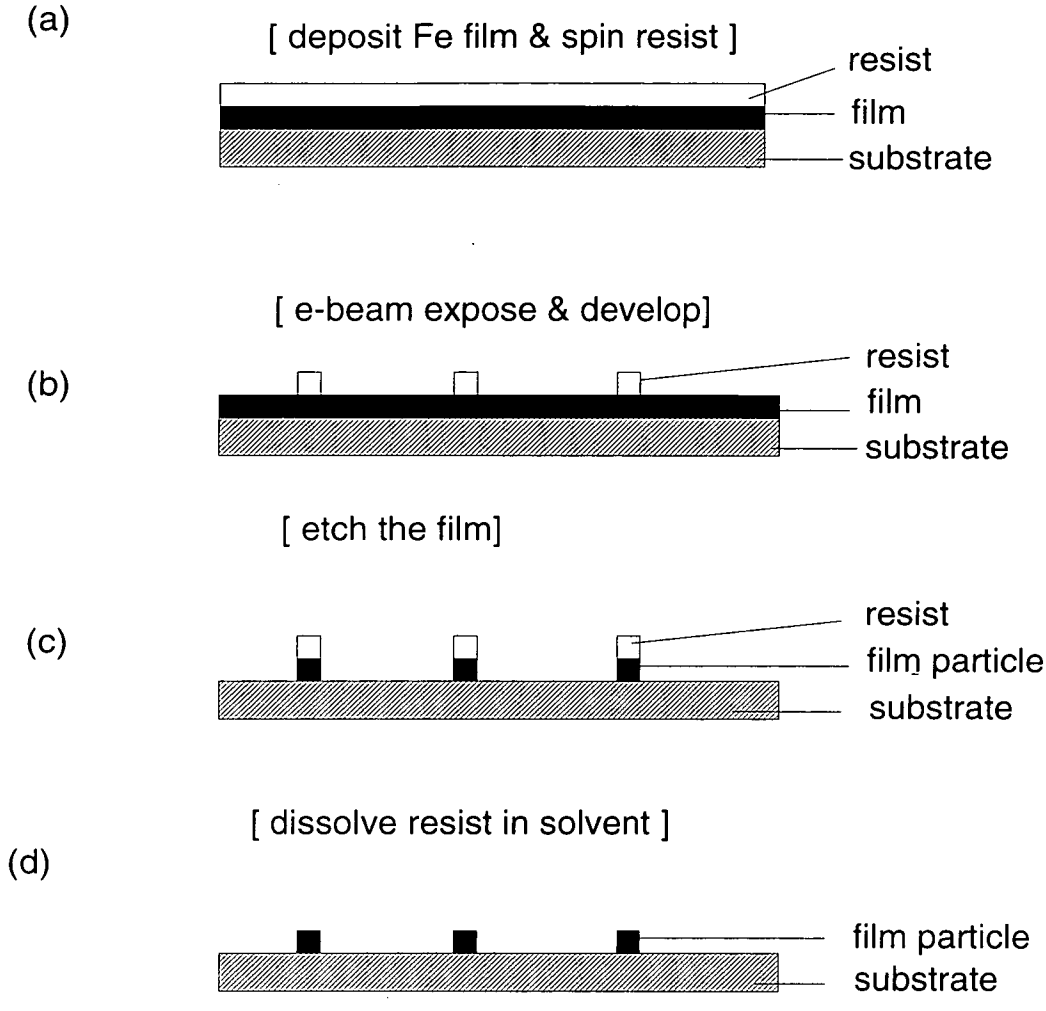


**Figure 3.2** Schematic representation of the electron beam lithography **etching** process showing the end result after (a) film deposition and resist spinning, (b) e-beam exposure and development of resist, (c) etching of film and (d) dissolving resist.

desired pattern on the substrate. Apart from the use of a light beam (photons), the process of photolithography is very similar to that of electron beam lithography described under section 3.2 (Figures 3.1 and 3.2).

The size of features which can be patterned using photolithography is limited by the wavelength of the light. The practical limit is around 0.5 μm. Once a mask is made it can be used many times to imprint the pattern on the substrate, hence it is cheaper than electron beam lithography where the expensive electron beam writer needs to be used each time a pattern is made. Another advantage of the photolithography process over that of electron beam lithography is that the substrate does not have to be a good conductor. In electron beam lithography if a substrate of poor electrical conductivity has to be used, one has to perform the cumbersome process of coating the resist with a layer of a good conductor before exposing it to the electron beam and having to get rid of it again before developing the sample.

### 3.4.2 Experiments and Results

A masking plate composed of lines of 2 μm width was used to make patterns on glass and silicon substrates. The opaque part of the mask was made of chromium. A positive photo resist sensitive to a light of 0.364 μm wavelength was used. After development, the sample was placed in chlorobenzene to shrink the resist and hence making possible an undercut (Figure 3.3). Fe was later evaporated at room temperature using the electron gun evaporator described under section 2.3 of this thesis. The lift-off process resulted in Fe lines which were later converted to $Fe_3O_4$ by annealing using method 1. Figure 3.4 shows optical microscope pictures of $Fe_3O_4$ lines obtained by this process. It can be seen from this figure that the lift-off process was successful and hence the experiment was a success. The next step was to attempt to fabricate submicron sized magnetite particles using EBL.

## 3.5 EBL fabrication of magnetite arrays - exposure test experiments

In order for the developer to remove the unwanted resist correctly, the resist has to be exposed to the correct number of electrons. The number of electrons required i.e. the dose (usually measured in $C/cm^2$), depends on

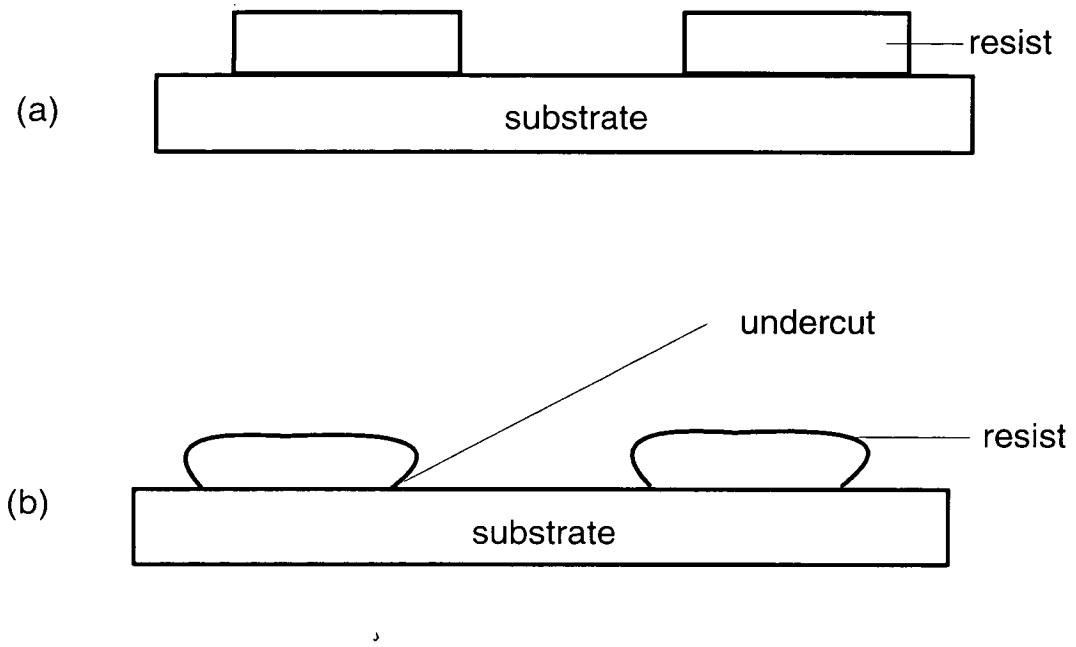


**Figure 3.3** Schematic representation showing (a) before resist shrinking and (b) after resist shrinking by placing in chlorobenzene to obtain an undercut.

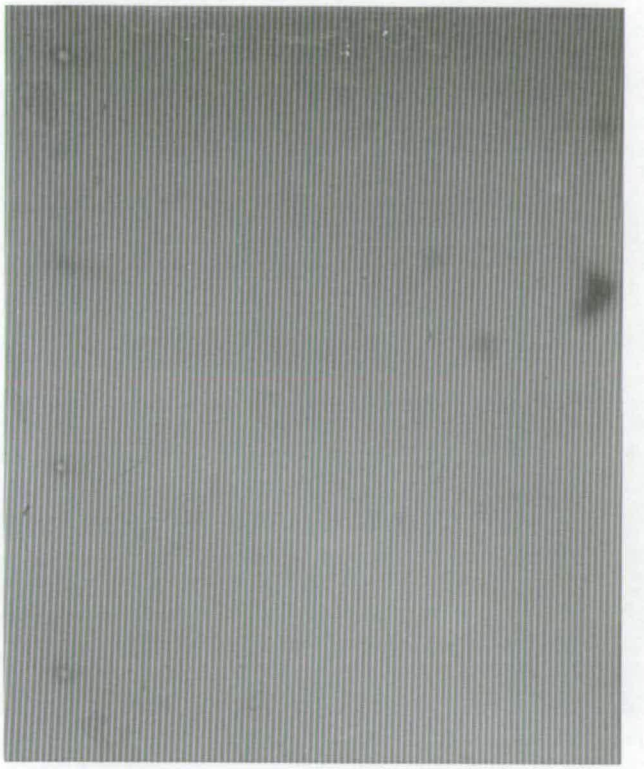

**Figure 3.4** A typical optical microscope picture showing lines of magnetite obtained in preliminary lift-off testing experiments. The magnetite lines in the picture are the white lines. Each magnetite line has a width of 2 μm,

the spot size of the electron beam, the resolution required, and the type and thickness of the resist among other parameters. In order to fabricate particles with various sizes and thicknesses, a resist of the correct thickness must be used. Hence the correct values of all the other parameters (e.g. the dose), had to be determined by running an exposure test experiment. In the next section, the exposure test experiments done are presented.

### 3.5.1 Program writing

At the Department of Electronic and Electrical Engineering of the University of Glasgow where the electron beam fabrication was done, there are mainly two computer programs used to define the patterns. These are WAM (Wavemaker) which is a windows based program and CATS (Computer Aided Transcription System) which is text based. The program WAM, in spite of its simplicity and visual appeal, is not suitable for the production of millions of particles differing in size and spacing. The most suitable option was to write a text file using CATS. This was done for all the patterns obtained in this study.

### 3.5.2 Resist spinning

A double layer resist of PMMA was spin coated on a silicon substrate. The bottom layer which is composed of PMMA of relatively lower molecular weight (and hence higher sensitivity than the top layer) was spun first. The resist was then baked in an oven at 180$^{o}$ C for at least two hours before being spin coated with the top resist layer. The film was then left overnight in an oven at 180$^{o}$ C to promote adhesion to the substrate. The thickness of the resist, apart from its dependence on the weight percent of the PMMA dissolved on the solvent (either chlorobenzene or xylene), is also a function of the spinning speed. The higher the spinning speed, the smaller the thickness of the resist layer. However the slower the speed, the less uniform the thickness of resist. A balance between these 2 has to be found. In this study a spinning speed of about 2 000 to 5 000 revolutions per minute (rpm) was used. After the sample was baked overnight, it was then submitted to join the queue for exposure by an electron beam. On average, it took about 3 days before the sample was exposed by the electron beam writer.

### 3.5.3 Resist development

A ratio mix of MiBK [$(CH_3)_2CHCH_2COCH_3$) and IPA (Isopropyl Alcohol) which are a solvent and non-solvent respectively of PMMA was used to develop the sample after exposure to the electron beam. An IPA:MiBK ratio mix of 1:1 to 3:1 was used. The 1:1 ratio is the fastest (least contrast), and 3:1 is the slowest (highest contrast). An optical microscope with a maximum magnification of x1000 was used as a first check of the development quality. A more rigorous check the quality of the patterned area undercut, a cut piece of the sample was observed with a SEM at an angle after sputter coating the resist with gold to avoid charging.

Figures 3.5 and 3.6 shows SEM pictures of a resist with no undercut and a good undercut respectively. It is vital to check the quality of the undercut achieved before deposition of an Fe thin film is done.

### 3.5.4 Film deposition

Fe deposition was done using a vacuum system at The University of Glasgow, Physics and Astronomy Department. This evaporation system was chosen over that at Heriot Watt University used under section 2.3 of this report because of the following reasons. (i) It is within walking distance from the department of Electronics and Electrical Engineering of the same university where the electron beam lithography patterning was done and where all the required post deposition facilities are housed. (ii) The evaporation system took about 2 hours to pump down to a pressure of about $2 \times 10^{-6}$ mbar while that at Heriot Watt took about 6 hours.

The low pressure vacuum pumping system is a liquid nitrogen trapped diffusion pump. The vacuum chamber is a bell jar system. The crucible is a resistance heated boat not surrounded by any housing. The system was pumped to a pressure of about $2 \times 10^{-6}$ mbar before heating of the Fe in the crucible was started. Upon heating, the pressure increased to around $0.8\text{-}2 \times 10^{-5}$ mbar. This is the pressure at which the deposition was done.

A quartz crystal oscillator was used to monitor the thickness during deposition. After deposition, a DekTak surface profilometer was used to check the actual film thickness to an accuracy of at least +/- 10 % of the thickness value. A more accurate (up to about +/- 2 %) determination of the

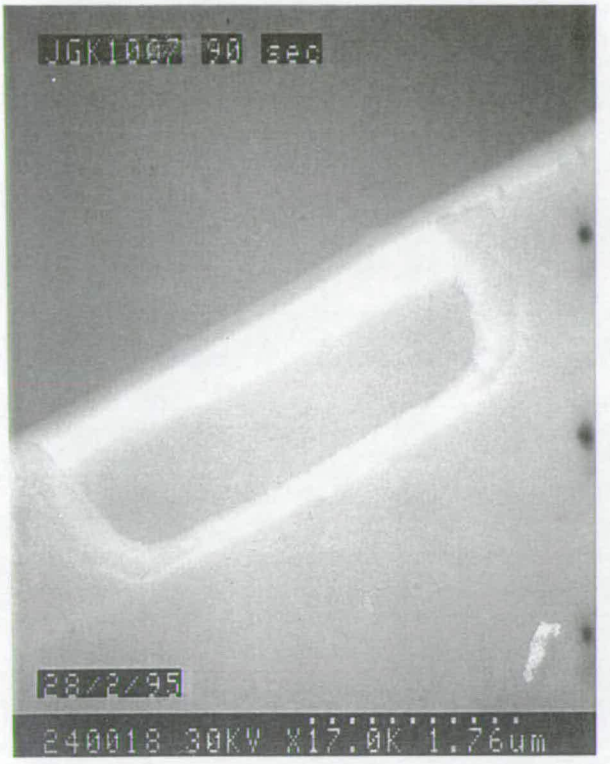


**Figure 3.5** A SEM showing a side view of a window on the resist on top of a silicon substrate. There is no undercut (see text for explanation).

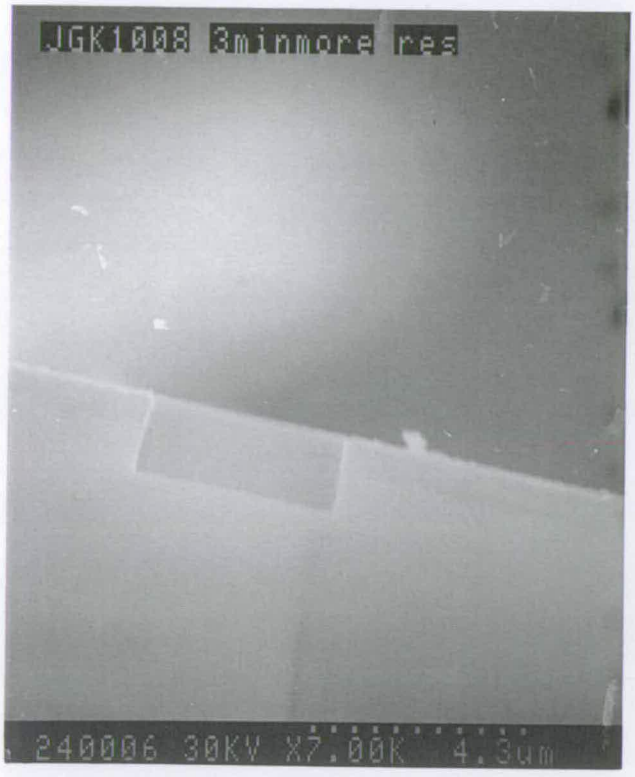


**Figure 3.6** A SEM showing the window where the resist on a silicon substrate had been removed during development. A good undercut is evident from this picture.

patterned particles was obtained by observing with a SEM. Thin films (0.05 -1 μm thickness) were deposited on the substrate while performing exposure test experiments. The experimental pressure was about 0.8 $x10^{-5}$ mbar. The particles used for exposure test experiments were in the size range 0.05 - 4 μm.

The lift-off process was done using acetone. Chlorobenzene, which also dissolves PMMA, was tried in this study and was found to be not much better than acetone. Since chlorobenzene is a well-known carcinogenic fluid it was not chosen for use in the lift-off process of this study. The lift-off process involved placing the sample in acetone at a temperature of $46^{o}$ C. After 5 minutes a pipette was used to squeeze some acetone over the sample to get rid of the loose Fe layer from the top of the dissolved resist. The sample was then transferred to a fresh container of acetone and left there for about half an hour. The sample was then viewed under an optical microscope still in the acetone fluid to roughly check the lift-off progress. If the lift-off seemed not complete, the sample was then placed in an ultrasonic bath for a few minutes before being transferred to another fresh container of acetone for rinsing. It was then very quickly transferred to a container with IPA and later de-ionised water. The final rinsing was done by passing de-ionised water from a tap over the sample. It was then blow dried by using compressed nitrogen gas.

A rough check of the quality of the patterned area and particles (where possible), was done using an optical microscope. High resolution observations of the particles were done using an SEM (Hitachi S800). As pointed out in chapter 2, section 2.5, the conversion from Fe to magnetite was done using annealing method 1 in the early part of this study. This method was later abandoned in favour of method 2. **It should be noted here that unless otherwise clearly stated, the lithographically produced samples reported hereafter and as well the rest of this thesis, are those obtained using annealing method 2.**

From chapter 2, section 2.5.2, lithographically produced arrays of magnetite particles of this study are expected to be single crystals. Using an SEM, no grains were observed in any of these particles. Argyle and Dunlop (1990) used a similar environment to that of method 2 to convert $Fe_2O_3$ (of about 0.5 μm) to $Fe_3O_4$. They found that the magnetite grains produced were consistent with single crystal pure magnetite.

In general, an increase in the sample dimensions of up to 0 - 30 % was observed after the Fe particles have been converted to $Fe_3O_4$ using method 2. As pointed out in chapter 2, section 2.5.2, the Fe fine grains join together when annealed using method 2 and thus closing the inter-grain spacing which existed before annealing the Fe. The effect of such space closure with magnetite material is to reduce the size of a particle, however, the effect of the change of crystal structure from that of Fe to that of $Fe_3O_4$, is to increase the particle size. Thus the total size of the resulting magnetite particle when Fe is annealed depends on these two opposing effects. The possibility of particle size increase due to annealing had to be considered at the EBL resist patterning stage. This was done by producing several patterns whose sizes were in the vicinity of the targeted magnetite particle size.

Magnetite particles produced in this study were stored in either a desiccator or ethanol alcohol to avoid oxidation during storage. The latter method of storage provided better protection than the former.

Figure 3.7 shows a SEM picture of an array of 4 μm x 4 μm x 1 μm magnetite particles produced in preliminary edge definition experiments. It can be seen from the close-up of one such particle (Figure 3.8), that the edge of the particle can be accurately defined to an error of less than 5%. Figure 3.9 shows a top view of an array of lithographically produced 0.2 μm cubic magnetite particles while Figure 3.10 shows a side view of the same sample. The ability to produced many particles with very few missing and as well the uniformity of the height of the particles produced, is evident from these figures. It is vital to check the samples from the side to determine particle quality since a top view alone may not reveal any 'flanks' resulting from the lift-off process.

The aim was to produce groups of $Fe_3O_4$ particles in the size range 0.04 to 4 μm with the following shapes: (a) cubic and (b) rectangular parallelepiped. In both groups of particles the inter-particle spacing was to vary as much as possible. The assumption was that the particles with the greatest possible inter-particle spacing would simulate non-interacting particles, and that the array with the least inter-particle spacing would simulate interacting ones. The process of production of full scale samples is similar to that of the exposure test described above. The difference is mainly in the size of the sample. In the next section the focus will be on the problems encountered in the production of these samples and the solutions attempted.

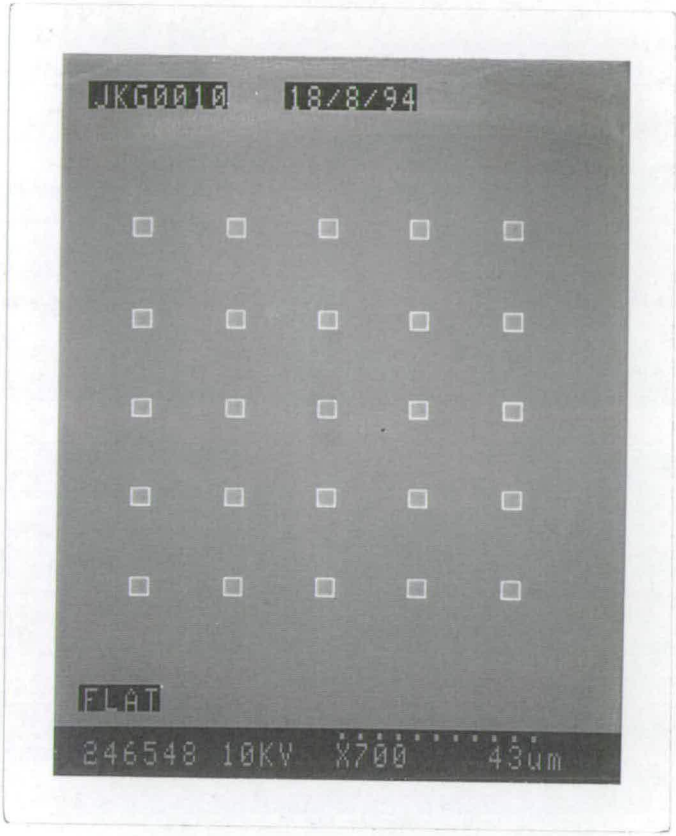


**Figure 3.7** SEM picture of an array of 4 μm x 4 μm x 1 μm magnetite particles produced in exposure test experiments.

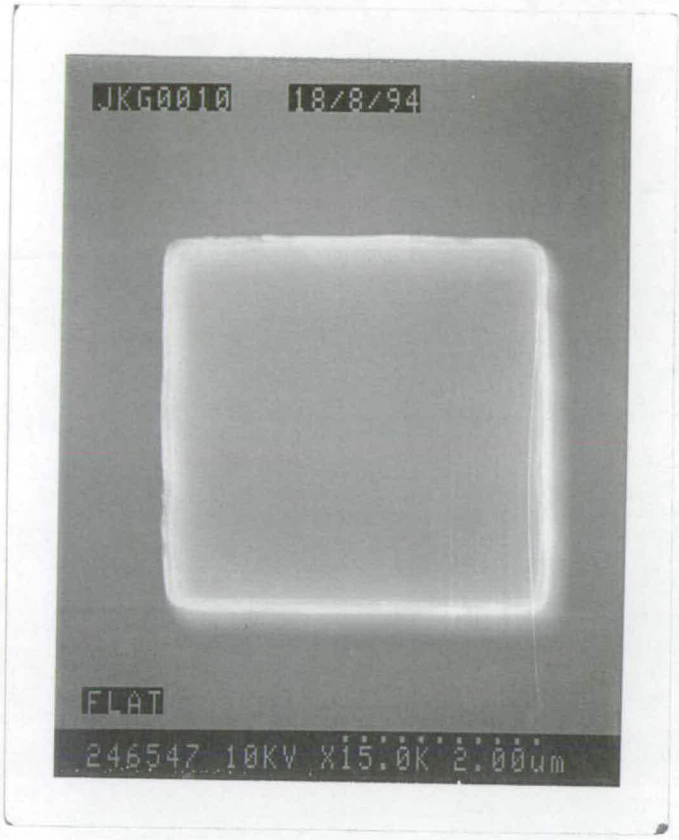


**Figure 3.8** SEM picture of a 4 µm x 4 µm x 1 µm magnetite particle showing a good edge definition. The edge can easily be measured to an error of less than 5% of the particle size.

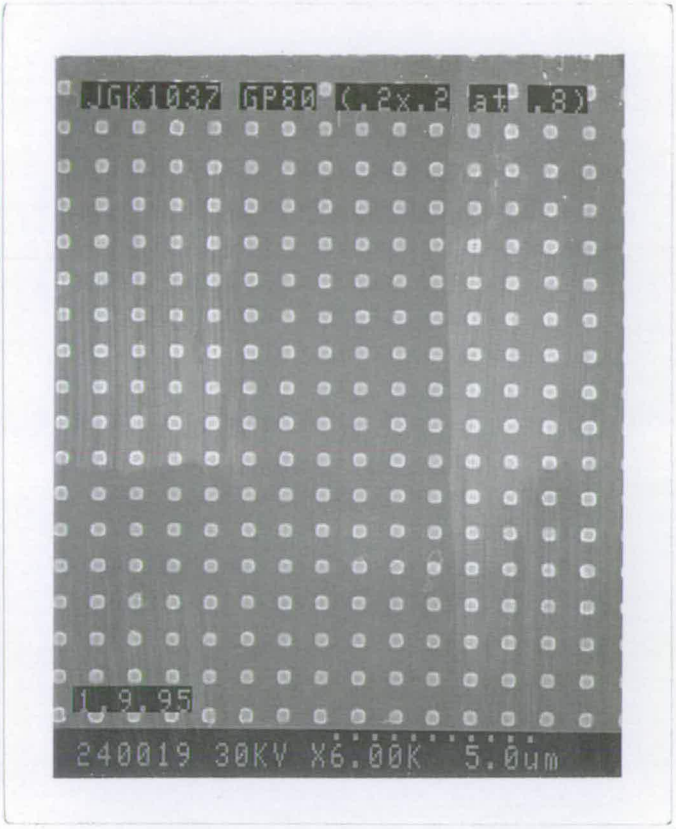


**Figure 3.9** A SEM picture (top view) of lithographically produced arrays of 0.2 μ cube magnetite particles.


**Figure 3.10** A SEM picture (side view) of lithographically produced arrays of 0.2 μ cube magnetite particles.

## 3.6 EBL fabrication of magnetite arrays - full size sample fabrication

### 3.6.1 Sample Size

The sample size had to be about 2 mm x 2 mm in order to fit on the sample holder of the alternating gradient force magnetometer (AGFM). Another requirement was that the number of Fe particles in a sample and consequently $Fe_3O_4$ particles obtained after heat treatment should have a sufficient total magnetic moment such that their remanent magnetisation would be detectable by an AGFM. So the aim was to produce a sample with a total moment of at least 1 x $10^{-9}$ $Am^2$. Figure 3.11 shows a plot of the number of particles required in order to have a total moment of 5 x $10^{-9}$ $Am^2$ in a sample as a function of particle size. For a sample with cubic particles of 0.04 μm size, about 160 million squares have to be exposed by the electron beam writer. The time required to expose a single area of 2 mm x 2 mm with 160 millions squares is about 150 hours. This time is not practically feasible. The high resolution resist PMMA could not be easily lifted-off if the maximum film deposited was more than 1.5 μm. Due to the limitations pointed out above, most of the samples reported in this study have their width in the size range 0.1 - 1 μm.

The 2 mm x 2 mm sample size limitation means that there is a limit on the greatest inter-particle spacing possible. Hence in this study, an inter-particle spacing of 4 times the particle size was used to simulate non-interacting particles. This spacing is considered to be sufficient since the magnetostatic function varies as an inverse square of the distance from the particle. Theoretical studies have shown that magnetostatic interaction start to be significant at an inter-spacing of about 1 times the particle size (Stevenson, 1994).

### 3.6.2 Sources of lift-off problems

Once a proper undercut of a resist has been achieved, the major source of problems of lift-off occur during the Fe film deposition. The main causes of these problems are briefly described below.

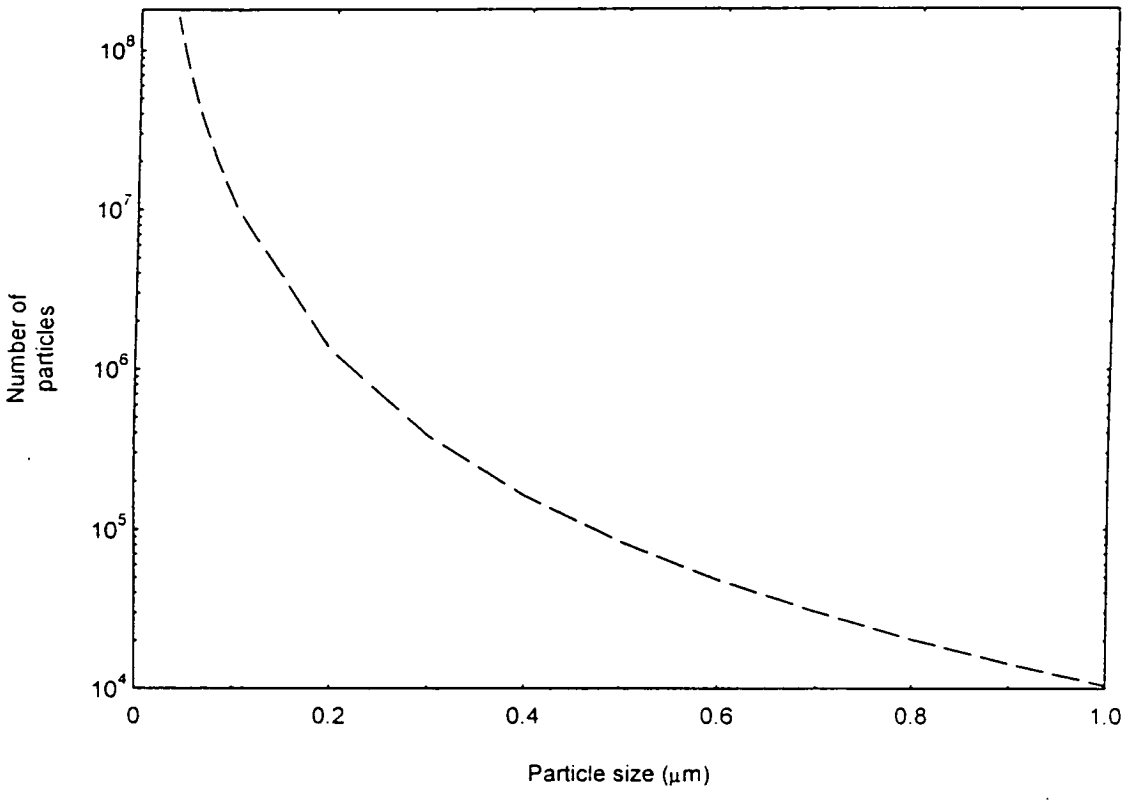


**Figure 3.11** A log-linear plot showing the number of magnetite particles which result in a total magnetic moment of $5 \times 10^{-9}$ $Am^2$.

### 3.6.2.1 90° angle of incidence requirement

In order for the evaporated Fe to be shielded by the resist undercut, the atoms (or diatoms) should strike the substrate at an incident angle $\phi$ (shown in Figure 3.12) whose value is as close to 90° as possible. The angle $\phi$ should not be less than the undercut angle $\theta$ for a good lift-off to occur. In this study $\theta$ was calculated from the resist undercut such as the one shown in Figure 3.6 and was in general about 5°. For a fixed value of $\phi$, the size of the area subtended by the solid angle $\phi$ at the substrate increases with the source to substrate distance. Hence ideally one would want the substrate to be as far away as possible. This would make possible deposition of the same thickness on all the samples simultaneously.

Unfortunately, the further away the substrate is from the source, the more chance of collision of the evaporating Fe atoms with the residual gas at a given pressure (i.e. the distance could be far greater than the mean free path), hence one has to balance these two opposing effects. In this study a source to substrate distance of about 14 cm was used. At a shorter source to substrate distance the heat due to the source would cause the resist to flow and thus destroy the sample patterns. This problem occurred when a thicker film than 0.2 μm was required. The need to use a large sized crucible (about 8 mm diameter) in order to fit enough Fe for a thicker than 0.2 μm deposit, made the temperature increase during deposition worse. For a thin film of less than 0.2 μm, a smaller crucible (about 3 mm diameter) was used. The heat generated by this crucible was did not cause problems. To reduce the heat generated during deposition of thicker than 0.2 μm films, an aluminium foil housing was constructed around the crucible. The housing was of a temporary nature and could be placed to cover the evaporating source and taken off at ease. This suited other users of the evaporation system who did not need such a housing.

### 3.6.2.2 Rate of evaporation of Fe

When too high (>5 nm/s ) or too low (<0.1 nm/s) rates of Fe deposition were used, the deposited film didn't stick very well to the substrate, hence such particles did not survive the lift-off process. When a thicker than 0.2 μm thin film was deposited, the chance that the quartz crystal thickness monitor

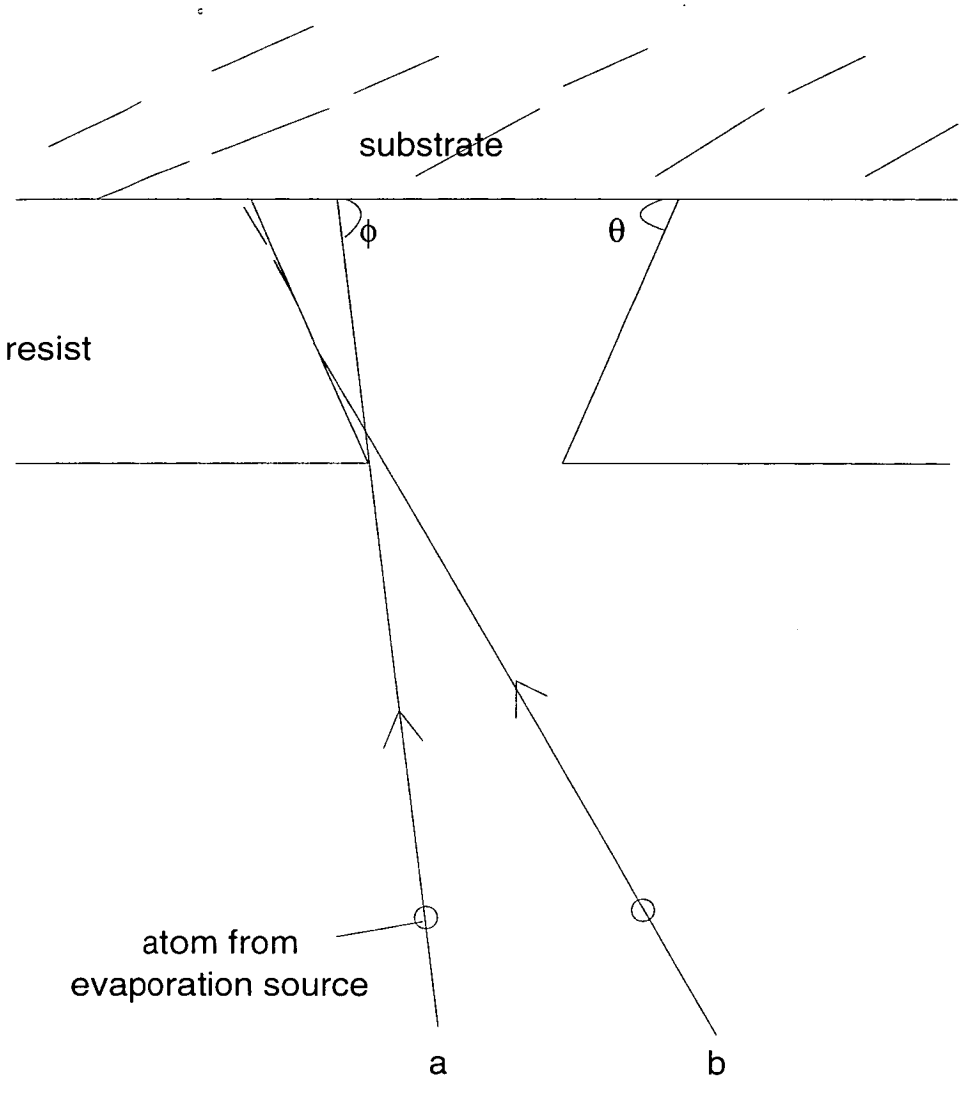


**Figure 3.12** Schematic representation illustrating the problems which could result if the striking angle is not very close to 90 degrees. An atom following path b (i.e. incident angle case $\phi > \theta$), would strike the undercut resist while that following path a would not.

would go off before the experimental run was complete was very high. The thickness of such samples was estimated from the rate of deposition measured before the quartz crystal went off. The assumption made was that the rate of deposition remained constant throughout the experiment. Estimating the thickness from the power applied to heat the crucible was not helpful, because the Fe being evaporated did not always occupy the centre of the crucible upon melting.

## 3.7 Magnetite particles used in this thesis

The dimensions of the particles used in this thesis are shown in Table 3.1. The names of lithographically produced non-interacting cubic particles of magnetite start with the prefix JK while those for rectangular particles start with JKL. The symbol @ after the above mentioned prefix only appears in interacting lithographically produced magnetite particle. Magnetite powders obtained by the methods of hydrothermal recrystallisation, gel ageing and annealing maghemite have names which start with JH, gel and JG respectively. The particles for sample JH>16 are those which remained on top of a 16 μm sieve. A typical example of these particles is shown in chapter 2, Figure 2.9 (a).

## 3.8 Summary

The method of electronbeam lithography has been introduced as a suitable way of preparing magnetite particles with well defined parameters including their spacing. This was confirmed using mainly SEM. Hence it is possible to avoid the problems of particle clumping which are often encountered when artificially produced magnetite powders are used in rock magnetic studies.

| Sample name | Particle's dimensions (μm) | Inter-particles spacing (μm) |
|---|---|---|
| JK0.1 | cube edge 0.1 | 0.4 |
| JK0.2 | " " 0.2 | 0.8 |
| JK0.3 | " " 0.3 | 1.2 |
| JK0.5 | " " 0.5 | 2 |
| JK1 | " " 1 | 4 |
| JK0.25@0.05 | " " 0.05 | 0.05 |
| JK0.6@≈0.0 | " " 0.6 | ≈ 0.0 |
| JK1@0.25 | " " 1 | 0.25 |
| JKL0.1x0.5 | 0.1x0.1x0.5 | 2 |
| JKL0.2x1 | 0.2x0.2x1 | 4 |
| JKL0.3x1.5 | 0.3x0.3x1.5 | 6 |
| KL0.5x2J.5 | 0.5x0.5x2.5 | 10 |
| JKL1x5 | 1x1x5 | 20 |
| JKL0.5@0.6 | 0.5x0.5x2 | Spacing 0.6 by 2 |
| JKL0.5@0.1 | 0.5x0.5x1 | Spacing 0.1 by 0.8 |
| Gel0.2 | Magnetite powder, average particle size 0.2 | N/A |
| JH0.5 | Magnetite powder, average particle size 0.5 | N/A |
| JH1 | Magnetite powder, average particle size 1 | N/A |
| JH>16 | Magnetite powder, average particle size >16 | N/A |
| JG3 | ellipsoidal magnetite powder, 0.12 by 0.34 (minor by major axis) | N/A |
| JG6 | ellipsoidal magnetite powder, 0.084 by 0.530 (minor to major axis) | N/A |
| JSC1 | 2 mm octahedral single crystal from Shetland | N/A |

**Table 3.1** Table showing the dimensions for samples used in this study.

# Chapter 4 Magnetic domain observations

## 4.1 Introduction

In this chapter various techniques of observing magnetic domains are presented. In addition, the results of experiments done in an attempt to observe domains of submicron magnetite particles using a transmission electron microscope (TEM) are presented. The production of magnetite particles involved the deposition of Fe onto a membrane of silicon nitride ($Si_3N_4$) and later annealing the Fe to $Fe_3O_4$. Magnetic domain observations were done using Fe thin films and as well lithographically produced arrays of Fe particles. These Fe samples were later converted to magnetite particles by using annealing method 2 which has been described in chapter 2. Although the method was successful in delineating domains in Fe samples, problems were encountered in observing magnetite samples.

## 4.2 Domain observation techniques

### 4.2.1 The Bitter technique

Magnetic domains were first observed by Bitter (1931). Bitter dispersed fine magnetite particles over the surface of a magnetised specimen (a similar technique to the familiar experimental demonstration of magnetic field in the vicinity of a bar magnet by sprinkling iron filings). This technique which is now referred to as the Bitter technique, was later improved by Bitter (1932), who dispersed the small magnetic particles on alcohol before placing the colloid over the sample. Nowadays water-based colloids such as ferrofluids (from Ferrofluidics Corp, Nashua, USA) are used.

The Bitter technique takes advantage of the stray magnetic fields of Bloch walls intersecting a plane of a stress-free surface. The particles are accumulated at such domain walls under the simultaneous action of magnetic forces and thermal agitation, hence outlining such walls. Although this method is attractive due to its simplicity, it is mainly based on the use of the optical microscope and hence is limited by the resolution of the wavelength of light. Thus the technique is not suitable for observing submicron PSD magnetites which are of interest to this study.

An improvement in the resolution of the Bitter technique has been made by observing dried patterns of domains using a SEM (e.g. Moskowitz et. al., 1988; Soffel, et. al., 1990). However, due to practical problems involved in applying the method to tiny particles in the submicron size range, its use has mainly been limited to larger than 1 μm particles.

### 4.2.2 Magneto-optic methods

To fully explain magneto-optic effects requires a quantum mechanical approach (e.g. Argres, 1955). However, a classical approach is sufficient for most qualitative domain image analysis. Hence the nature of the description given below is classical.

When a plane polarised light beam is incident on the surface of a magnetic specimen whose magnetisation is **M**, the electrons near the surface of the specimen are forced to oscillate parallel to the electric field vector **E,** (Figure 4.1). As a result of the Lorentz force due to this oscillation, a Kerr component (**K**) in the direction given by **E X M** results. Due to this force, the plane of oscillating electrons is rotated and hence the plane of polarisation of the reflected beam is different from that of the incident beam. This effect depends on the orientation of the magnetic induction of a domain. The domains appear as bright and dark areas. If the transmitted light beam is observed, the technique is known as the Faraday effect.

The Kerr technique has been used successfully in rock magnetism by, for example, Hoffmann et. al., (1987). However, since the technique is optical microscopy based, its practical resolution is also limited by the wavelength of light, and hence is not suitable for use in observing PSD in the submicron size range.

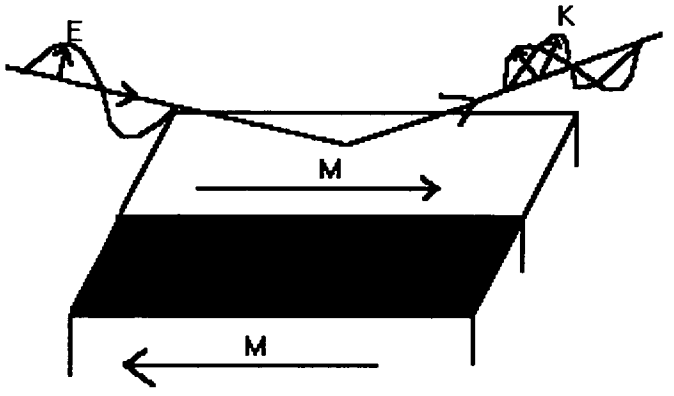


**Figure 4.1** Schematic diagram showing the electric field vector **E** and the Kerr **K** component.

### 4.2.3 Probe techniques

These domain observation techniques involve the mapping of local field variation near the surface of a magnetic material. An example of the probe technique is the Hall probe. When a conductor carrying a current is placed across a magnetic field, a voltage is developed across the conductor in a direction perpendicular to both the direction of the current and the field. This is known as the Hall effect. Hence it is possible to map the field due to magnetic domains using this technique. Although this technique has been used to observe domains with some success, it has not been widely used. This has mainly been due to the difficulties in producing small enough probe tips needed to resolve stray fields due to domains.

An important recent development in domain observation probe techniques is the magnetic force microscope (MFM). The MFM consists of a cantilever with a very fine magnetic tip (diameter of about 50 nm). When the fine magnetic tip is traversed near the surface of a specimen, it experiences a force due to the magnetic field from the specimen domains. Hence by traversing the specimen surface at a suitable height, a contour map of the field variation due to domains can be obtained. A typical height is 80 - 150 nm (Williams et. al., 1992). The spatial resolution of the MFM is about 10 nm (Dahlberg and Zhu, 1995). Hence the MFM can be used to observe PSD with submicron size.

### 4.2.4 Electron beam techniques

The interaction between the electron beam and the magnetic induction can be qualitatively explained adequately by a classical approach even though a full explanation requires a quantum mechanical approach. An electron moving in a region of magnetic induction **B** experiences a Lorentz force given by

$$\mathbf{F} = e\mathbf{v} \times \mathbf{B} \qquad (4.1)$$

where e is the electron charge and **v** is its velocity. Hence a beam of electrons passing through a specimen with horizontally magnetised domains will be deflected as shown in Figure 4.2. It can be seen from this figure that the image plane intensity is high and low below the domain walls. In order to observe this bright and dark contrast, the microscope has to be out of focus. Hence this technique is known as the defused mode (but is more often referred to as the 'Fresnel' mode).

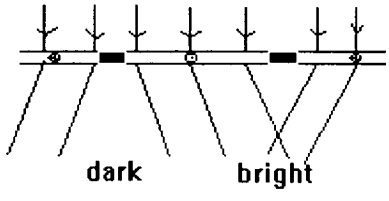


**Figure 4.2** Schematic diagram showing how light rays converge and diverge to produce bright and dark lines at the site of domain walls for oppositely magnetised domains.

If a deliberate off-centring of the objective aperture is done (e.g. Chapman, 1984), a magnetic contrast showing bright and dark areas delineating uniformly magnetised domains (not domain walls) is obtained. This domain observation technique is known as the Foucault mode. For further information on electron microscopy techniques of domain observations, the reader is referred to a review article by Chapman (1984).

## 4.3 Domain observation experiments attempted

In this section the results of experiments done in an attempt to observe domains in PSD particles with submicron sizes are presented. The samples were prepared by depositing Fe on a membrane of silicon nitride and later converting the Fe by oxidation annealing method 2 see chapter 2, section 2.5.2. Magnetic domains were observed on Fe samples (before conversion) and as well magnetite particles (obtained by conversion of Fe). The idea was to observe domains for a thin film and then on lithographically produced arrays of magnetite particles of various sizes from several microns to submicron. As will be shown in the sections below, there were no problems in observing domains in Fe while problems were encountered in observing the magnetite samples.

### 4.3.1 Sample preparation - a brief description

In order to observe magnetic domains using TEM, the thickness of the magnetic sample has to be very thin (< 0.1 μm ). It is therefore necessary to deposit the Fe which is later converted to $Fe_3O_4$ in a very thin membrane. In this study, a thin membrane (30 - 100 nm thick) of silicon nitride ($Si_3N_4$) was used. In Figure 4.3 a schematic diagram of the process of membrane production is shown. Basically a resist is spun on a silicon substrate whose surface layer is silicon nitride [Figure 4.3 (a)]. A window is then etched at the bottom and the resist dissolved [Figure 4.3 (b)].

A thin film of Fe was deposited by the vacuum evaporation technique described in chapter 2, section 3.5.4. The electron beam lithography technique described in chapter 3 was used to produce arrays of parallelepiped magnetite particles on silicon nitride membranes. In order to avoid charging problems while observing domains of arrays of magnetite particles on a silicon nitride membrane, a carbon thin film (about 30 nm) was deposited on the bottom of the membrane.

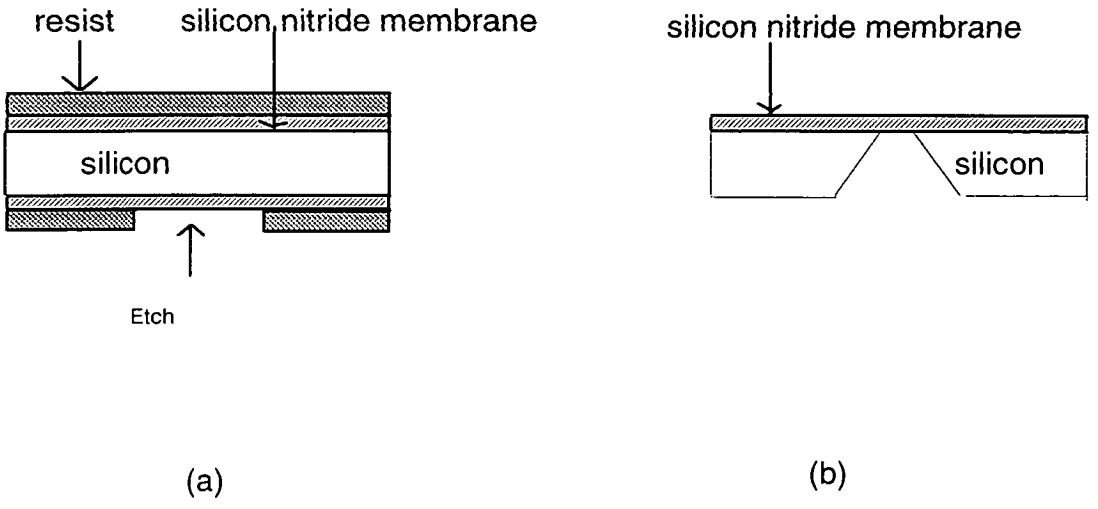


**Figure 4.3** Schematic diagram showing the process of production of a silicon membrane window by etching.

### 4.3.2 Thin film domains

The TEM equipment used in this study is housed at the Department of Physics and Astronomy (University of Glasgow). It is a JEOL 2000 FX equipped with a specially designed objective lens for use with magnetic specimens ((Tsuno, et. al., 1983; Hefferman et. al., 1991) .

Figure 4.4 shows a typical Foucault image of domains observed on an Fe thin film. The dark and bright areas delineate the regions of magnetic domains whose directions of magnetisation are opposite. Figure 4.5 shows Foucault image for the sample shown in Figure 4.4 after the film was converted from iron to magnetite by annealing using method 2. While some of the white regions seen in this figure may be representing domains magnetised in different directions from the black regions, some of the white areas (e.g. the one marked with a cross **x**, pointed by an arrow), are regions without any material but just membranes The magnetic material in these areas have lifted off during the process of converting the Fe to magnetite at 600$^{o}$ C. The distortions of the silicon nitride membrane during the heating or cooling process might be responsible for this missing magnetic material. These problems made any sensible domain observation difficult. Hence silicon nitride membranes are not very suitable for the productions of

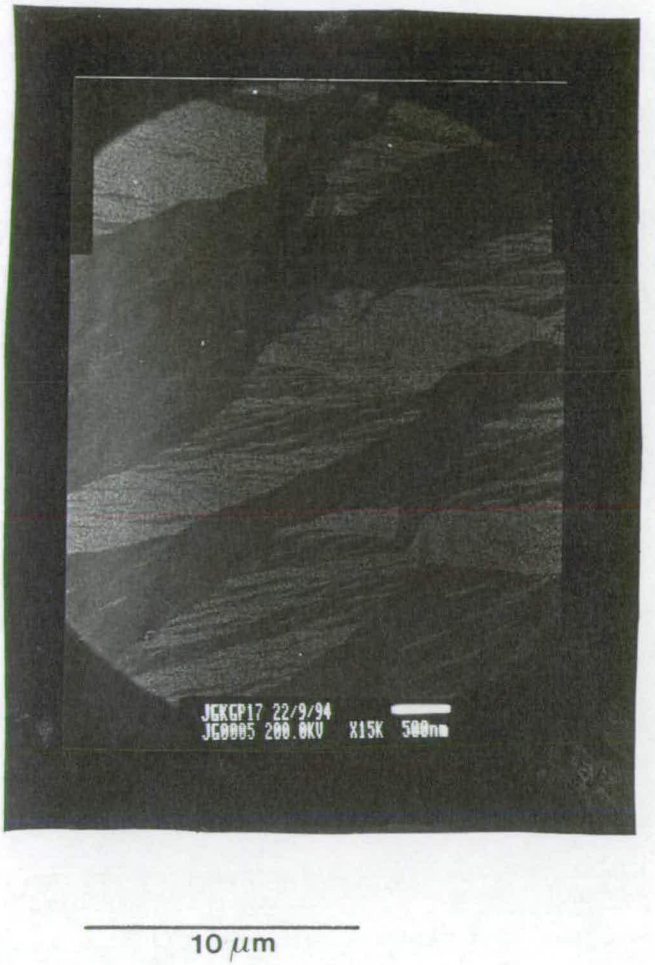


**Figure 4.4** A typical Foucault image of domains observed on an Fe thin film deposited on a silicon nitride membrane. The scale bar shown in the picture is 4 times larger than the actual scale shown below the picture.

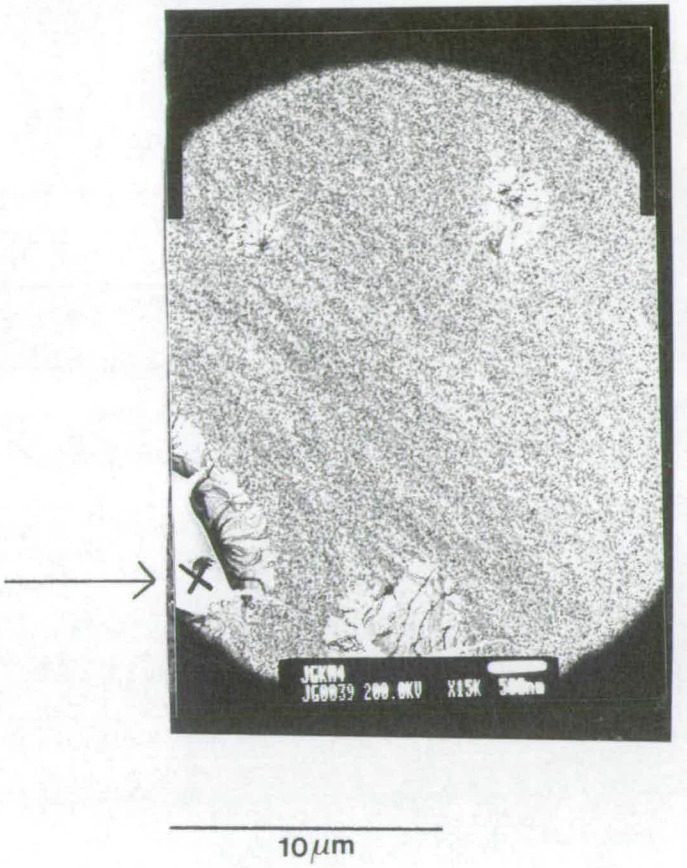


**Figure 4.5** A Foucault image of the sample shown in Figure 4.4 after it was converted to magnetite by annealing at 600 $^{o}$C. Note that the scale bar shown in the picture is 4 times larger than the actual scale which is shown below the picture.

magnetite particles via the method which requires high temperature annealing of Fe.

### 4.3.3 Domains of arrays of Fe and Magnetite particles

Figure 4.6 (a) shows an array of 5 μm x 5 μm x 0.05 μm of Fe particles. A Foucault image of the domains in one such particle is shown in Figure 4.6 (b). Domains magnetised in opposite directions are shown by bright and dark regions. After converting the Fe to $Fe_3O_4$, no domains were obtained mainly because of problems resulting from heating the thin membrane at 600° C during the conversion of Fe or $Fe_3O_4$.

The silicon nitride membrane when heated to convert Fe particles to magnetite get distorted and in most cases crack and break. Hence the magnetite particles produced on these thin silicon nitride membranes are under stress and often contain cracks. Hence silicon nitride membrane is not a substrate for production of magnetite particles via the method of annealing of Fe at elevated temperatures.

## 4.4 Summary

Magnetic domains of Fe thin films and arrays of lithographically produced parallelepiped particles were observed without any problems. However difficulties were encountered in observing domains on $Fe_3O_4$ samples produced by annealing Fe at 600° C. The problems are mainly brought by the heating during the Fe to $Fe_3O_4$ conversion. Solving these problems would require finding a suitable way of producing isolated particles of magnetite at room temperature, an attempt made without success in this study (see chapter 2, section 2.3). It may be more appropriate to try other high resolution domain observation methods such as using the MFM in future studies since no thin membranes are required in such experiments.

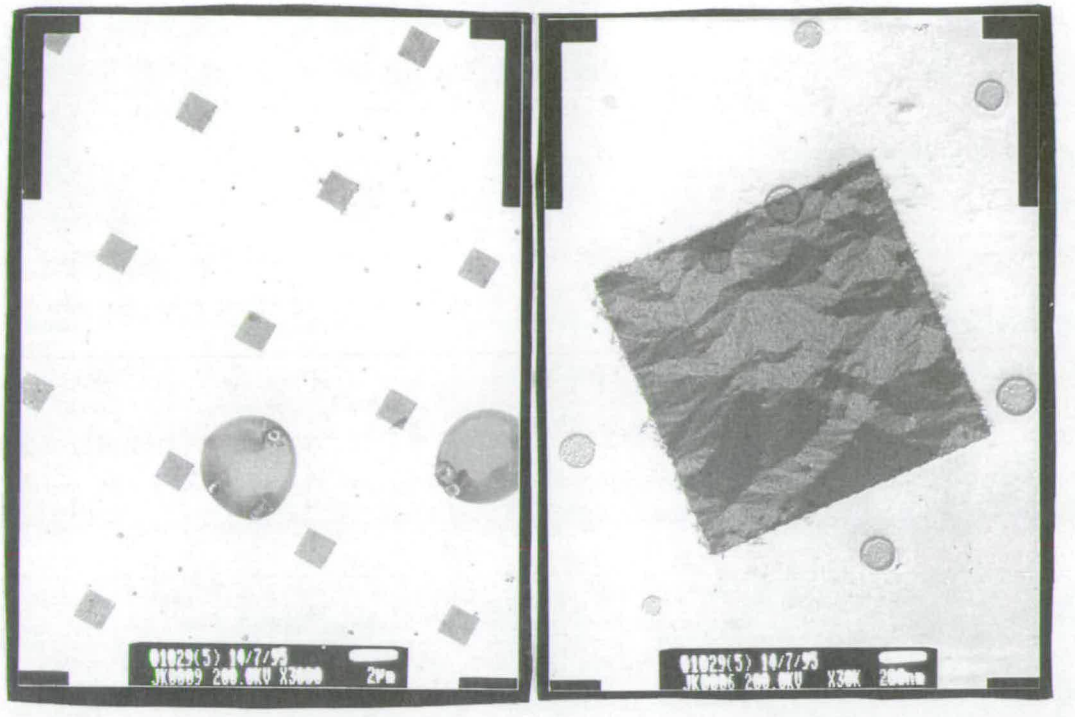

25$\mu$m

2·5$\mu$m

(a) (b)

**Figure 4.6** (a) A transmission electron microscope picture of an array of 5 μm x 5 μm x 0.05 μm particles of Fe and (b) a Foucault image of one such particle. Note that the scale bar shown in the picture is 4 times larger than the actual scale which is shown below the picture.

# Chapter 5 Low temperature magnetic properties of magnetite

## 5.1 Introduction

In this study a sample with a continuous thin film is referred to as 'a thin film'. This should not be confused with a sample composed of arrays of particles.

In order to isolate the primary magnetic remanence (i.e. the more stable remanence and hence more ancient), in rocks from secondary components (less stable), two techniques are often employed. This practice is often referred to as 'magnetic cleaning'. One technique is the stepwise alternating field (af) demagnetisation (e.g. Creer, 1959) and the other is thermal demagnetisation (e.g. Thellier, 1966). Apart from these two techniques, magnetic cleaning of samples whose major remanent magnetisation carrier is magnetite can be obtained by zero-field cycling from room temperature to a temperature much lower than the low temperature transition for magnetite (reported to be near 120 K, see section 5.3). Although several studies (e.g. Ozima et al., 1964; Kobayashi and Fuller, 1968; Merrill, 1970), have recommended this technique as an effective means of 'magnetic cleaning', it has not become a standard routine technique. This is partly due to the lack of a clear understanding of the behaviour of magnetite particles at this low temperature transition.

Previous experiments by other researchers have used magnetite powders (e.g. Morrish and Watt, 1958; Heider et al., 1992; Özdemir, et al., 1993). In such powders, it is always possible to attribute any discrepancy between the results observed and theory to possible existence of magnetostatic interaction effects or existence of elongated particles in samples presumed to contain only equant particles. Such factors need to be eliminated in order to determine low temperature behaviour of magnetite particles.

In this chapter, the results of low temperature magnetic properties of lithographically produced arrays of both interacting and non-interacting cubic magnetite particles, are presented. Where appropriate, the results of the magnetic measurements of these samples are compared to those for thin magnetite films, artificially laboratory grown magnetite powder particles

and natural magnetite crystals. In addition, comparison is extended to include results from studies by other researchers. Also presented is the results of the experiments done in order to determine the Curie temperature although such a process is a high temperature process.

The results show a gradual increase in the amount of saturation isothermal remanent magnetisation (SIRM) lost at the Verwey transition $T_V$ (see section 5.3 below) with increasing particle size in the PSD size range. This behaviour which is similar to that observed by Özdemir et al., 1993, and ascribed to partial oxidation of the particles, is here interpreted as being most likely a reflection of the domain structure of these particles which is predicted to be of vortex state (e.g. Williams and Dunlop, 1989, 1995). The grain size dependence of the amount of SIRM lost at $T_V$ is most probably what has been reported by previous researchers (e.g. Dunlop and Argyle, 1991, Heider et al., 1992, Özdemir et al., 1993), as a magnetic memory particle-size dependent trend. Magnetic memory measured during the cooling and warming process is shown to be a stress related phenomenon. Such measurements may be useful in assessing the nature of stress in a magnetite sample.

## 5.2 High temperature magnetic measurements

The interest in high temperature magnetic measurements in the present study was limited to its use as a way of characterising the magnetite produced. When a magnetite sample is heated, at a temperature of about 580$^{o}$ C (the Curie point for magnetite), it loses all its magnetisation. This loss in spontaneous magnetisation is due to thermal agitation overcoming the exchange energy. This high temperature transitional change is used often in rock magnetism to determine if a rock contains the mineral magnetite. The major problem in using this method is the possibility of chemical alteration of the sample during the heating. Small unprotected grains of magnetite convert to maghemite which in turn converts to hematite on heating to above 300$^{o}$ C.

In this study, the Curie point was determined using samples of thin films of magnetite obtained by converting Fe thin films using annealing method 2 (see chapter 2 for the description of this method). A susceptibility meter model MS2 from Bartington connected to a heating system model MSWFP from the same company was found to be easier to use for the

determination of the Curie point than using the Curie balance. It is easier to pass nitrogen gas over a sample during an experimental run in this instrument and hence avoiding oxidation of the sample which could lead to chemical alteration. It is often necessary to house the whole Curie balance equipment in either a vacuum or an inert gas environment.

A schematic arrangement of the equipment used is shown in Figure 5.1. A typical plot of normalised susceptibility is shown in Figure 5.2. The Curie temperature was found to be $580^{o}$ +/- $12^{o}$ C which is in good agreement with the literature value of $580^{o}$ C for magnetite (Thompson and Oldfield, 1986). Due to their weak total magnetic moment, samples of arrays of magnetite were not used for the Curie point determination. It was assumed that the Curie point for thin films of magnetite which was obtained by annealing Fe in a gas mix ratio of 100:6 carbon-dioxide to hydrogen (Chapter 2, section 2.6.2) was the same as that for lithographically produced arrays of magnetite particles annealed under the same environment.

## 5.3 Verwey transition and stoichiometric magnetite

Stoichiometric magnetite exhibits abrupt changes in magnetic properties near 120 K, (Özdemir, et. al., 1993, RadhaKrishnamurty, 1981; Hodych, 1986). This temperature is known as the Verwey transition temperature, (Verwey, 1939, O'Reilly, 1984). Associated with these magnetic changes is the change in crystal structure from cubic to monoclinic (upon cooling of the sample) and as well the isotropic point (i.e. the temperature where the first magnetocrystalline anisotropy constant $K_1$ becomes zero). The Verwey transition is a signature for magnetite. Unlike in the Curie point determination, there is no risk of chemical alteration of a sample since it is not heated. Hence the process is more appropriate than the Curie point determination for use in lithographically produced magnetite particles of this study which easily oxidise on heating unless protected. The Verwey transition temperature in this study was obtained using a Magnetic Property Measurement System (MPMS2), Superconducting Quantum Interference Device (SQUID), from the company Quantum Design. This instrument is more sensitive than the susceptometer used to determine the Curie point.

SEM pictures of typical samples of lithographically produced non-interacting cubic magnetite particles used in this chapter are shown in Figures 5.3 and 5.4. These samples were cooled from 300 K through the

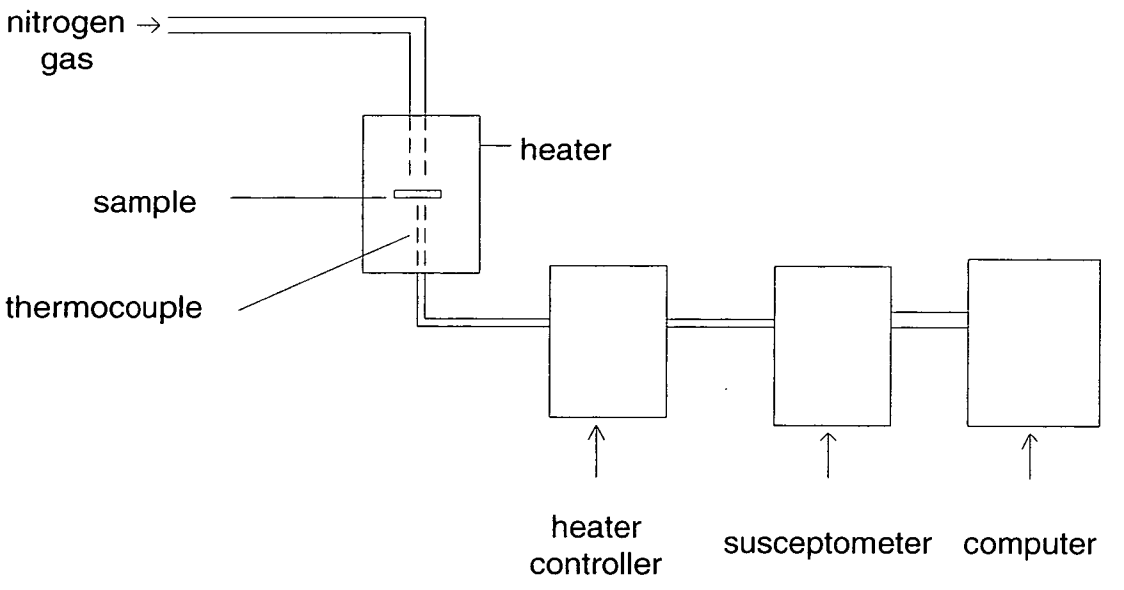


**Figure 5.1** Schematic representation of the experimental arrangement which avoided the possibility of mineral alteration during the determination of the Curie temperature. The Bartington heater and susceptibility meter were connected to nitrogen gas.

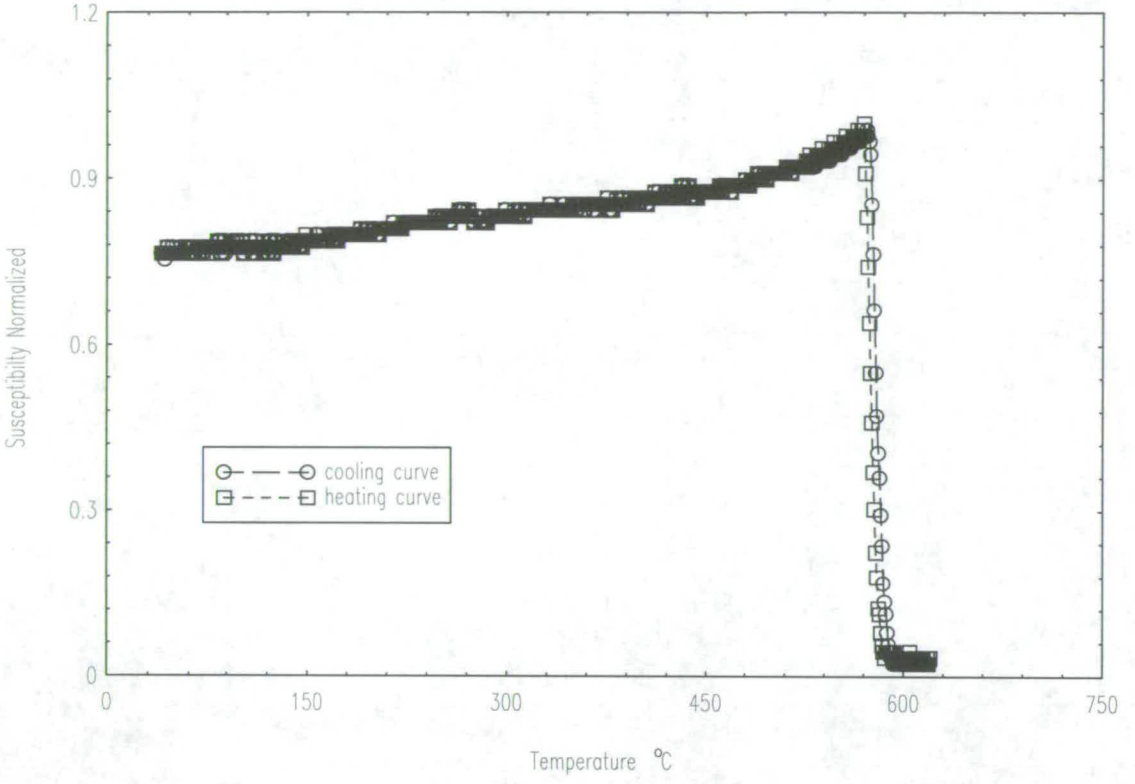


**Figure 5.2** Susceptibility normalised to the largest value during the heating and cooling cycle. The plot also shows that the samples are stable in a $N_2$ environment. A Curie point of 580 $^{o}$C was obtained.

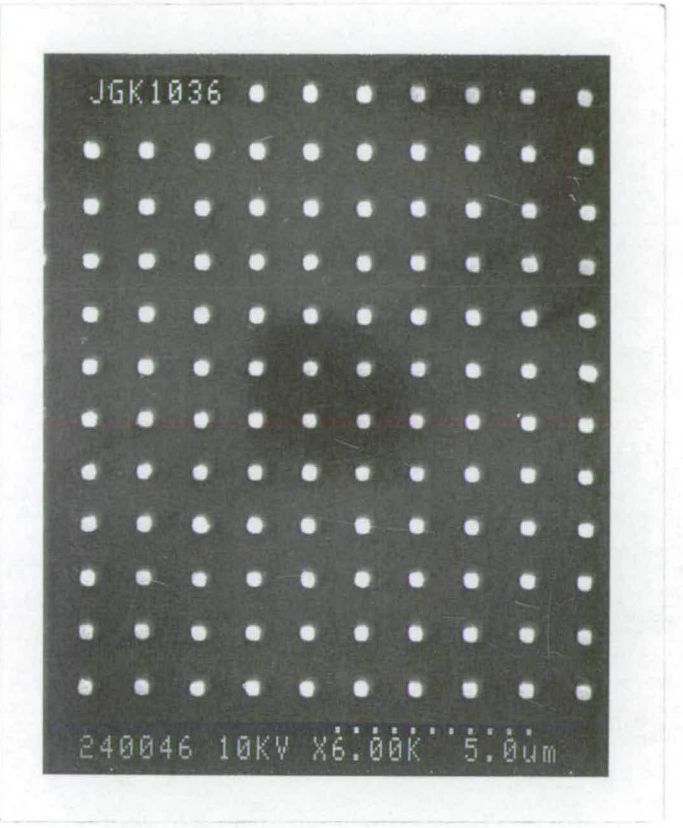


**Figure 5.3** SEM picture of an array of 0.3 μm cubic magnetite particles at a spacing of 1.2 μm.

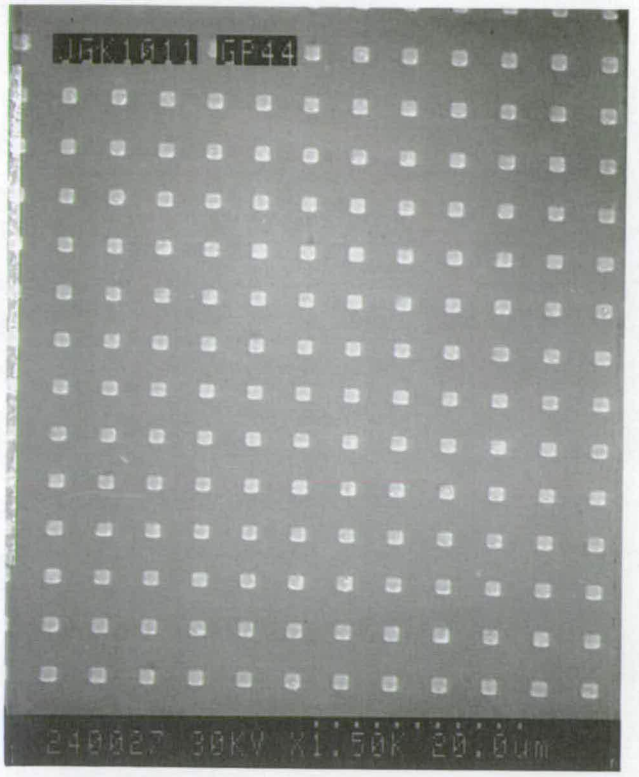


**Figure 5.4** SEM picture of an array of 1 μm cubic magnetite particles at a spacing of 4 μm.

Verwey transition in a zero magnetic field environment. A sample was given a SIRM in a field of 1Tesla (T) at a low temperature before warming it through the Verwey transition in zero field. While the majority of samples had their SIRM measured from 20 K to 170 K, some experiments were done in the temperature interval 1.8 K (or 5 K) to 300 K. This was done in order to check for the presence of superparamagnetic particles or hematite. Moskowitz et al., 1993, observed that the presence of superparamagnetic magnetite particles in a sample lead to a rapid decrease in SIRM in the temperature interval 5 to 40 K. This behaviour was ascribed to the distribution of blocking temperatures due to different sizes of SPM particles. By starting from 1.8 K, the existence of even the smallest sized SPM in a sample was expected to be observed. Since there are no reported SIRM measurements done below 4.2 K for magnetite in the literature, it was also interesting to check if the expected behaviour of SIRM continues in this temperature range. If hematite is present in a sample, a loss of the SIRM intensity near 260 K; the so-called Morin transition (Morin, 1950; O'Reilly, 1984) is expected.

Figure 5.5 shows thermal demagnetisation of SIRM intensity given in a field of 1 T, for sample JK0.5. The sample was warmed from either 1.8 K to 300 K or from 20 K to 170 K. It can be seen from this figure that, when the sample was warmed from 20 K, a relatively larger SIRM intensity was lost while approaching the Vervey transition than when the sample was warmed from 1.8 K. There is neither a big decrease in SIRM intensity below 40 K indicative of the presence of superparamagnetic sized particles (reported to be about 30 - 40 % by Özdemir, et. al., 1993), nor a transition near 260 K which could be due to hematite. This observation is in agreement with results of XRD data of co-produced magnetite thin films (see chapter 2).

Figure 5.6 shows SIRM intensity given at 20 K in a field of 1T during warming in zero field to 170 K (or 300 K), for lithographically produced samples. Typical curves for arrays of magnetite particles with the following cube sizes 0.1, 0.2, 0.3 0.5 and 1.0 μm (i.e. samples JK0.1, JK0.2, JK0.3, JK0.5 and JK1 are shown together with that of a 0.5 μm thin film. All the curves in this figure exhibit a sharp drop in SIRM near 120 K. According to Aragón et. al., 1985, the effect of non-stoichiometry on SIRM is to shift the Verwey transition to lower temperature values as shown in Figure 5.7. Using this figure, the non-stoichiometric value $\delta$ for these samples is zero, hence they are stoichiometric. This result is consistent with the results of XRD (see

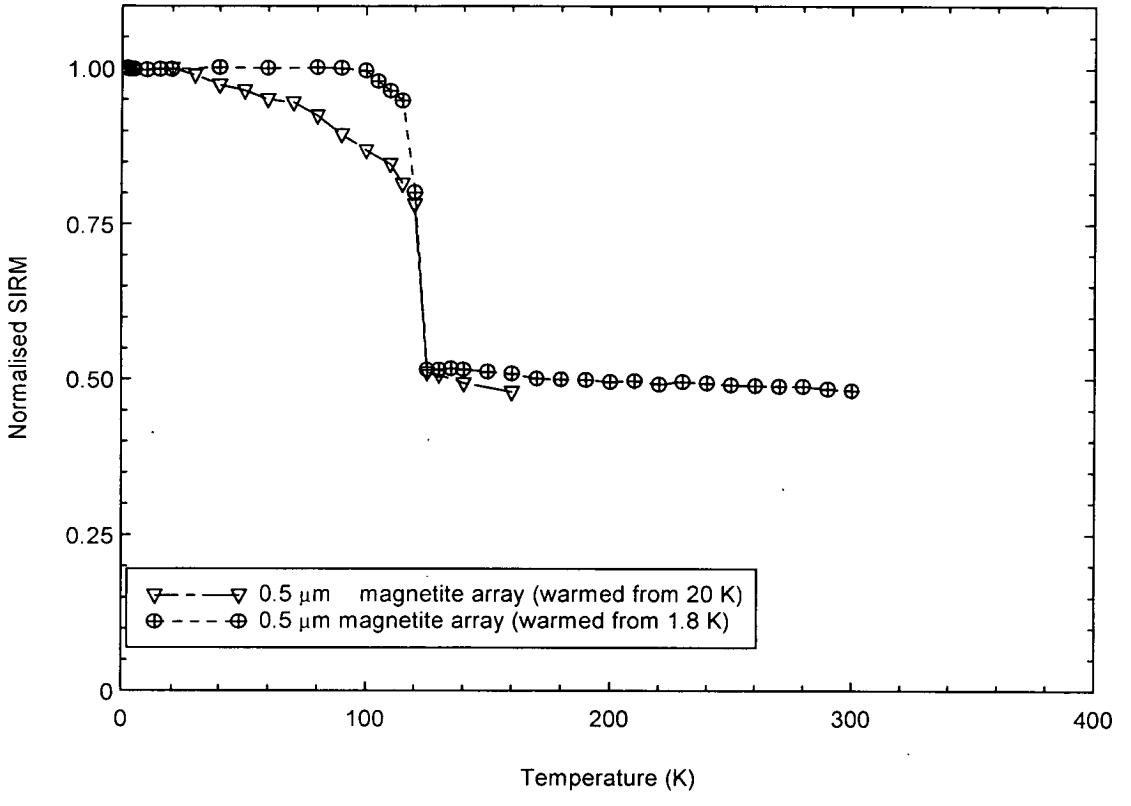


**Figure 5.5** Thermal demagnetisation of SIRM given at 1.8 K in a field of 1 T for a sample composed of arrays of 0.5 μm magnetite particles (i.e. sample JK0.5). There is neither the rapid decrease in SIRM below 40 K expected if SPM are present, nor the sharp drop in SIRM expected near 260 K if hematite were present. The curve for the sample which was given SIRM intensity at 20 K show more loss in SIRM as it approaches the Verwey transition temperature than that for 1.8 K.

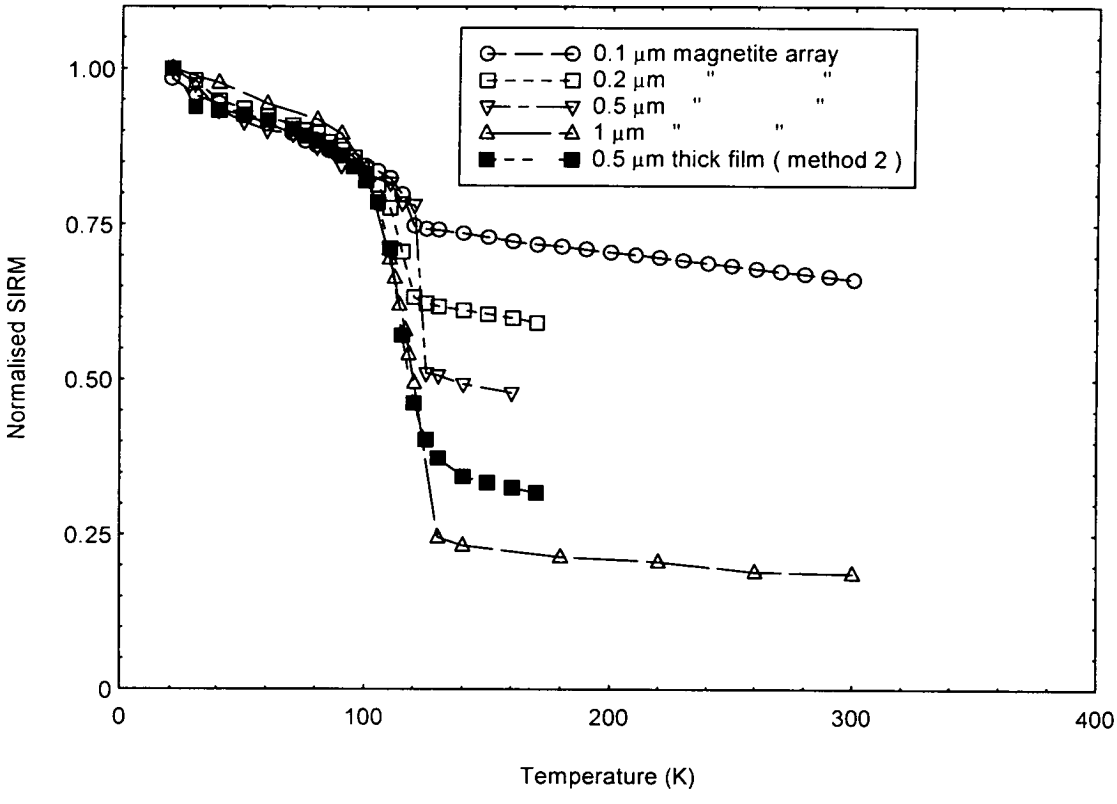


**Figure 5.6** Thermal demagnetisation of SIRM intensity for lithographically produced non-interacting cubic magnetite particles of size 0.1 μm, 0.2 μm, 0.5 μm and 1 μm (i.e. samples JK0.1, JK0.2, JK0.3, JK0.5 and JK1 respectively), and as well that for a thin film. A sharp drop in the SIRM intensity lost at the Verwey transition is evident.

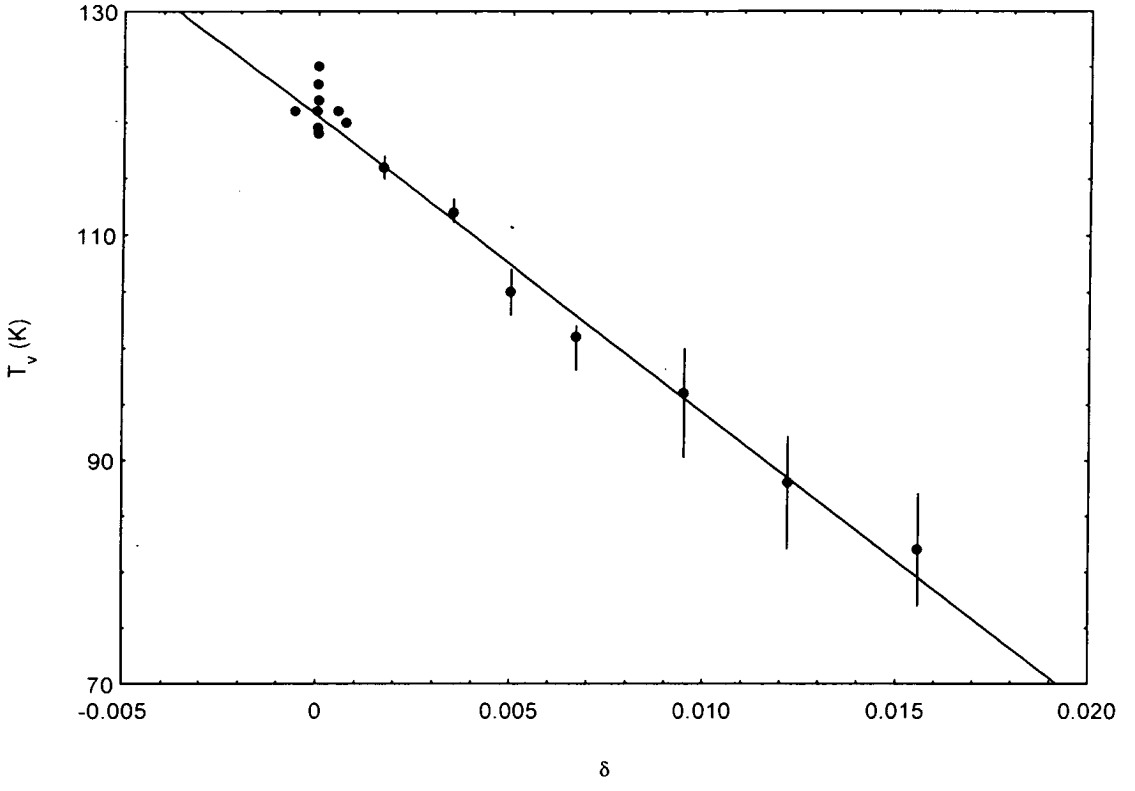


**Figure 5.7** Verwey transition temperature as a function of the nonstoichiometry parameter δ (after Aragón, et. al., 1985).

Chapter 2) and Curie point (see section 5.2) obtained using magnetite thin films concurrently produced with these samples.

The amount of SIRM loss at the Verwey transition decreases with decreasing particle size. Powdered samples (Figure 5.8) also exhibit this trend although the amount of loss of SIRM intensity is in general more than those for samples of arrays of magnetite (Figure 5.6). Özdemir et. al., 1993, attributed this behaviour to surface oxidation. According to this explanation, surface oxidation results in the formation of a maghemite shell with a smaller lattice parameter than the magnetite core. The resulting stretching due to the differences in lattice parameters produce cracks on the surface creating ultrafine particles whose sizes are in the superparamagnetic range. It is the progressive unblocking of magnetisation with temperature by these ultrafine particles which suppresses the Verwey transition. The smaller the particle, the larger the surface to body ratio, and hence the more the Verwey transition suppression. Levi and Merrill, 1976, attributed the source of the observed smaller decrease in SIRM with grain size of magnetite samples to shape anisotropy. This is unlikely in the present case since the arrays of cubic shaped particles of this study have no significant shape anisotropy (their error in dimensions is less than 5%).

Although partial oxidation plays a role (e.g. see Figure 5.9), it is not convincing for samples whose Verwey plots are shown in Figure 5.6 which were placed in ethanol immediately after annealing and taken for Verwey transition measurements. XRD of co-annealed thin films of magnetite did not show any lines expected from oxidation. Moskowitz et. al., 1993 observed a similar difference between the loss of SIRM at the Verwey transition between inorganic magnetite powders and intact magnetotactic bacteria magnetite.

## 5.4 Possible explanation to the observed decrease in the SIRM lost at the Verwey transition

The magnetisation of a grain is sensitive to its atomic arrangement. Testimony to this is the existence of magnetocrystalline anisotropy. It is reasonable to expect the distortion of atomic arrangement at a particle's surface to play a role in its magnetic behaviour. At the boundary of grains, regular inter-atomic spacing is distorted (e.g. Mercer, 1990 pp. 50).

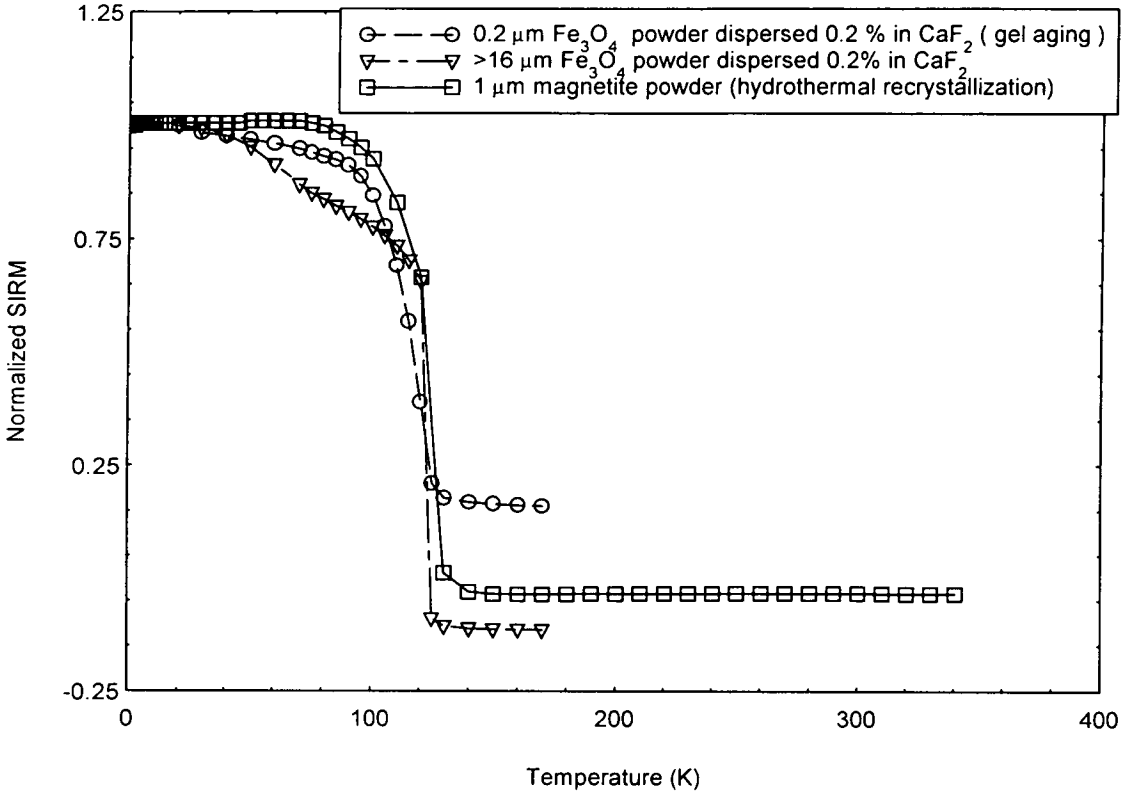


**Figure 5.8** Thermal demagnetisation of normalised SIRM for powdered samples whose particle sizes are 0.2 μm, 1 μm and greater than 16 μm, (i.e. sample Gel0.2, JH1 and JH>16 respectively), showing a decrease in the amount of SIRM lost at the Verwey transition with grain size.

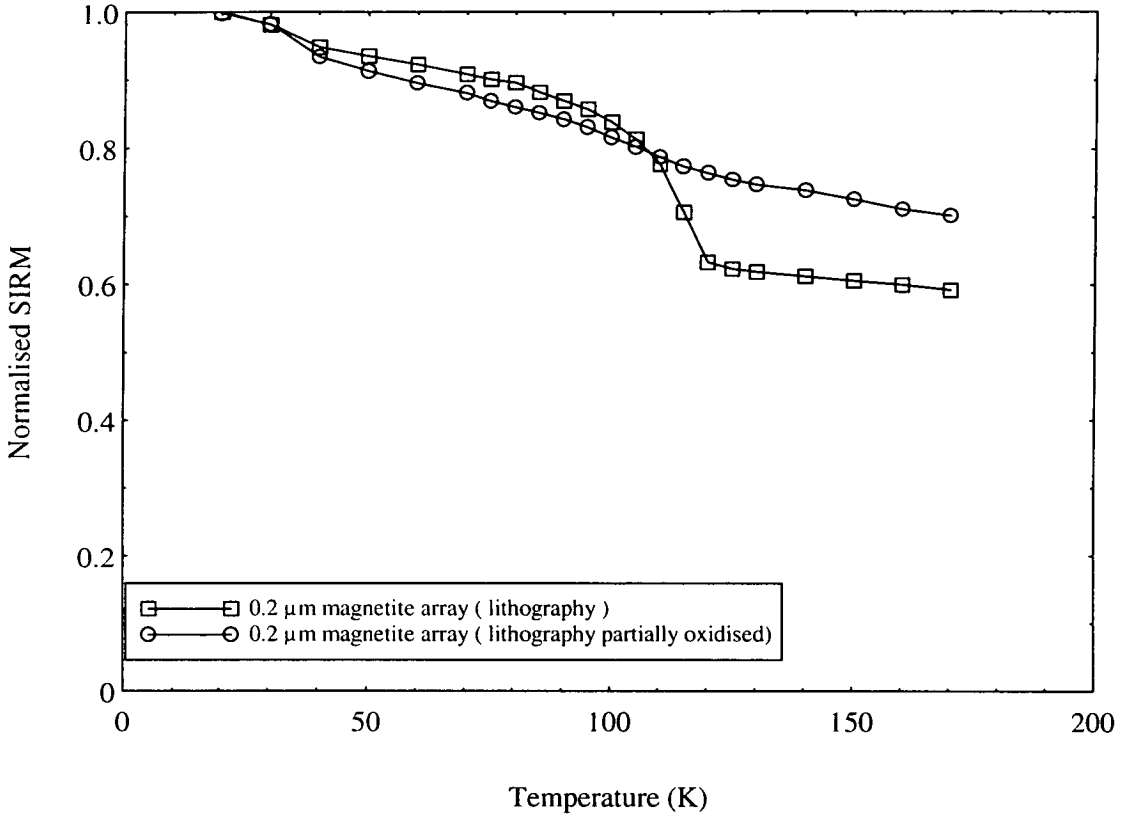


**Figure 5.9** The Verwey transition for partially oxidized samples of lithographically produced arrays of 0.2 μm (sample JK0.2) cubic magnetite particles compared to that of an unoxidised sample.

Since the surface area to body ratio of a particle increases with the decrease in particle size, this contribution could result in a similar trend to that exhibited by partially oxidised samples. Thus the observed decrease in SIRM intensity loss at the Verwey transition with particle size for unoxidised samples could be a surface to body ratio phenomenon which has nothing to do with oxidation of the sample.

An alternative explanation is to assume that the domain state of the particles in this size range is in a vortex state (Williams and Dunlop, 1989). Unlike single domain particles, these samples will not have all their atomic moments aligned in the (111) and (100) crystal directions at temperatures above and below the Verwey transition. Hence on cooling a sample through the Verwey transition, not all atomic moments will align themselves from the (111) to the nearest (100) crystal axis and hence less decrease in the SIRM is expected.

## 5.5 Effect of particle interaction on the Verwey transition

In order to determine the effects of magnetostatic inter-particle interaction, lithographically produced interacting magnetite particles (i.e. samples JK0.25@0.05, JK0.6@≈0.0 & JK1@0.25 were used. Figures 5.10, 5.11 & 5.12 show SEM pictures of these samples. A typical Verwey transition for interacting particles is shown in Figure 5.13. As can be seen from this figure, there is a larger drop in the SIRM lost at the Verwey transition for the sample with interacting particles than for that with non-interacting particles. Hence it is likely that the observed smaller drop in the SIRM at $T_V$ for arrays of magnetite particles of this study (Figure 5.6) or those of arrays of intact magnetotactic bacteria (Moskowitz et. al., 1993), than magnetite powder samples (e.g. this study Figure 5.8; Moskowitz et. al., 1993; Özdemir et. al., 1993) is due to particle clumping in the latter. The observed larger drop in SIRM at $T_V$ for a 0.5 μm thick magnetite film than an array of 0.5 μm non-interacting magnetite particles (Figure 5.6) is consistent with the deduction made above concerning particle clumping.

## 5.6 Effect of stress on the Verwey transition

Figure 5.14 shows SIRM as a function of temperature for an array of magnetite cubic particles after subjecting them to stress. Stress was induced

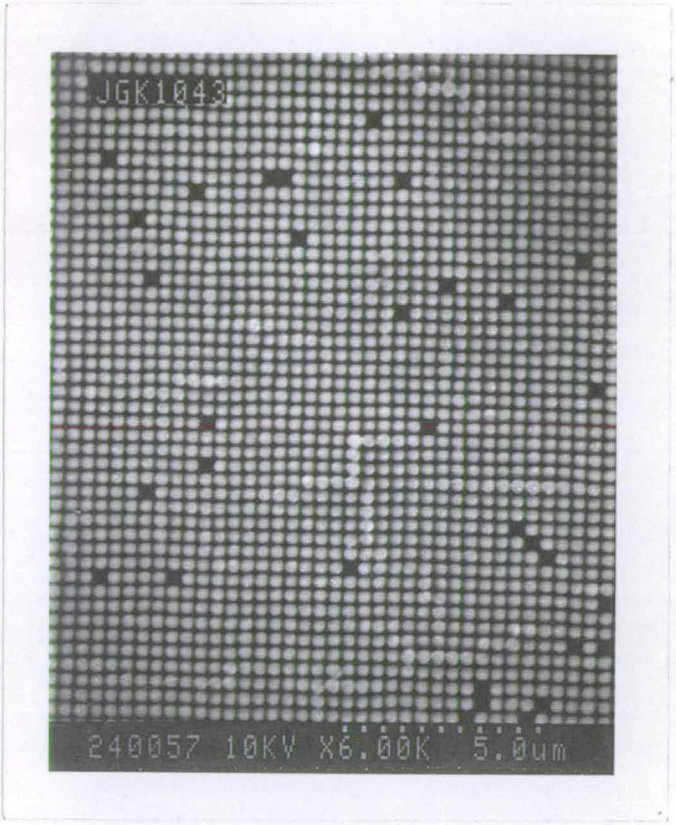


**Figure 5.10** SEM picture of lithographically produced interacting arrays of cubic magnetite particles. The cube edge for each particle is 0.25 μm while the inter-particle spacing is 0.05 μm. This is sample JK0.25@0.05.


**Figure 5.11** SEM picture of lithographically produced interacting arrays of cubic magnetite particles. The cube edge for each particle is 0.6 μm while the particles are just touching. This is sample JK0.6@≈0.0.

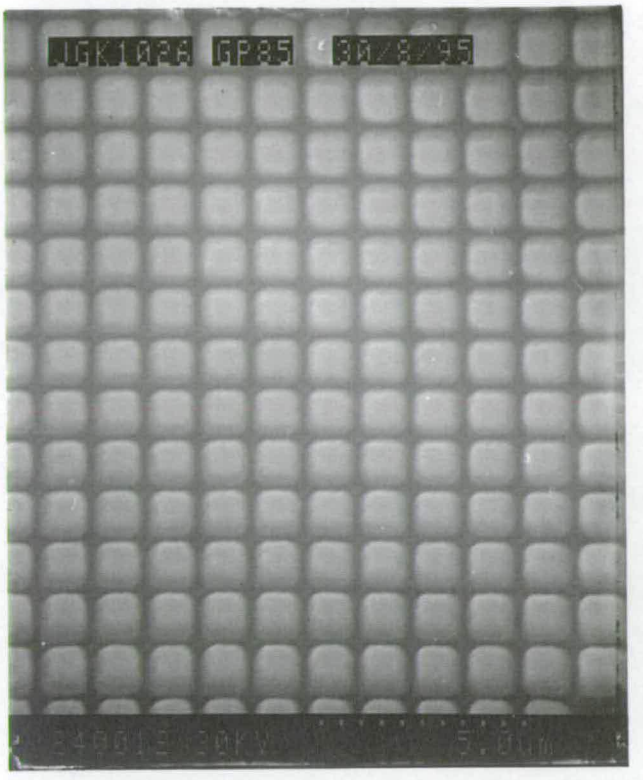

**Figure 5.12** SEM picture of lithographically produced interacting arrays of cubic magnetite particles. The cube edge for each particle is 1 μm while the interspacing is 0.25 μm. This is sample JK1@0.25.

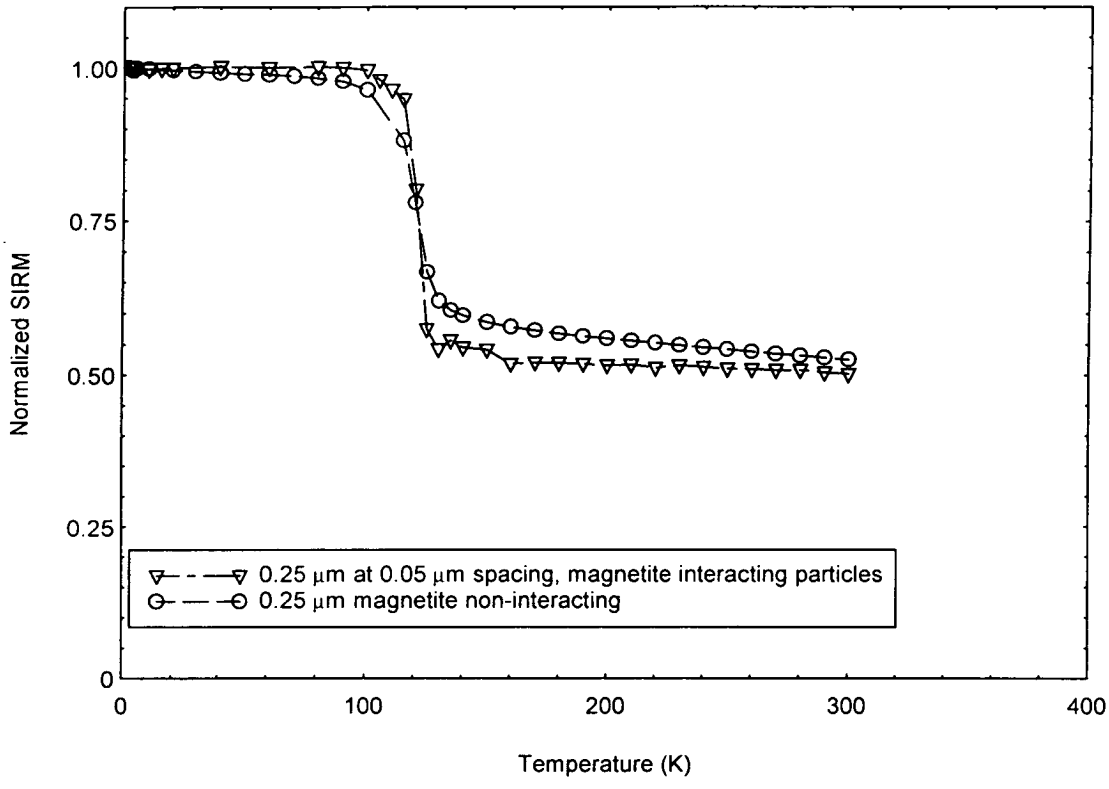


**Figure 5.13** Thermal demagnetisation of normalised SIRM given at 1.8 K in a field of 1 T for a sample of interacting lithographically produced arrays of 0.25 μm cubic magnetite particles (sample JK0.25@0.05) compared to that for a sample whose particles are non-interacting (sample JK0.25). The sample with interacting magnetite particles exhibits a larger drop in SIRM at the Verwey transition than that of non-interacting particles. Similar behaviour is displayed by magnetite powder sample.

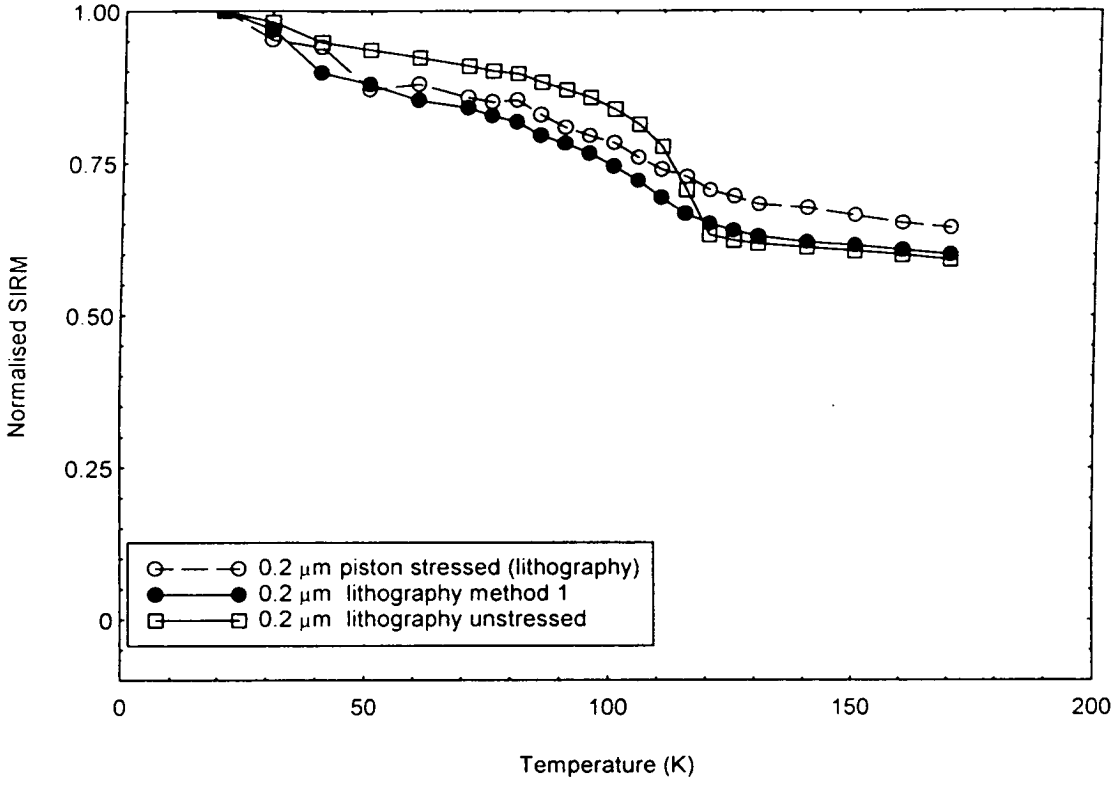


**Figure 5.14** Thermal demagnetisation of normalised SIRM given at 20 K in a 1 T field showing an increase in the temperature interval at which the Verwey transition occurs for the stressed lithographically produced 0.2 μm magnetite arrays particles (sample JK0.2) compared to that of the unstressed sample. The normalised SIRM for the sample obtained using method 1 is similar to that of the stressed sample.

in these samples by dropping the sample from 600° C into water placed below the furnace. According to Lowrie and Fuller, 1969, cooling magnetite at a higher rate of greater than 30° C/sec leads to structural defects. Hence the process of rapid quenching of samples described above insured that this rate was exceeded. Another way of subjecting the sample to stress was by applying physical pressure with a piston.

In Figure 5.14, curve marked with open circles shows SIRM intensity for a sample which was rapidly quenched by dropping from a temperature of 600° C into a water container at room temperature. There is a constant decrease in the amount of SIRM intensity starting from 70 K to 120 K temperature. The Verwey transition is still near 120 K. The curve marked with solid circles shows a typical example for an array of magnetite particles obtained using annealing method 1 which involved rapid cooling from 300° C to room temperature (see chapter 2). Although the Verwey transition is centred near 120 K, the rate of decrease is almost constant and occurs over a large temperature interval. This is most likely due to the difference in the stress anisotropy in a particle which is expected to increase from the top of a particle to the bottom (i.e. the particle-substrate interface). Thus different regions in a magnetite particle behave as if they each have their own magnetostriction anisotropy which is slightly different from the next region. This is to be expected if stress is mainly due to the differences in linear expansion coefficients between magnetite and the silicon substrate as suspected in this quenched samples.

From the above mentioned observations concerning stressed samples of magnetite, it can be concluded that stressed magnetite grains can lead to an increase in the temperature interval where the Verwey transition occur.

## 5.7 Effect of oxidation on the Verwey transition

Low temperature oxidation of magnetite often results in the formation of a layer of maghemite on the surface. Due to the difference in lattice constants between magnetite (3.96 Å) and maghemite (3.34 Å), stress as a result of lattice mismatch is expected in partially oxidised samples. It had already been shown in the above section that stress can lead to an increase in the temperature interval at which the Verwey transition occurs, hence one can expect partially oxidised particles to exhibit this behaviour. This has been found to be the case (Figure 5.9). There is no large decrease in SIRM

intensity below 40 K observed by Özdemir et. al. 1993, and ascribed to possible existence of small particles in the SPM size range. Such SPM particles are expected from the postulated cracking of a grain due to the lattice mismatch between the magnetite at the core and the maghemite at the surface. Using a high resolution SEM, no cracked grains were observed in the samples of this study.

## 5.8 The definition of magnetic memory

In this section it will be shown that two definitions of magnetic 'memory' exists in the literature. The definition of Haigh (1957) which is the same as that of Ozima et. al., 1964, Creer and Like, 1967, Kobayashi and Fuller, 1968, Nagata et al., 1964 and others not included in this list, is different from that of Heider et. al., 1992. The former definition will hereafter be referred to as **definition 1** while the later is **definition 2**.

### 5.8.1 Definition 1

According to this definition, memory refers to the recovery of the original direction of remanent magnetisation after cooling and warming through a low temperature transition in zero field. In this definition, there has to be a ***recovery*** of the remanence in the same direction as the original remanence. The amount of recovered memory is indicated by the letter A in Figure 5.15 (b). This definition will also be referred to in this study as the 'true' memory.

### 5.8.2 Definition 2

Here memory refers to the surviving remanent magnetisation after cooling and warming through a low temperature transition in zero field. In this definition, the lost remanence at the low temperature (if any) ***need not be recovered.*** Figure 5.15 shows such a memory indicated by the letter B.

For example, a sample which doesn't exhibit a low temperature transition such as maghemite will have 0 % and 100% memory according to definitions 1 and 2 respectively [Figure 5.15 (c)]. Since there has to be recovery of the lost remanence at the low temperature transition of magnetite according to definition 1, one has to measure the value of the remanence at

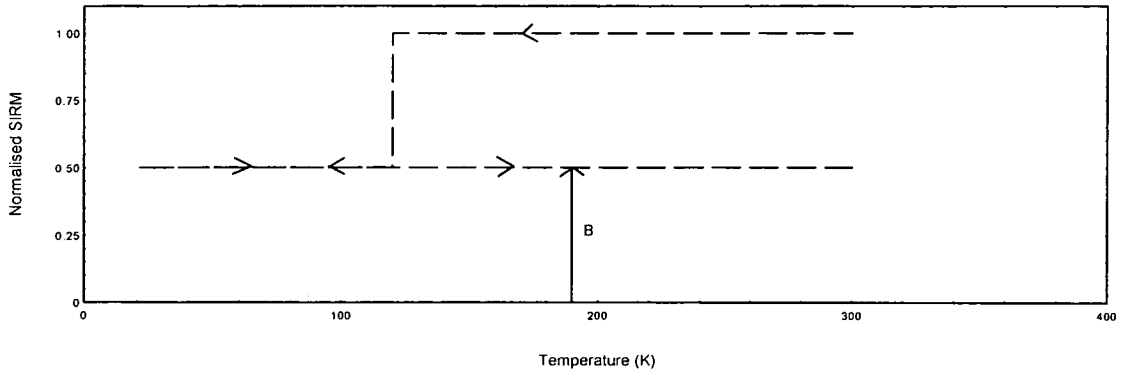


(a)

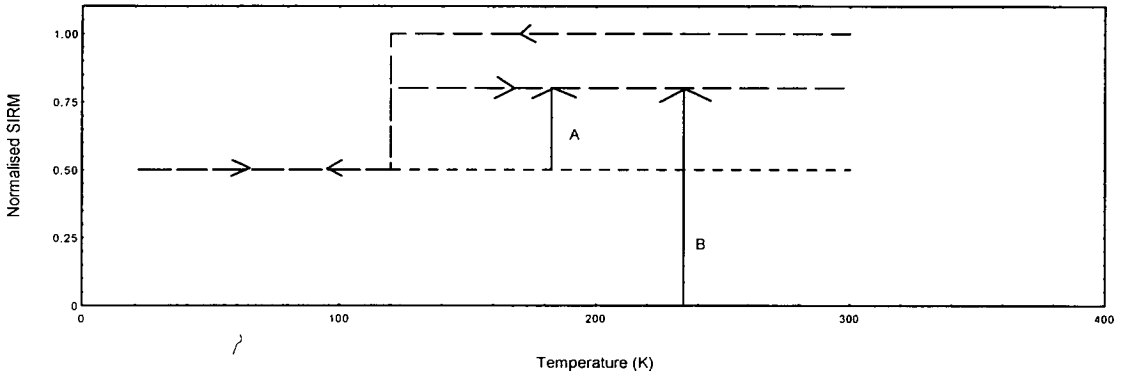


(b)

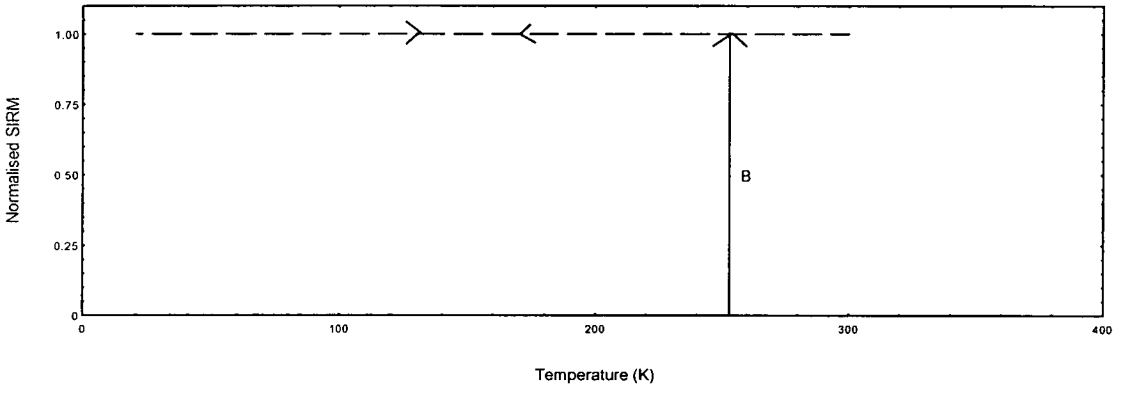


(c)

**Figure 5.15** Hypothetical normalised SIRM for magnetite showing (a) no memory according to definition 1, but memory equal to B according to definition 2. In (b) the magnetic memory according to definition 1 and 2 are given by A and B respectively. There is no low temperature transition in (c) yet the memory according to definition 2 is equal to B (a 100 % memory).

least once below the transition to confirm that there has been indeed a loss and recovery of remanence during the cooling and warming process. Thus a minimum of 3 points is required. On the other hand definition 2 allows one to measure only two points, i.e. one at room temperature and the other again at room temperature after cooling the sample through the Verwey transition temperature and warming it to room temperature. The practice of recording the SIRM before and after immersing a magnetite sample in a Dewar with liquid $N_2$, and allowing it to equilibrate before warming it back to room temperature in zero field as described by Dunlop and Argyle, 1991, measures the memory as defined by definition 2 even though these researchers defined memory according to **definition 1.**

## 5.9 MPMS2 set temperature overshooting problem and the measurement of magnetic memory.

In measuring the magnetic memory, one wishes to continuously measure SIRM from room temperature to below the Verwey transition and back to room temperature. However the MPMS2 program used (1995 version) does not allow continuous measurement of SIRM during cooling (or warming) from one set temperature to another. A measurement is only allowed after the next set temperature has been reached and is stable. The problem is the overshooting of the set temperature before it stabilises. For example, an overshoot of 30 K during cooling for a temperature set of 140 K when the MPMS2 **undercool mode is set to on** is typical. This subjects the sample to a temperature of 110 K before stabilising at 140 K and hence unpinning domains in a MD sample. If the undercool mode is off and the temperature interval between set points is 10 K or less, the temperature overshoot is about 1 K, provided the measurements are done at a temperatue lower than 200 K.

Another possible way of using the MPMS SQUID to measure memory is to record SIRM at 300 K, cool the sample to several tens of degrees below the Verwey transition (e.g. cooling to 20 K) before taking a measurement there. The sample is then warmed back to 300 K and SIRM recorded. This 3 point SIRM measuring procedure avoids the problem of overshooting past the Verwey transition described above. The problem with this process is that no information on the behaviour of SIRM in the vicinity of the Verwey transition is obtained.

In the present study the 3 point SIRM measuring procedure was done to quickly check the memory status of a sample. This was followed by measuring the magnetic memory at lower than 200 K at temperature intervals of 10 K or less.

## 5.10 Magnetic memory for unstressed samples

SIRM was given in a field of 1T at 300 K before cooling the sample in zero field to 20 K and then warming it back to 300 K. SIRM intensity was then given to the same sample in a field of 1T at 180 K and measured at 10 K temperature intervals on cooling to 20 K in zero field and back to 180 K. Figure 5.16 shows a plot of normalised SIRM for the thermal process described above for a lithographically produced sample of arrays of 1 μm magnetite particles (sample JK1) and as well that of magnetite powder of 1 μm particles (sample JH1). None of the samples exhibits magnetic memory according to definition 1 while according to definition 2 they all have memory.

## 5.11 Effect of stress on magnetic memory

Stress has long been suspected to be the source of the observed magnetite memory (e.g. Ozima, et al., 1964; Kobayashi and Fuller, 1968) although its effect was not specifically investigated for this mineral by these researchers. Kobayashi and Fuller, 1968, investigated the materials nickel and cobalt. Heider, at. el., 1992, investigated the effect of stress on magnetic memory of magnetite but since they did not measure any SIRM with low temperature during the cooling and warming process, no information was obtained on the nature of the SIRM recovery at the Verwey transition.

In the present study the effect of stress was investigated on lithographically produced arrays of cubic magnetite particles and magnetite powder. Stress was applied to both lithographically produced samples and gel aged magnetite powder by dropping them from the annealing temperature of $600^{o}$ C into water at room temperature.

It can be seen from Figure 5.17, that stressed samples exhibit memory according to definition 1 since there is a recovery of part of the SIRM loss at the Verwey transition. It should be noted here that any sample which has memory according to definition 1 is automatically having memory according to **definition 2**. It can be concluded from this observation of

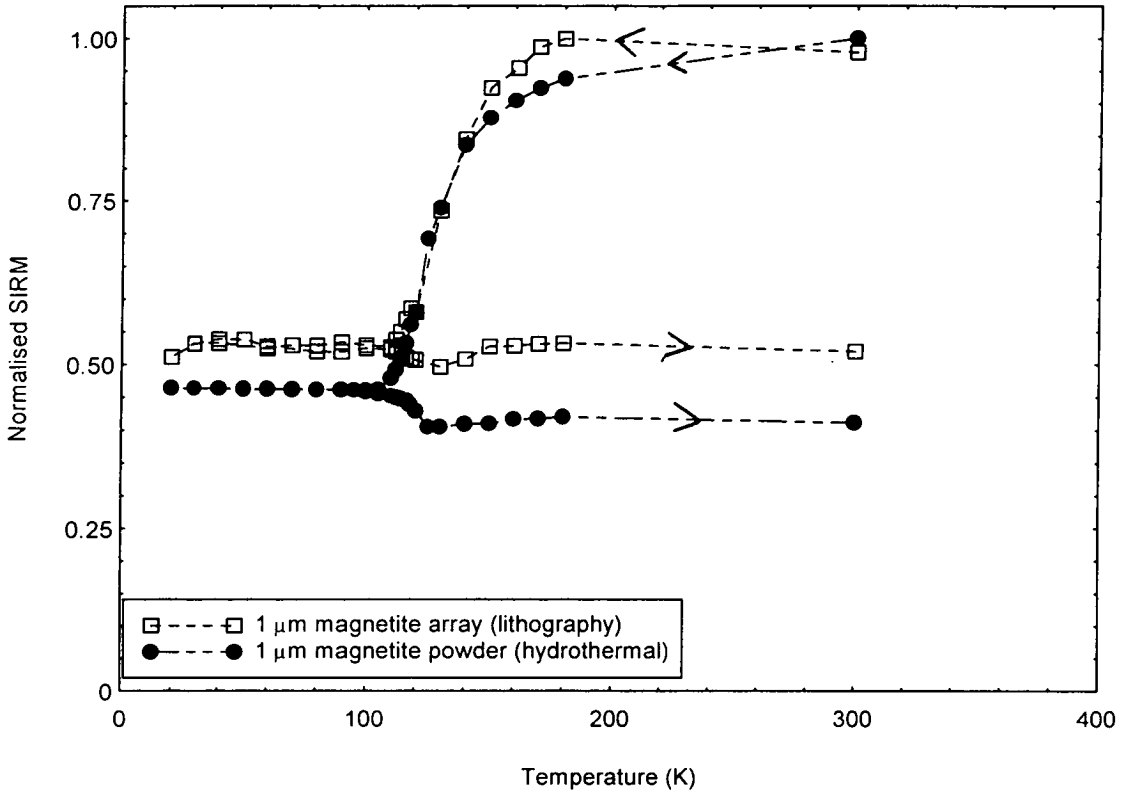


**Figure 5.16** Magnetic memory plots for 1 μm array of magnetite produced by the method of lithography (sample JK1), compared to a similar sized sample of magnetite powder produced by the hydrothermal recrystallisation method (i.e. sample JH1). There is no memory according to **definition 1**, but there is memory according to **definition 2** (see main text for explanation).

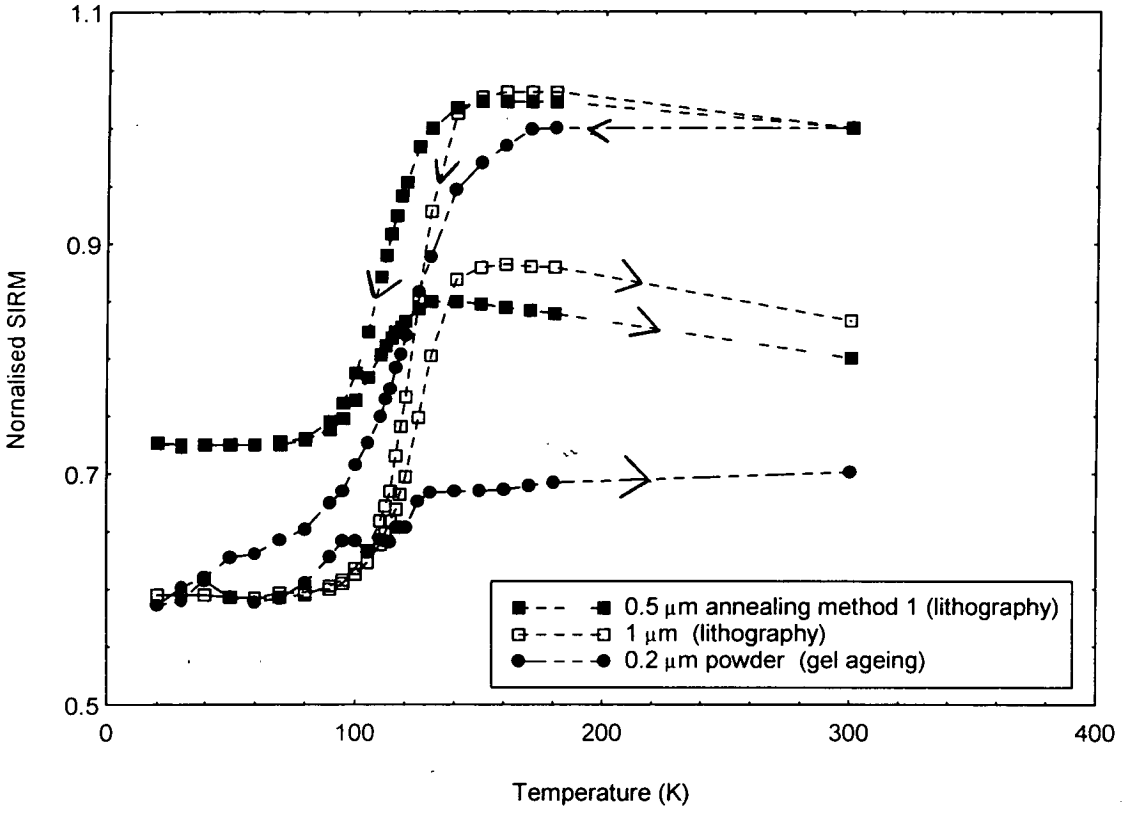


**Figure 5.17** Memory for rapidly quenched samples Gel0.2 (i.e. 0.2 μm powder produced by Gel ageing method and JK1 (a lithographically produced array of 1 μm cubic magnetite particles. Also shown is sample JK0.5 but annealed using method 1. All these samples exhibit 'true' magnetic memory (i.e. recovery of lost SIRM at the Verwey transition).

memory for stressed samples that indeed memory according to definition 1 is a result of stress. What is measured as memory according to definition 2 could contain both memory as defined by definition 1 and the size dependence of SIRM lost at the Verwey transition discussed in the section 5.4 above or just the latter.

The magnetic properties of a 2 mm natural crystal (sample JSC1) from Shetland greenschist which was kindly provided by Mr Peder Aspen (University of Edinburgh, Department of Geology and Geophysics) were measured. The Curie temperature of this sample was found to be 550$^{o}$ C. Its Verwey transition temperature was 107 K. The lower than 120 K observed low temperature transition for this sample is most likely an indication of non-stoichiometry. The magnetic memory of this sample was found to be very high (Figure 5.18). It can be concluded that this magnetite crystal is stressed. Stress may have been induced during its formation or during the extraction or during the process of Curie point determination by heating and cooling.

## 5.12 Saturation magnetisation as a function of low temperature

According to theoretical predictions (e.g. O'Reilly, 1984), the saturation magnetisation of magnetite should decrease with increasing temperature till the Curie point without any transition in between. However, as can be seen from Figure 5.19, an increase in saturation magnetisation is observed near 120 K on warming the sample from 5 K. The applied saturating field was 1T.

This observation is not entirely explicable in terms of the Verwey model of a 'structural-electronic' transition which explain some observed transition parameters in terms of electron hopping between the iron cations in the B site of the magnetite crystal structure (O'Reilly, 1984). A possible model which can explain the observed increase in saturation magnetisation ($M_S$) near 120 K is the so-called 'magnetic-electronic' model (Belov, 1993). According to this model, some conducting electrons are trapped by the field of the iron cations in the B site. Such trapped electrons have their magnetic moment in a direction which is antiparallel to that of cations in the B sites hence the reduction of magnetisation. It is not the intention of the present study to vindicate this theory, hence the interested reader is referred to the review article by Belov (1993).

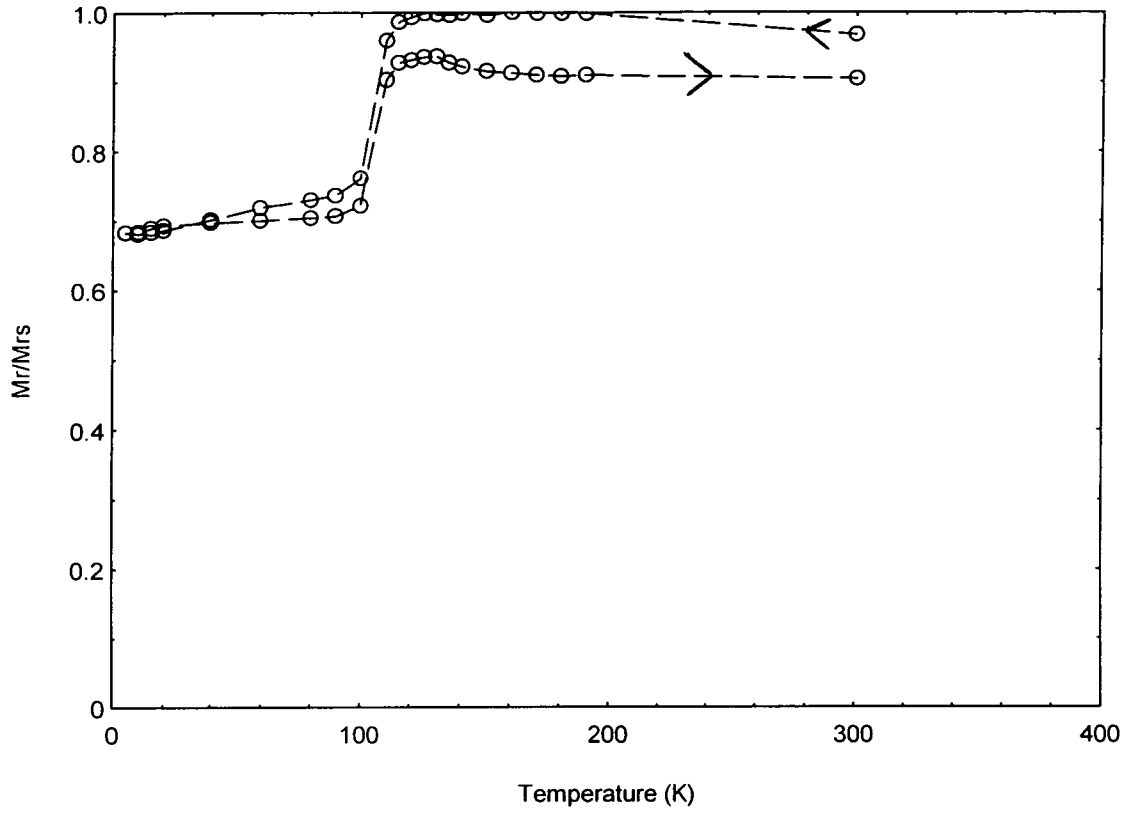


**Figure 5.18** Saturation remanence measured in zero field as a function of temperature for a 2 mm size single crystal of magnetite (i.e. sample JSC1). The sample exhibits a very high memory - a sign of stress.

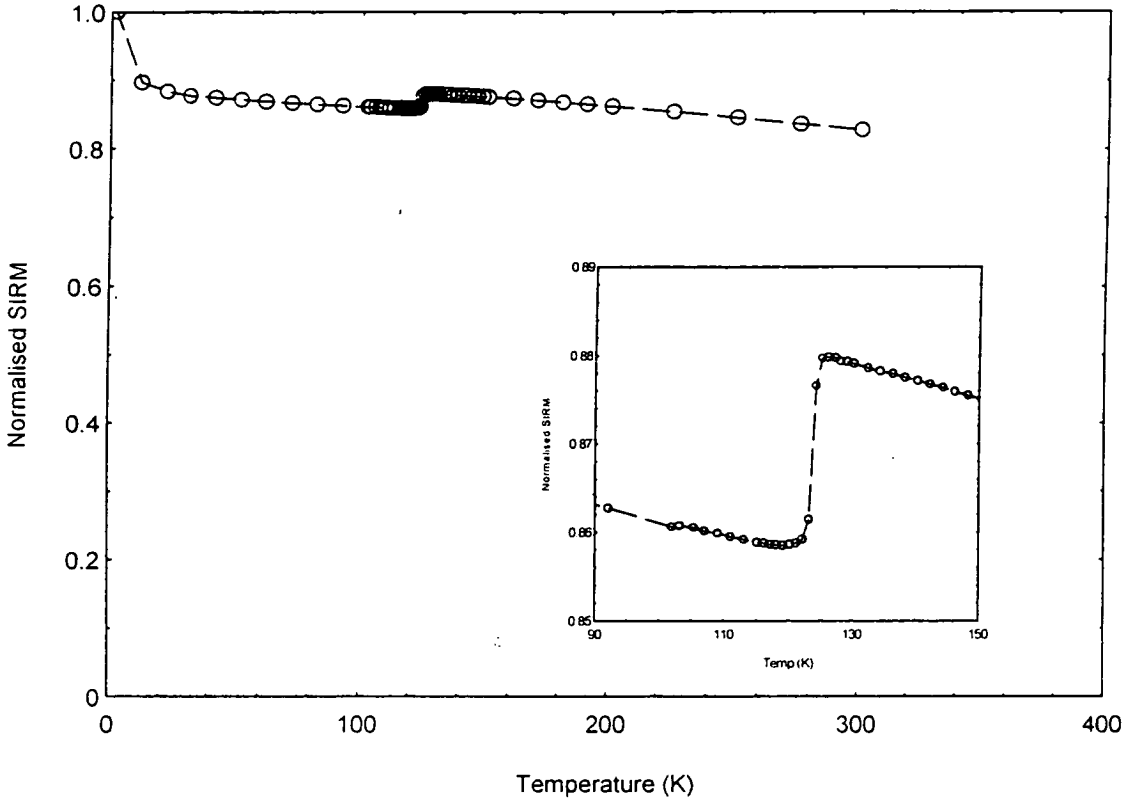


**Figure 5.19** Normalised magnetisation obtained in a field of 1 T when a sample of magnetite was warmed from 5 K to 300 K. An increase in magnetisation can be seen near 120 K. The transition is easily visible from the inset figure.

However, the intention here is to draw attention to a possible high field low temperature method of identifying magnetite by measuring the $M_S$ as a function of low temperature and observing if there is an increase near 120 K. Such a measurement would not require the sample to be in an essentially field free environment which is necessary when observing SIRM changes (e.g. section 5.3).

## 5.13 Coercivity as a function of low temperature

An attempt was made to measure hysteresis loops of lithographically produced particles as a function of low temperature using the MPMS2 SQUID. However this equipment was found to be not suitable for producing loops with clearly resolvable coercivities for most of lithographically produced arrays of magnetite samples because of their weak total moment. Here the coercivity ($H_C$) as a function of temperature for a lithographically produced sample of an array of 1 μm cubic particles of magnetite (sample JK1) and two samples of magnetite powders (JH0.5 and JK>16) is reported. The sample JK1 had a large enough total moment for the coercivity to be resolved by the MPMS2 SQUID.

Figure 5.20 shows coercivities plotted as a function of temperature for these samples. The curves for samples JK1 and JH0.5 shows a gradual increase in coercivity with decreasing temperature before a comparatively sharp decrease to a minimum around the Verwey transition temperature. The temperature then increases drastically with decreasing temperature before reaching a maximum and then gradually decrease again. On the other hand the curve for $H_C$ as a function of temperature for JK>16 μm show no such increase and decrease with temperature above the Verwey transition.

From the above observations, it seems reasonable to deduce that the existence of a small maximum in the observed coercivity as a function of low temperature above the Verwey transition could be typical of PSD particles. Upon checking available data in the literature (e.g. Hodych, 1986, 1990, Schmidbauer & Schembera, 1987 and Morrish & Watt, 1958), the same difference as outlined above was observed.

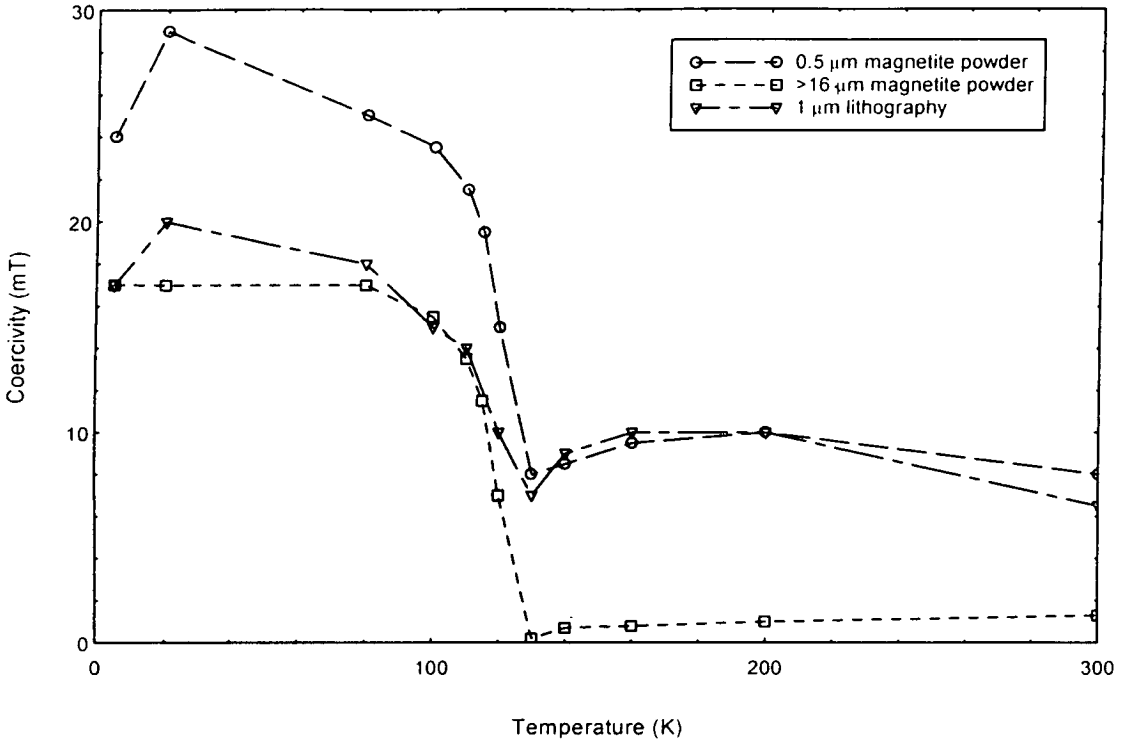


**Figure 5.20** Coercivity as a function of temperature showing a slight increase followed by a decrease in coercivity on either side of 120 K for samples JH0.5 and JK1 but not for the JH>16.

## 5.14 Summary

Using samples of arrays of magnetite particles of well defined dimensions including particle inter-spacing, the following results were obtained. The larger drop in SIRM at the Verwey transition observed in this study and other studies (e.g. Moskowitz et. al., 1993), compared to samples of magnetite powders was shown to be consistent with effects of inter-particle magnetostatic interactions in the latter. The particle-size dependence of the drop in SIRM at the Verwey transition displayed by magnetite particles in the PSD range has been shown to be explicable in terms of the vortex domain structures obtained from 3-D micromagnetic calculations (e.g. Williams and Dunlop, 1989). The reported particle-size dependent memory by other researchers (e.g. Dunlop and Argyle, 1991; Heider et. al., 1992), is most likely a reflection of the amount of the SIRM lost at the Verwey transition instead of being the 'true' magnetic memory. Magnetic memory has been shown to be a stress related phenomenon. This observation might be useful in accessing the nature of stress in rocks. A possible method of identifying rocks containing magnetite by measuring saturation magnetisation as a function of low temperature has been identified. Such a method does not require the sample to be in an essentially field free space as is necessary when SIRM is measured.

# Chapter 6 Room temperature magnetic properties of cubic arrays of magnetite particles

## 6.1 Introduction

Unless otherwise stated, the magnetic properties reported in this chapter were measured using an AGFM at the University of North Wales (Bangor) and the applied field was in the plane of the substrate. Room temperature magnetic properties such as hysteresis loop parameters are often used to determine the type of grains responsible for the natural remanent magnetisation in rocks. The stability of NRM over geological time depends on the type of magnetic grains which carry this remanence. As pointed out in chapter 1, the magnetic properties of grains whose sizes are in the PSD range are poorly understood. In this chapter hysteresis loops for magnetite thin films are plotted to demonstrate that the sample's magnetisation reaches saturation readily unlike those of directly deposited magnetite thin films at high substrate temperatures (e.g. Margulies et al., 1996). The hysteresis loops and their associated parameters such as coercivity and isothermal remanence are plotted as a function of particle size and spacing for interacting and non-interacting cubic magnetite particles in the size range 0.1 - 1 μm. Also plotted and discussed are the acquisition and DC demagnetisation curves for these samples. These curves are often used to study the effects of magnetisation interactions in rock magnetism. The values of the magnetic parameters of samples used in this study are given in Table 6.1.

Magnetic properties of lithographically produced arrays of magnetite are compared to results of theoretical predictions and as well selected representative experimental data from the literature. It is shown that none of the samples exhibits magnetic properties consistent with the mechanism of coherent rotation or 'truly' multidomain, but in general is in good agreement with the mechanism of reversal by vortex nucleation and propagation predicted from 3-D micromagnetic calculations (e.g. Enkin and Williams, 1994).

| Sample name | Particle dimension (μm) | Coercivity $H_c$ (mT) | Normalised saturation remanence ($M_{rs}/M_s$) | Crossover point | Remanence coercivity ($H_{cr}$) |
|---|---|---|---|---|---|
| JK0.1 | cube edge 0.1 | 18 | 0.4 | 0.3 | 21.5 |
| JK0.2 | " " 0.2 | 14 | 0.21 | 0.36 | 25.2 |
| JK0.3 | " " 0.3 | 9.5 | 0.17 | 0.36 | 29.2 |
| JK0.5 | " " 0.5 | 8 | 0.19 | 0.25 | 14.5 |
| JK1 | " " 1 | 6.5 | 0.1 | 0.26 | 14.2 |
| JK0.25@0.05 | 0.25 at spacing of 0.05 | 9.2 | 0.14 | 0.35 | 22 |
| JK0.6@≈0.0 | 0.6 at spacing of almost zero | 7.8 | 0.15 | 0.42 | 22 |
| JK1@0.25 | 1 at spacing of 0.25 | 5.6 | 0.25 | 0.56 | 32 |
| " field ⊥ | | 5 | 0.12 | 0.33 | 12 |

**Table 6.1** Table showing the values of magnetic parameters for samples used in this chapter. The values shown are for the case when the field was applied parallel to the major axis except for sample JK1@0.25 row at bottom of the table whose first column has a symbol ⊥ where the field was perpendicular to the major axis.

## 6.2 Hysteresis loops for magnetite thin films

The hysteresis loops shown in Figure 6.1 (a) are for magnetite thin films of thicknesses 0.5 μm (circle markers) and 1.5 μm (square markers). The middle curve (triangle markers), obtained by subtracting the diamagnetic contribution of the silicon substrate from the measured values of the loop for the 0.5 μm thick magnetite thin film (circle markers) is practically the same as the latter curve. Normalised magnetisation plots of the samples shown in Figure 6.1 (a) are plotted in Figure 6.1 (b). The samples were first demagnetised before the magnetisation was measured as the field was increased from zero to 1 000 mT.

It is evident from Figure 6.1 that the magnetite films readily saturate in fields of less than 500 mT. This behaviour which is typical of pure unstressed magnetite particles, is in contrast to that of magnetite thin films of Margulies et al., 1996, which did not saturate in fields as high as 7 000 mT.

## 6.3 Hysteresis loops for arrays of cubic magnetite samples

Figure 6.2 show examples of measured hysteresis loops for samples of non-interacting arrays of cubic magnetite particles. There is a general narrowing of the loop width as the size of the particles in a sample increases from 0.1 μm to 1 μm. Although each curve is shown up to a maximum field of 500 millitesla (mT), most of the curves were measured by applying a field of up to 1 T. The higher than 500 mT part of each curve is not shown since it is not different from that shown in the vicinity of 500 mT. The samples have practically reached their saturation point at this field. Plotting the loops to a maximum applied field of 500 mT instead of 1 T also improves the clarity of the loop width when all the loops are plotted in a single graph as done in Figure 6.2. The saturation magnetisation ($M_S$) estimated from the total volume assuming a density of 5200 kg/m$^3$ for magnetite was in the range 87 - 93 Am$^2$/kg. Hence the measured $M_S$ is in good agreement with the literature value of 92 Am$^2$/kg (Thompson & Oldfield 1986). In general there was no significant change in the shape of the loops with the direction of the applied field for non-interacting particles.

In order to check the effects of inter-particle interaction on the hysteresis loops, lithographically produced interacting cubic magnetite particles (samples JK0.25@0.05, JK0.6@≈0.0 & JK1@0.25), were used.

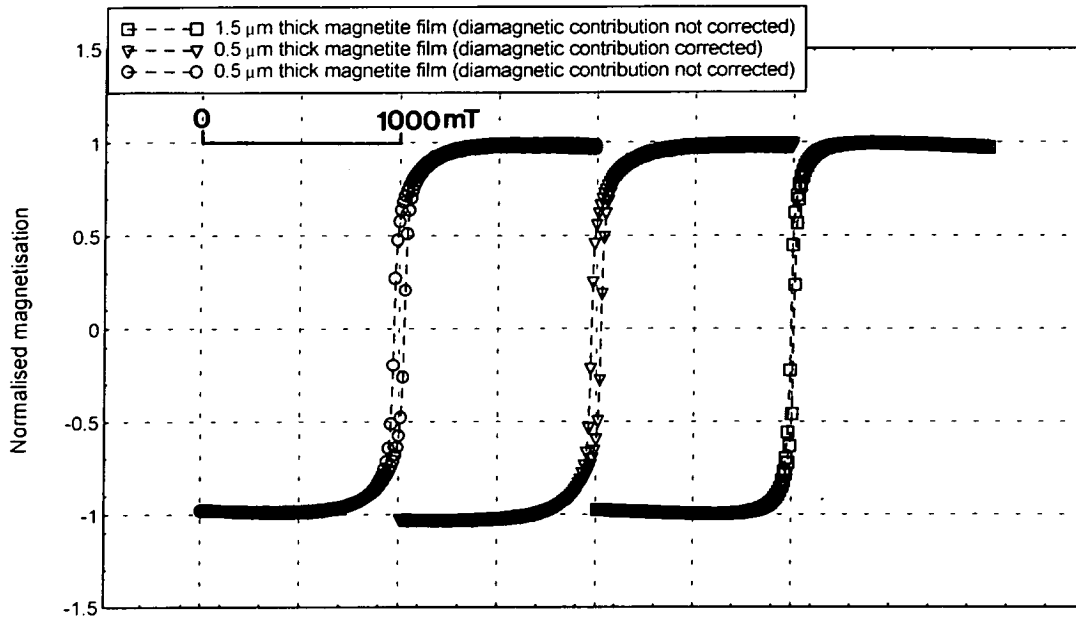


(a)

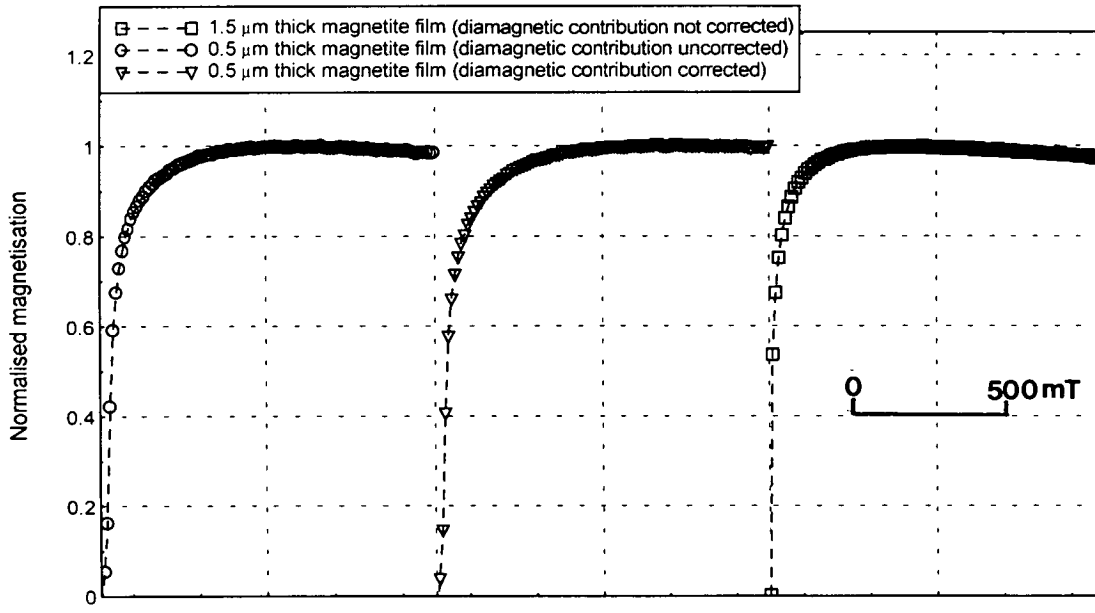


(b)

**Figure 6.1** (a) Hysteresis loops for samples of 0.5 μm and 1.5 μm thick magnetite films and (b) magnetisation measured as a function of applied field starting from a demagnetised state for the same samples. It is clear from these plots that the magnetite thin films of this study readily saturate in fields of less than 500 mT. The field was applied in the plane of the film.

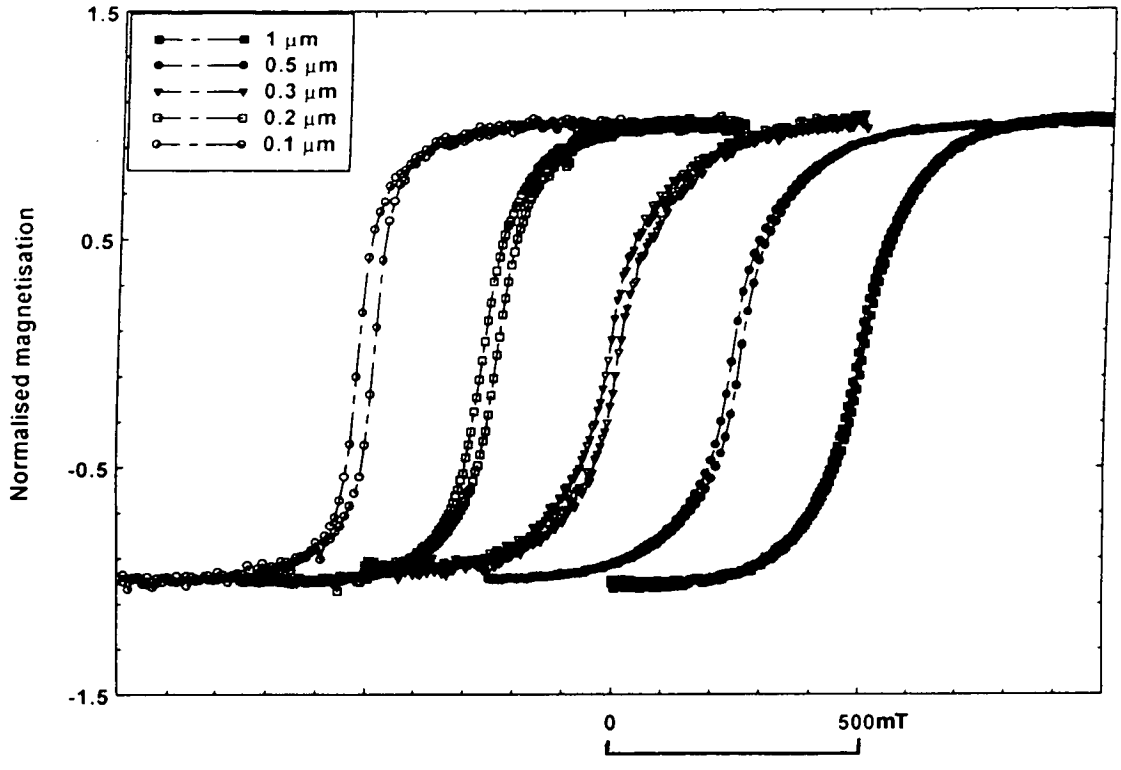


**Figure 6.2** Hysteresis loops for samples of arrays of non-interacting cubic magnetite particles of sizes 0.1 μm, 0.2 μm, 0.3 μm, 0.5 μm and 1 μm (i.e. samples JK0.1, JK0.2, JK0.3, JK0.5 and JK1 respectively). The loops become narrower with increasing grain size,

The Figure 6.3 shows the hysteresis loops for sample JK1@0.25. The hysteresis loops for samples JK0.25@0.05 and JK0.6@≈0.0 are not shown since there are almost similar to those for the JK0.3 and JK0.5 non-interacting particles shown in Figure 6.2 respectively. It can be seen from Figure 6.3 that the loop for sample JK1@0.25 is not only different from that of the non-interacting sample JK1, but also different from that obtained when the field was applied in the plane perpendicular to the substrate for the same sample. The loop obtained with the field in the plane of the substrate show saturation attained at lower fields than when the field is in the out of substrate plane.

Although visual inspection of hysteresis loops can provide useful qualitative information on the nature of the behaviour of the magnetic particles, it is the comparison of the loop parameters such as coercivities and remanence which provide quantitative information. In the next section the coercivities of both interacting and non-interacting particles are compared to published theoretical predictions and experimental results of other researchers.

## 6.4 Coercivities as a function of grain size

According to Stoner and Wohlfarth (1948) single domain theory, a grain which is too small to contain a domain wall will have all its atomic moments aligned in one direction. During the magnetic reversal of such a particle the rotation of the moments will still maintain this configuration. In this case the coercivity of oriented particles without any shape anisotropy but with magnetocrystalline anisotropy is given by

$$H_C = 2K_1/M_S \qquad (6.1)$$

while that for randomly oriented particles is given by

$$H_C = 0.64K_1/M_S \qquad (6.2)$$

where K and $M_S$ are the magnitude of the crystalline anisotropy constant and saturation magnetisation for magnetite at room temperature respectively.

The Figure 6.4 shows a bi-log plot of coercivities as a function of particle size for interacting and non-interacting arrays compared to the

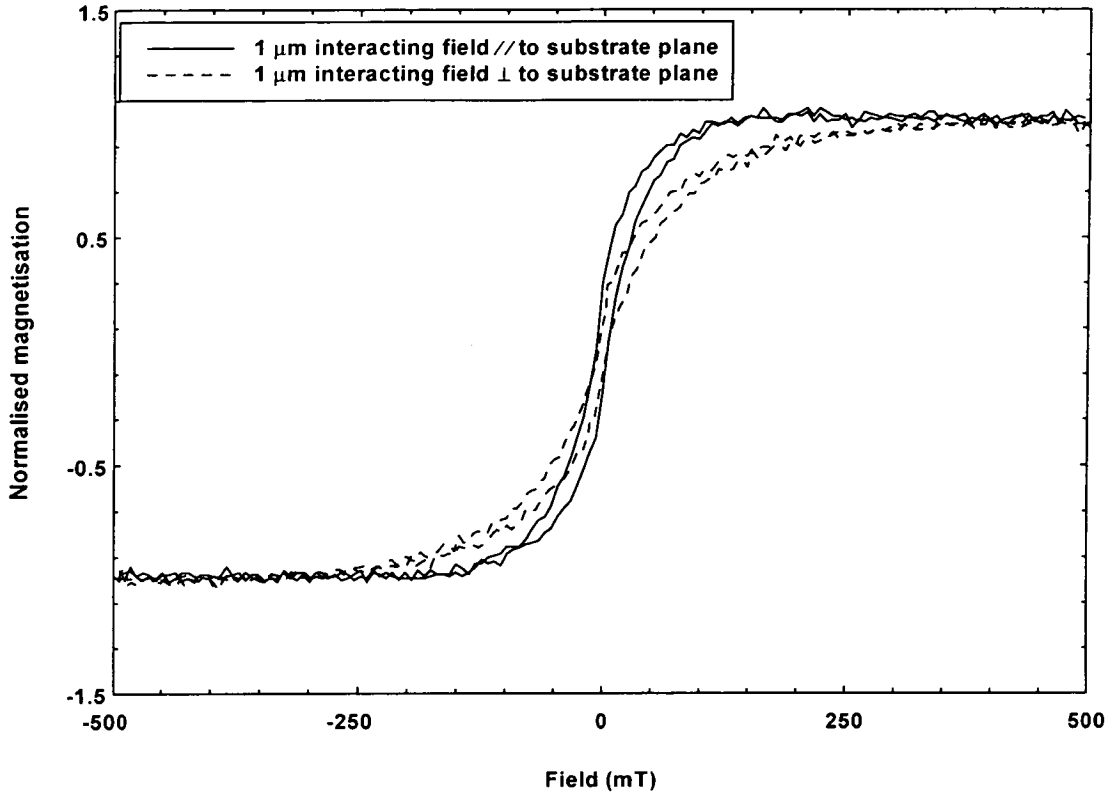


**Figure 6.3** Hysteresis loops for sample of interacting cubic magnetite particles of 1 μm size and spacing of 0.25 μm (i.e. sample JK1@0.25).

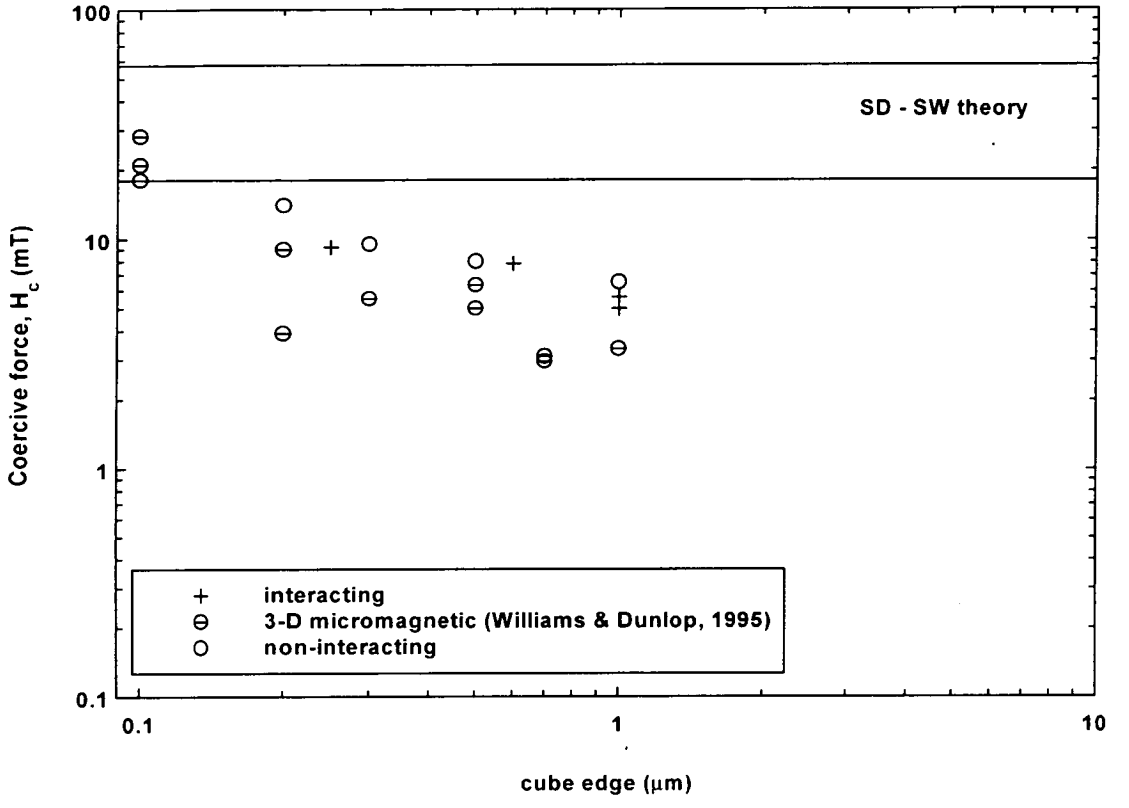


**Figure 6.4** Coercivity as a function of particle size for non-interacting (samples JK0.1, JK0.2, JK0.3, JK0.5 & JK1 and as well interacting arrays of magnetite particles (samples JK0.25@0.05, JK0.6@≈0.0 & JK1@0.25), compared to that of single-domains (SD) whose dominant anisotropy is crystalline anisotropy. The Stoner & Wohlfath SD theory was used to calculate the value for the solid line shown. Also shown in this figure are the coercivities obtained from 3-D micromagnetic calculations of Williams and Dunlop, 1995.

minimum and maximum values predicted from the Stoner and Wohlfarth, 1948 theory. Also shown are the results from 3-D micromagnetic calculations of Williams and Dunlop, 1995. It can be seen from this figure that (with the exception of sample JK0.1), none of the lithographically produced samples has a coercivity in the range expected from the SW theory. It is concluded from this that most of the particles are not single domain. This conclusion is consistent with the results of 3-D micromagnetic calculations.

In general, the coercivities of lithographically produced samples are slightly higher than those obtained from 3-D micromagnetic calculations (Williams and Dunlop, 1995). The small difference could be due to the assumption made in micromagnetic calculations that the atomic arrangement of a grain (including their inter-spacing) is uniform throughout the whole sample. The atomic arrangement of real grains departs from this idealised situation.

The coercivities of interacting particles JK0.25@0.05, JK0.6@≈0.0 and JK1@0.25 are also shown in Figure 6.4. The coercivities of interacting particles differ only slightly from those of non-interacting particles of similar size. It can be concluded that particle interaction does affect magnetic properties of PSD cubic magnetite particles.

Figure 6.5 shows the coercivities of lithographically produced particles compared to selected representative data for crushed and grown crystals from the literature. Also shown in the same figure are coercivities for lithographically produced magnetite particles obtained using annealing method 1 which involved rapid quenching of samples from a high temperature to room temperature (see chapter 2). The coercivities of lithographically produced samples are slightly higher than those of laboratory grown magnetite powder samples. This small difference is probably due to inter-particle magnetostatic effects in the magnetite powder samples.

However, in general, the coercivity plot for samples obtained using method 2 are in agreement with literature data for laboratory grown magnetite particles while those obtained using annealing method 1 are in good agreement with literature data for crushed samples. Unlike crushed samples, laboratory grown magnetite particles have very low internal stresses (Heider et al., 1987).

Since non-interacting lithographically produced arrays of cubic magnetite particles are of uniform size, it can be concluded that the

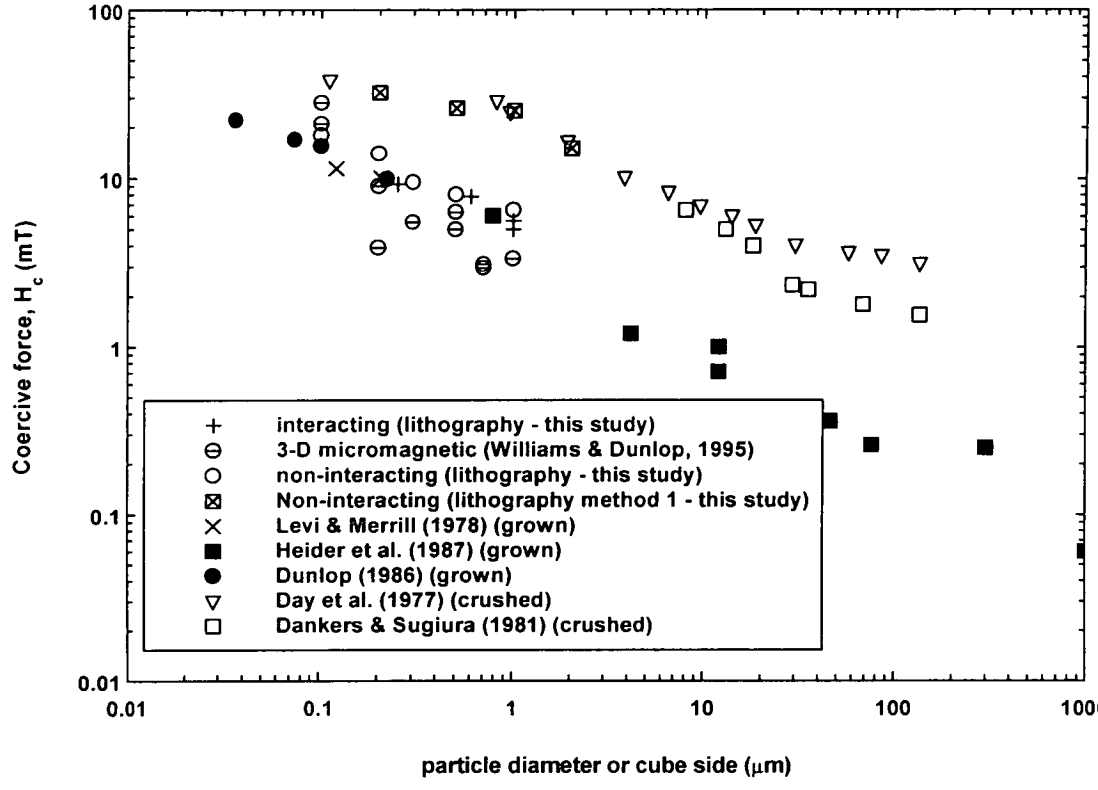


**Figure 6.5** Coercivity as a function of particle size for lithographically produced arrays of cubic magnetite particles of this study compared to representative experimental and theoretical data. Data for magnetite samples obtained using annealing method 1 and 2 fall in the trend for stressed and unstressed literature data respectively.

coercivities of the samples annealed using method 2 are the true representative of PSD samples which are magnetocrystalline anisotropy controlled. Hence there is no sharp drop in coercivity at the supposed single domain to 2 domain transition boundary predicted from hypothetical magnetic domain predictions of the type described in chapter 1 section 1.4. However, the magnetic properties of arrays of magnetite particles of this chapter are in good agreement with data from 3-D micromagnetic calculations in general.

## 6.5 Normalised saturation isothermal remanence ($M_{RS}/M_S$) for cubic arrays of magnetite as a function of grain size

According to the SW theory, oriented single domain particles with uniaxial anisotropy should have a normalised saturation remanence value of 1 while that for the random case is 0.5. For a magnetite sample whose particles are cubic and randomly oriented, the normalised remanence should be 0.87, (O'Reilly, 1984, pp. 73). Figure 6.6 shows normalised saturation remanence as a function of size for arrays of cubic magnetite particles compared to theoretical prediction for the SW theory and 3-D micromagnetic calculated values (Williams and Dunlop, 1995). The largest measured remanence for lithographically produced samples of this study is 0.43 (sample JK0.1). This value is however, far smaller than 0.87 expected from the SW theory. It can be concluded that the 0.1 μm sample contains particles which are not single domain.

In general the measured normalised saturation remanence of lithographically produced samples are higher than those of 3-D micromagnetic calculations (Figure 6.6). Again slight differences are observed between theory and reality, such as the possible difference in the surface structure.

The normalised saturation remanence for interacting cubic particles is also shown in Figure 6.6. Again a change in the remanence due to particles interaction is evident.

In Figure 6.7, normalised saturation remanence obtained for samples in this study is compared to selected representative data from the literature. In general saturation remanence for lithographically produced samples are slightly higher than those obtained by other researchers using laboratory

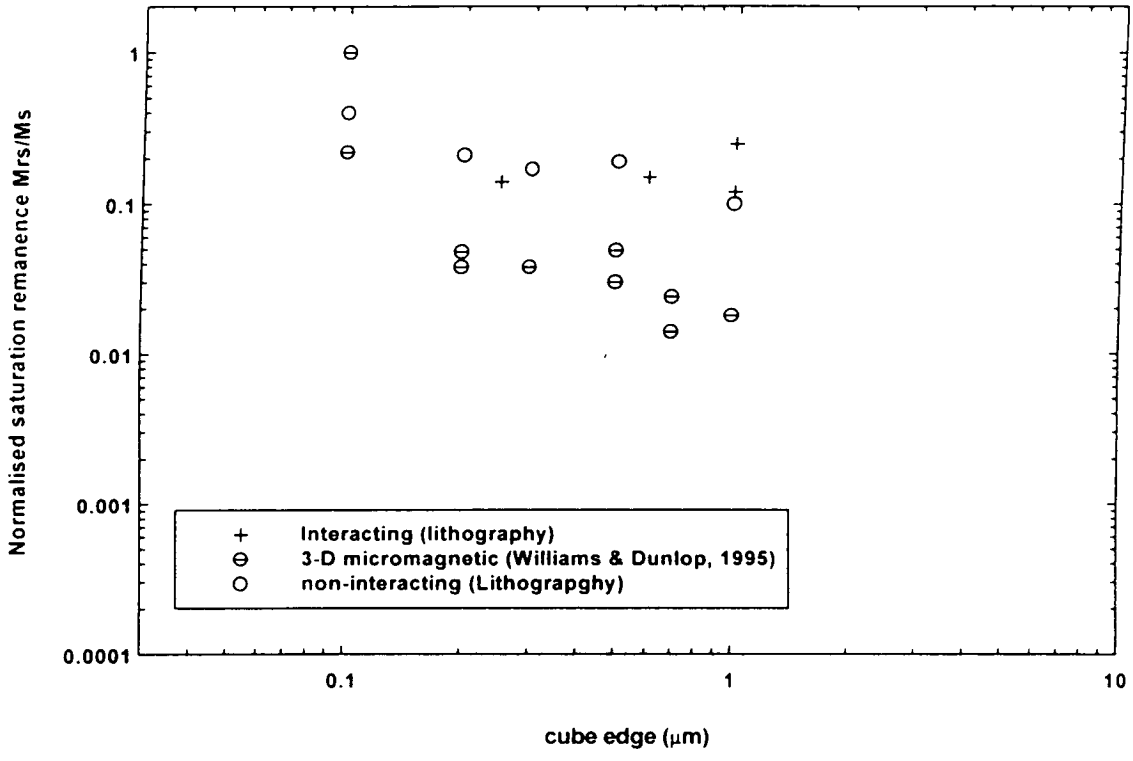


**Figure 6.6** Normalised saturation remanence curves as a function of cube edge for lithographically produced arrays of interacting and non-interacting particles whose coercivities was shown in Figure 6.4, compared to 3-D micromagnetically calculated values of Williams and Dunlop, 1995.

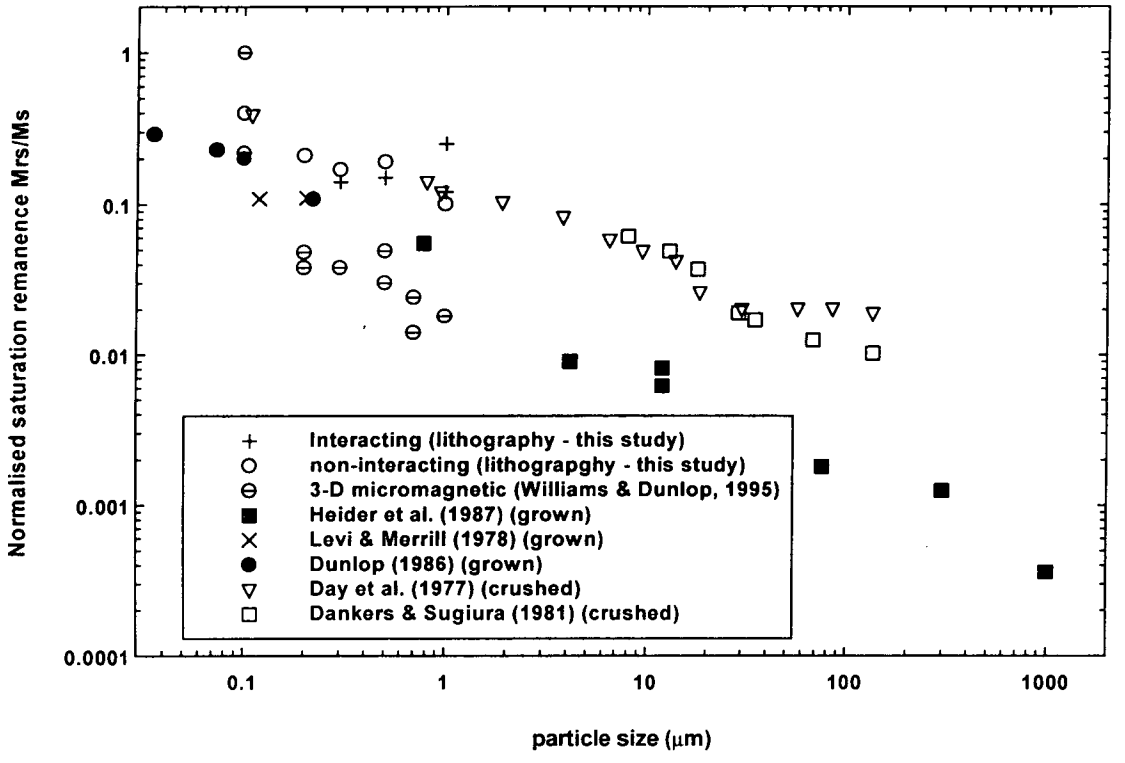


**Figure 6.7** Normalised saturation remanence curves as a function of particle size for lithographically produced arrays of interacting and non-interacting particles compared to results of other reseachers.

grown magnetite powders. The differences is probably due to inter-particle interactions effects in the latter.

## 6.6 Comparison of acquisition and demagnetisation of isothermal remanence curves for arrays of cubic magnetite particles

According to Wohlfarth (1958), in the absence of inter-particle interactions, the isothermal remanence magnetisation [$M_r(H)$] is related to the demagnetisation remanence [$M_d(H)$] by

$$M_d(H) = 1 - 2M_r(H) \qquad (6.3)$$

This relation was first plotted by Henkel (1964) who deduced that any deviation from the plot for SD particles should be a result of inter-particle magnetostatic interactions. In rock magnetism the normalised curves $M_d(H)$ and $M_r(H)$ are often plotted in the same graph as a function of field (H) and if the point where the curves cross has a value of less than 0.5 for SD particles, the sample is considered to have interacting particles.

An AGFM was used to measure $M_d(H)$ and $M_r(H)$ curves as a function of applied field. A sample was first af demagnetised using separate equipment before it was mounted on the AGFM sample holder. Although the AGFM itself can be used to ac demagnetise the sample it was not used in this study, because it was observed that when the AGFM is used to af demagnetise a sample, it always leaves the sample with a small residual remanence. $M_r(H)$ was measured by sequentially increasing the value of H while measuring the isothermal remanence for each H value. The $M_d(H)$ curve was measured by saturating the sample in a field of 1T and then sequentially increasing the field in the opposite direction to the saturation field while measuring the remanence for each value of H.

The total moment of lithographically produced samples of magnetite arrays of this study is weak (about $10^{-6}$ cgs or $10^{-9}$ $Am^2$), and the remanence was in most cases an order of magnitude smaller than this. This is close to the practical limit of the AGFM which is $10^{-8}$ cgs (i.e. $10^{-11}$ $Am^2$). Consequently the measured remanence curves are not smooth. Most of the curves were obtained with an averaging time of about 1 - 5 seconds in order to average out the effects of noise. It took about half an hour on average to complete measurement of a curve. In contrast, the hysteresis loops were

recorded using an averaging time of about 0.5 - 1 seconds. A loop was completed in a few tens of seconds in most cases.

Figure 6.8 (inset) shows a typical example of the measured remanence curves. It can be seen from this figure that despite attempts made to reduce the effects of noise due to vibration sources which does affect the AGFM performance, the data is still not smooth. One possible source of the observed noise is that which is a result of wind vibrations. Hence on a windy day as it was in most cases when the measurements were made, noise was inevitable. In order to determine the crossover point with clarity, the curves were smoothed with a moving average filter. Either a 3 or 5 point moving average filter was used to smooth remanence curves.

Figure 6.8 shows smoothed and normalised $M_d(H)$ and $M_r(H)$ plots as a function of applied field H for samples of arrays of non-interacting cubic magnetite particles. It can be seen from this figure that none of the non-interacting samples exhibits a crossover point of 0.5. The lower than 0.5 crossover point displayed by these samples is expected for interacting single domain particles. Since the particles are definitely non-interacting, it can be concluded that these samples do not contain single domain particles. This is consistent with the conclusions made earlier from coercivities and saturation remanence data. It can further be concluded that in general, non-interacting PSD cubic magnetite particles have lower than 0.5 crossover point for the $M_d(H)$ and $M_r(H)$ plots as a function of field.

In Figure 6.9, the remanence curves for 3 interacting samples are shown. In general, the crossover points for interacting particles are larger than those for non-interacting particles. Hence the effect of interactions in these samples seems to be to increase the crossover point. This is contrary to that expected for SD particles (Wohlfarth, 1958).

## 6.7 Domain Structure inferred from the coercivity ratio

The field at the point where the $M_d(H)$ curve has a zero value is known as the remanence coercivity ($H_{cr}$). The coercivity ratio $H_{cr}/H_c$ is often used in paleomagnetic studies as an indicator of the domain state of a sample. A sample composed of SD particles is expected to have a ratio in the interval 1.1 - 2 (Stoner and Wohlfarth, 1948; Gaunt, 1960). For PSD and MD samples the coercivity ratio $H_{cr}/H_c$ is expected to be in the interval 2 - 4 and 4 - 10 respectively (Wasilewski, 1973). Coercivity ratios of greater than

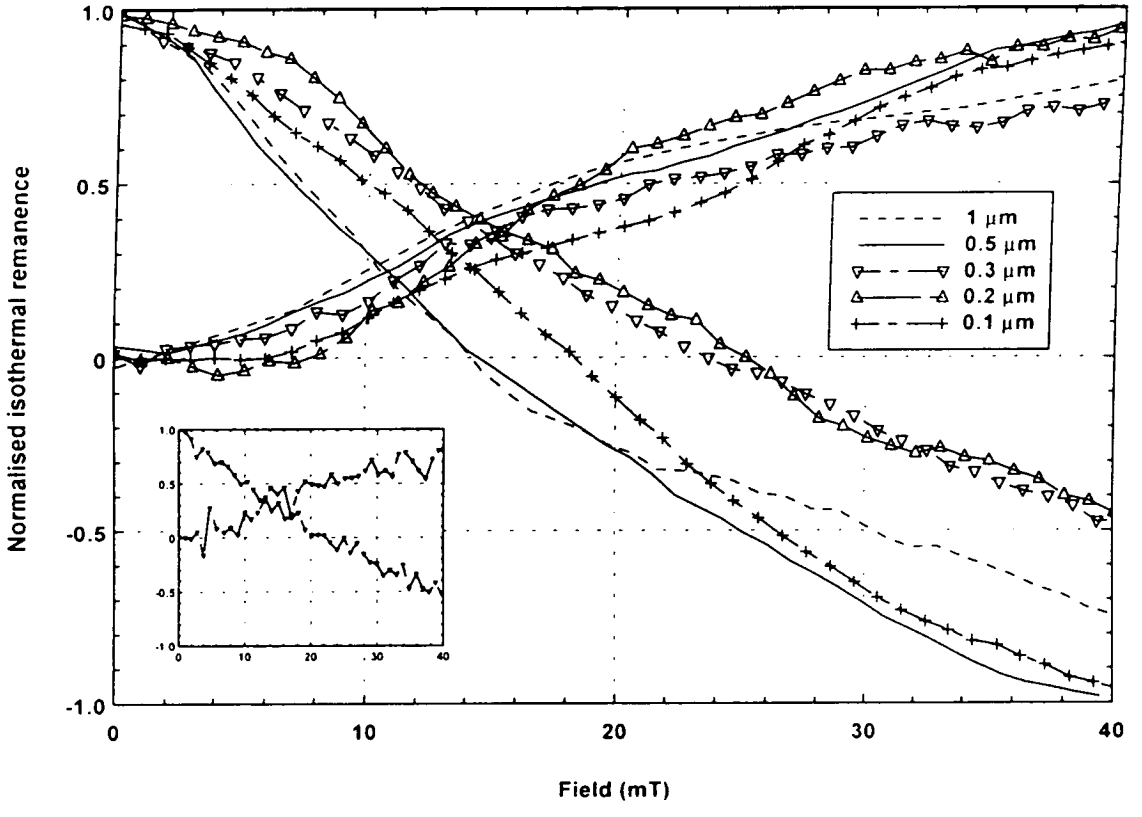


**Figure 6.8** Normalised acquisition and demagnetisation isothermal remanence curves (smoothed with a moving average filter) plotted as a function of the applied field for non-interacting arrays of cubic magnetite particles. Inset is a typical example of an unsmoothed curve.

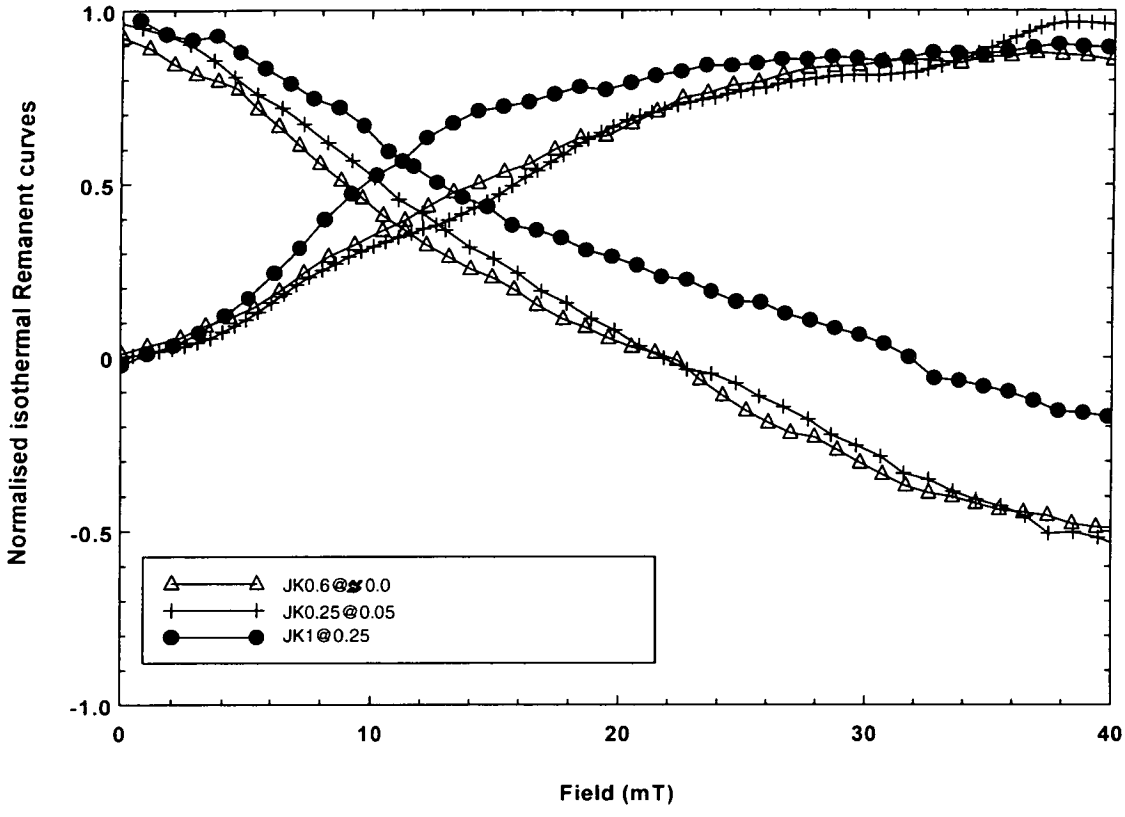


**Figure 6.9** Normalised acquisition and demagnetisation isothermal remanence curves as a function of applied field for interacting arrays of cubic magnetite particles (samples JK0.6@≈0.0, JK0.25@0.05 and JK1@0.25). See Table 6.1 for dimensions of these samples.

10 are expected for magnetite samples with a large amount of particles in the superparamagnetic size range (Dunlop, 1981).

The remanence coercivity values obtained from the curves shown in Figures 6.8 and 6.9 are shown in Table 6.1. In Figure 6.10 these $H_{cr}$ values are plotted against the $H_c$ values. Also shown in this figure are the boundary lines separating regions with different domain types. It can be seen from this figure that non-interacting samples plot within the SD and PSD regions without any clear size dependent pattern. This is contrary to the results of saturation remanence, coercivity, isothermal remanence magnetisation & demagnetisation plots for these samples discussed in the sections above which showed that the samples are not single domain. Since the samples are of uniform size and are not interacting, the discrepancy between expectation from this method of classification and observation cannot be assigned to particle interactions or different grain sizes in a sample as is often done when powdered samples are used.

In an attempt to determine the effects of particle interaction on the method of classification of domains by the coercivity ratios, the points for 3 interacting samples are also shown in Figure 6.10. Again no clear size dependency is observed. As Figure 6.10 illustrates, the plotted points for the sample of 1 μm interacting particles fall within the PSD and MD regions depending on the direction of the applied field to the substrate. This further shows the non-suitability of using this method of domain classification.

## 6.8 Summary

The coercivities of arrays of non-interacting cubic magnetite particles do not exhibit a sharp drop at the supposed single-domain to two-domain transition boundary which is predicted from hypothetical domain configuration structures. Instead a gradual decrease in coercivities with increasing particle size is observed. This observed behaviour is consistent with the mechanism of vortex nucleation and propagation predicted from unconstrained 3-D micromagnetic calculations.

The coercivities and saturation remanences of lithographically produced samples are slightly higher than those for laboratory grown magnetite crystals. This slight difference is probably due to inter-particle magnetostatic interaction effects in the latter, lab-grown sample.

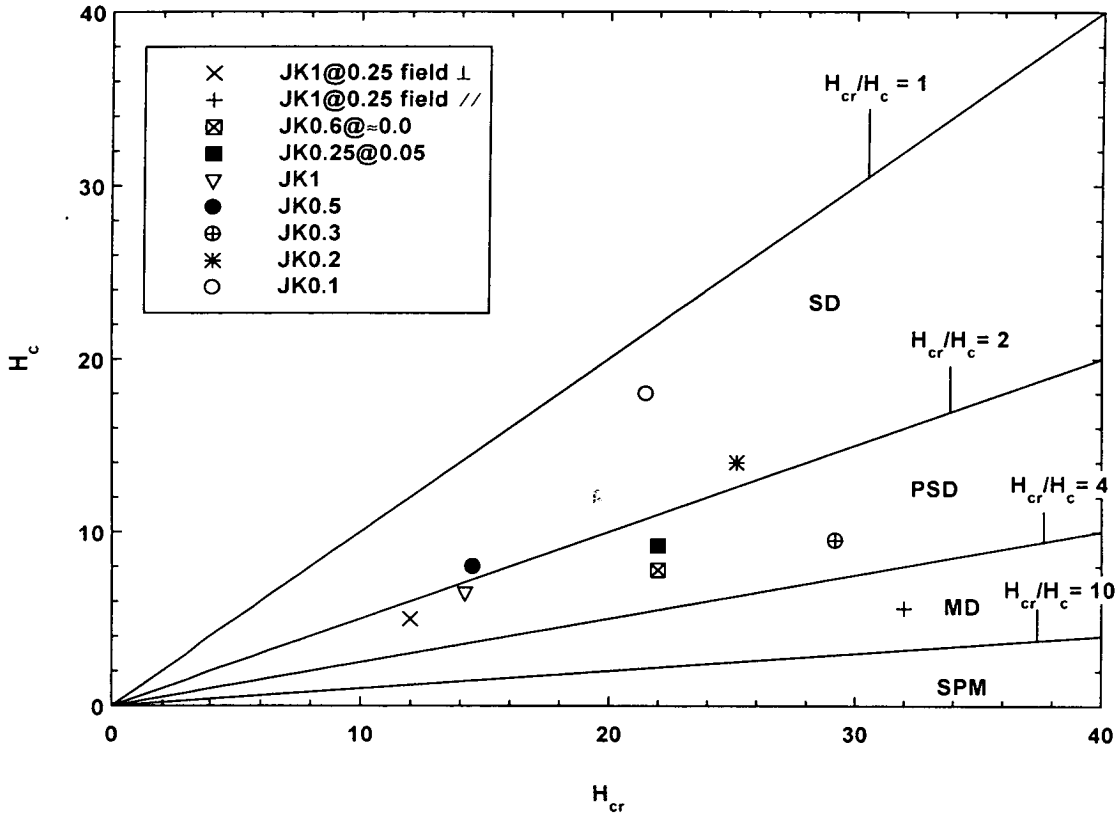


**Figure 6.10** Remanence coercivity ($H_{cr}$) plotted against coercivity ($H_c$) for interacting and non-interacting arrays of cubic magnetite particles. The sample dimensions are shown in Table 6.1. Lines showing expected regions for different domains are explained in the main text.

# Chapter 7 Magnetic properties of arrays of parallelepiped magnetite particles

## 7.1 Introduction

The magnetic properties of elongated magnetite particles whose dimensions are in the PSD size range are poorly understood. In chapter 6 we saw that the observed magnetic properties of equant lithographically produced PSD magnetite particles in the submicron size range were not consistent with predictions based on hypothetical domain configurations, but instead, were in good agreement with results of unconstrained 3-D micromagnetic calculations. In this chapter we check if the same is true for elongated particles.

Previous experimental studies have used artificially produced ellipsoidal shaped magnetite particles usually obtained from commercial companies (e.g. Davis and Evans, 1976). These particles whose aspect ratio (major axis/minor axis, length/width, a/b or simply q) is usually 6, are obtained in an intermediate process of the production of $\gamma$-$Fe_2O_3$ for magnetic recording media.

Apart from the fact that these samples contain magnetite particles which poorly resemble the shape of magnetite particles in rocks (which are usually parallelepiped), these particles are impossible to disperse completely as result of inter-particle magnetostatic forces, and hence particle clumping cannot be ruled out. In the following paragraphs, a description is given of typical environments of paleomagnetic interest where parallelepiped magnetite particles may be found.

Parallelepiped magnetite particles with dimensions in the submicron size range have been found in many environments of paleomagnetic interest. Studies of Modipe gabbro of Botswana by Evans et. al., 1969, identified submicron sized elongated grains with high aspect ratio within pyroxenes. Further studies on the same Modipe gabbros by Evans and Wayman, 1970, revealed parallelepiped grains of magnetite in the magnetite/ilmenite intergrowth with similar high aspect ratios. The coercivities of these particles were found to be as high as 180 mT. These high coercivities cannot be explained by the coherent rotation of atomic moments of a single domain controlled by magnetocrystalline anisotropy alone. Magnetite which is a result of magnetite/ilmenite intergrowth has also

been shown to be responsible for high paleomagnetic stability by Strangway, et. al., 1968. It is clear from the above examples that parallelepiped magnetite particles are important paleomagnetic carriers in igneous rocks.

Some types of bacteria found in both freshwater and marine environments utilise chains of magnetite particles (also known as magnetosomes) within their bodies for navigation. These magnetotactic bacteria were first described by Blakemore (1975). Most of these bacteria produce magnetite particles which are parallelepiped in shape. Their sizes are often in the submicron size range. Figure 7.1 shows typical SEM pictures of bacteria magnetite. After the death of these bacteria, magnetosomes are preserved in deep-sea sediments and become paleomagnetic carriers. Evidence of magnetosomes in rocks of paleomagnetic interest includes Quaternary unconsolidated sediments, Quaternary to Tertiary deep-sea sediments, Jurassic limestones (Vali et. al., 1987) and Precambrian rocks (Ferris et. al., 1986). It is clear from the above studies that parallelepiped magnetite particles are important paleomagnetic carriers in these environments.

Magnetic properties of arrays of parallelepiped magnetite particles produced by the method of electron-beam lithography are presented in this chapter. Some of these samples are not strictly sharp edged due to their method of production which involved the oxidation of Fe to $Fe_3O_4$ (see chapter 2 section 2.5.2 and chapter 3 section 3.5.4). However, elongated magnetite particles of paleomagnetic interest are often not strictly sharp edged either (Figure 7.1). The samples presented in this chapter include both interacting as well as non-interacting arrays of magnetite particles. Also presented for comparison purposes are samples composed of ellipsoidal magnetite particles which are in powder form. These particles were produced by the method of annealing maghemite as described in chapter 2 section 2.6.3. These samples have narrower size distribution (<10% standard deviation). Their size distribution variation is slightly larger than that of lithographically produced samples which is less than 5% in general. The dimensions and magnetic properties of the samples used in this chapter are summarised in Table 7.1.

Figures 7.2 & 7.3 shows typical SEM pictures of lithographically produced non-interacting parallelepiped magnetite particles while interacting particles are shown in Figures 7.4 & 7.5.

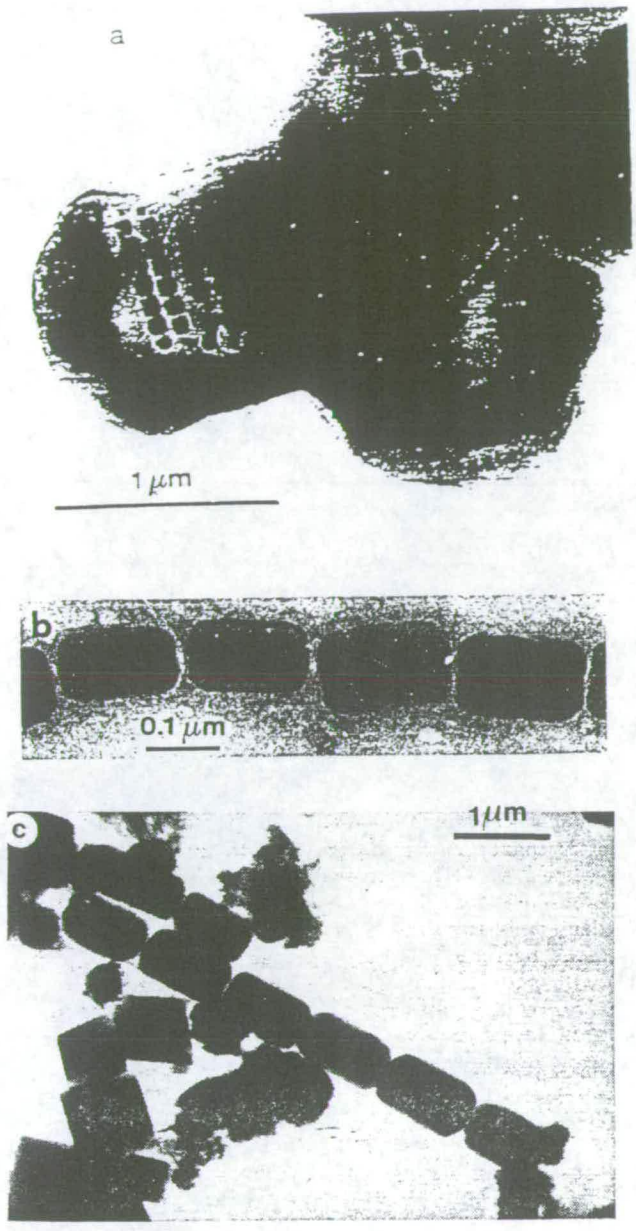


**Figure 7.1** SEM pictures of examples of magnetosomes from different environments of paleomagnetic interest, (a) fresh water mud, (b) Quaternary unconsolidated sidements, (Vali et. al., 1987) & (c) Eocene deep sea sediments of the Angola basin (Petersen et. al., 1986).

| Sample name | Sample dimensions (μm) & orientation | Coercivity $H_c$ (mT) | Normalised saturation remanence ($M_{rs}/M_s$) | Crossover point | Remanence coercivity ($H_{cr}$) |
|---|---|---|---|---|---|
| JKL0.1x0.5 | 0.1x0.1x0.5 // | 29 | 0.53 | 0.26 | 30 |
| | " " " ⊥ | 44 | 0.44 | 0.27 | 53 |
| JKL0.2x1 | 0.2x0.2x1 // | 11 | 0.15 | 0.41 | 23 |
| | " " " ⊥ | 13 | 0.11 | 0.13 | 24 |
| JKL0.3x1.5 | 0.3x0.3x1.5 | 15 | 0.25 | 0.43 | 27 |
| | " " " ⊥ | 18 | 0.23 | 0.35 | 32 |
| JKL0.5x2.5 | 0.5x0.5x2.5 // | 18 | 0.30 | 0.27 | 35 |
| | " " " ⊥ | 10 | 0.15 | 0.24 | 34 |
| JKL1x5 | 1x1x5 // | 8 | 0.17 | 0.26 | 35 |
| | " " " ⊥ | 10 | 0.13 | 0.20 | 37 |
| JKL0.5@0.6 | 0.5x0.5x2 at Sapcing 0.6 by 2 // | 27 | 0.42 | 0.25 | 45 |
| | " " " ⊥ | 19 | 0.21 | 0.26 | 36 |
| JKL0.5@0.1 | 0.5x0.5x1 at Sapcing 0.1 by 0.8 // | 43 | 0.48 | 0.19 | 60 |
| | " " " ⊥ | 32 | 0.32 | 0.3 | 52 |
| JG3 | 0.12x0.34 ellipsoid | 23 | 0.23 | | |
| JG6 | 0.084x0.5 ellipsoid | 26 (10%)<br>26 (1%)<br>25 (0.1%)<br>24 (0.01%) | 0.29 (10%)<br>0.29 (1%)<br>0.28 (0.1%)<br>0.27 (0.01%) | | |

**Table 7.1** Table showing the dimensions and values of magnetic parameters for samples used in this chapter. The symbol // is for the field applied parallel to the major axis of the particles while ⊥ is for the perpendicular case. The percentage values shown besides thecoercivity and remanence values indicate the amount of magnetite dispersed into $CaF_2$ matrix.

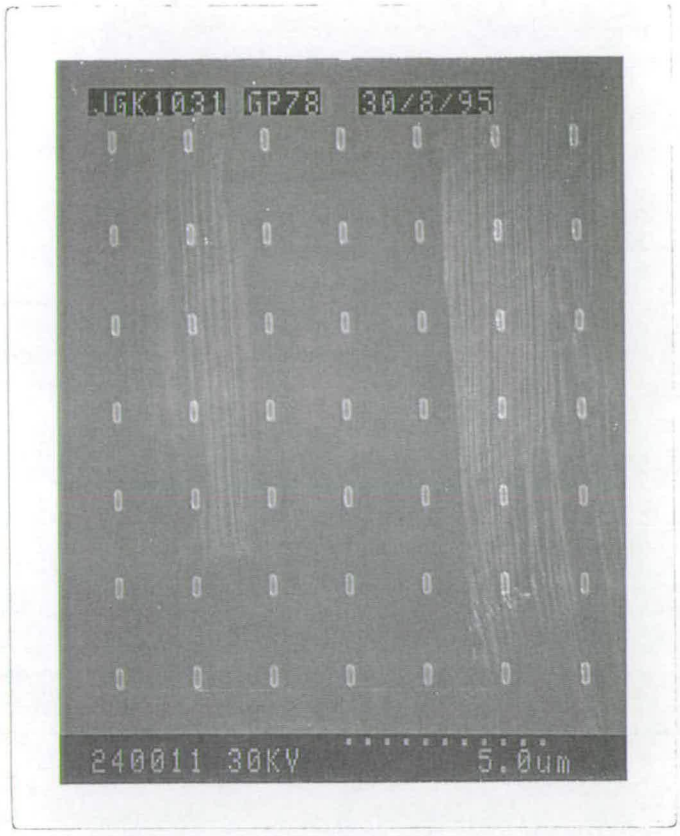


**Figure 7.2** A SEM picture of a typical examples of lithographically produced arrays of non-interacting parallelepiped magnetite particles. The picture is for sample JKL0.1x0.5 whose dimensions are shown in Table 7.1.

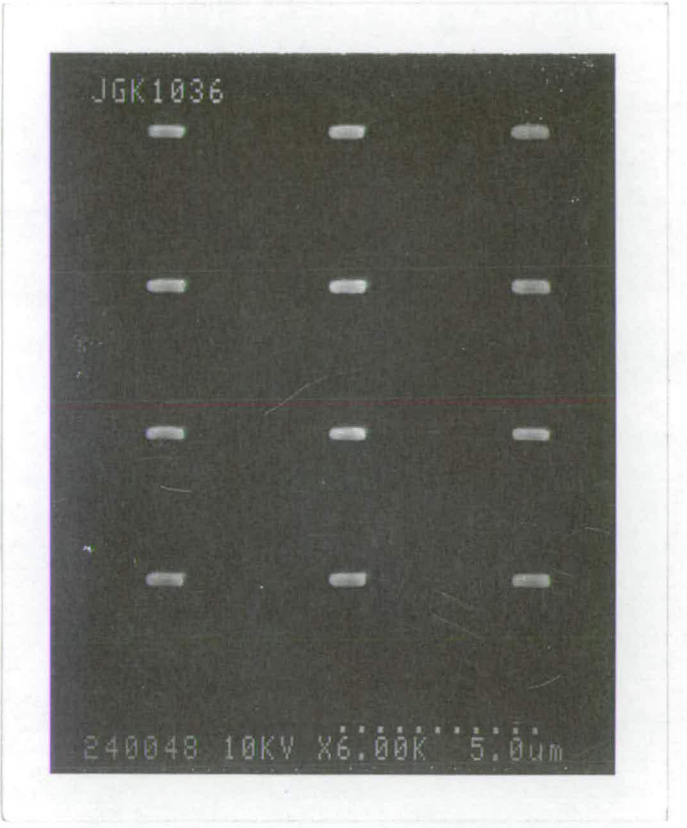


**Figure 7.3** A SEM picture of a typical examples of lithographically produced arrays of non-interacting parallelepiped magnetite particles. The picture is for sample JKL0.2x1 whose dimensions are shown in Table 7.1.

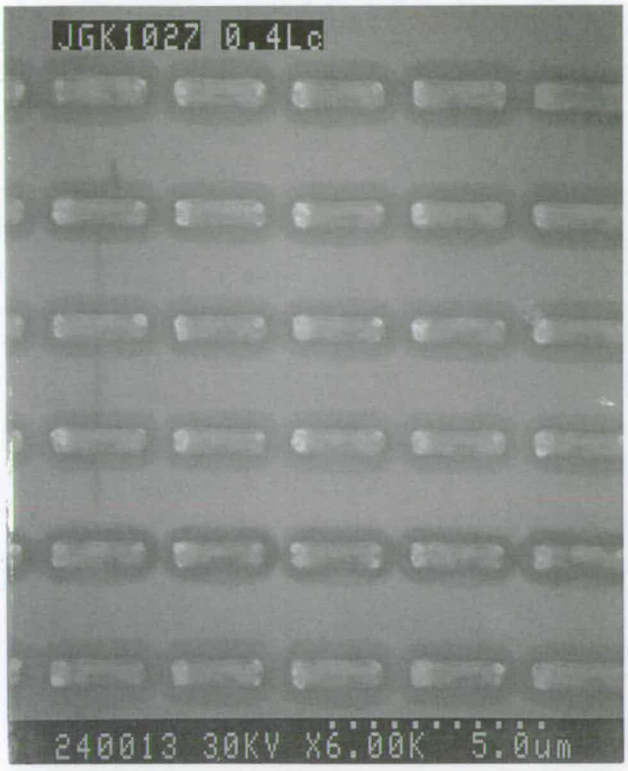


**Figure 7.4** A SEM picture for sample JKL0.5@0.6 whose dimensions are shown in Table 7.1.

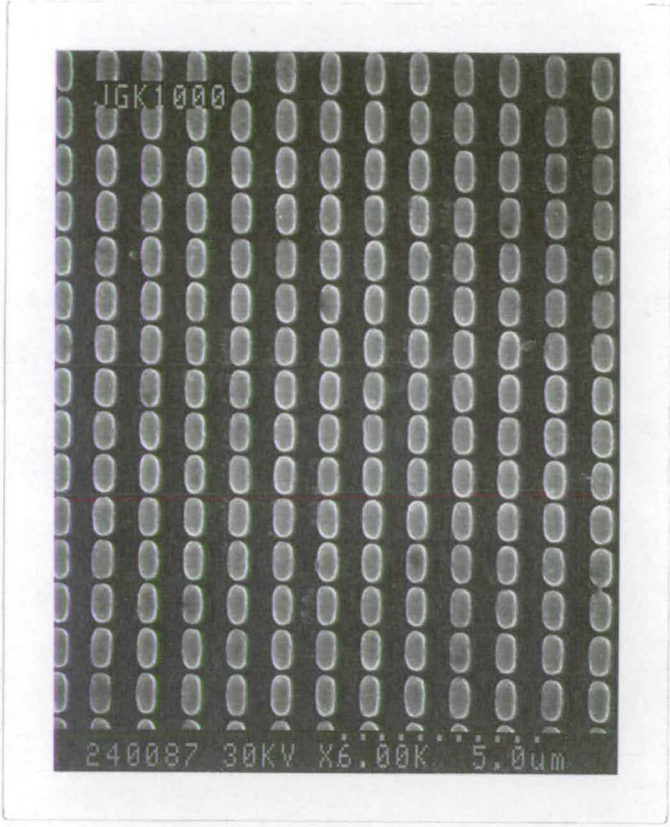


**Figure 7.5** A SEM picture for sample JKL0.5@0.1 whose dimensions are shown in Table 7.1.

## 7.2 Domain boundary calculations for elongated particles

In rock magnetism, a popular way of classifying magnetite properties of elongated particles is to plot the particle length as a function of aspect ratio and compare it to theoretically calculated boundaries for the stability of single-domain particles. Figure 7.6, shows an example of such a plot for magnetite particles of the Modipe gabbros of Botswana. The curves showing the domain boundaries were calculated assuming the magnetite particle to be a prolate spheroid. Figure 7.7 shows a plot for the samples used in this chapter. Since both parallelepiped and ellipsoidal shaped magnetite particles are used in this chapter, the boundaries for SD stability regions are shown for prolate spheroids as well as parallelepiped magnetite particles. The curves for the boundaries shown in Figure 7.7 were obtained from Figures 3 & 4 of Diaz Ricci and Kirschvink (1992).

The calculation of the SPM-SD stability boundary is done by equating the energy required to reverse aligned atomic moments of a particle to thermal energy which tend to randomise their alignment. This is done by substituting appropriate values into the Neel's (1955) relaxation equation

$$\tau = f_o^{-1} . e^{(\upsilon H_c M_s / 2kT)} \qquad (7.1)$$

where $\tau$ is the relaxation time in seconds, $f_o^{-1}$ is the frequency factor (= $10^9$ per second), $\upsilon$ is the particle volume, $H_c$ is the coercivity, $M_s$ is the saturation magnetisation for magnetite, k is the Boltzman constant and T is the absolute temperature. The coercivity is assumed to be entirely due to shape anisotropy and given by the Stoner and Wohlfarth theory (1948) for the prolate spheroid as follows,

$$H_c = (N_b - N_a)M_s \qquad (7.2)$$

where $N_b$ and $N_a$ are the demagnetisation factors along the minor and major axis respectively. For a prolate spheroid shaped particle, from Morrish, 1965 (pp.10), the demagnetising factors are given by

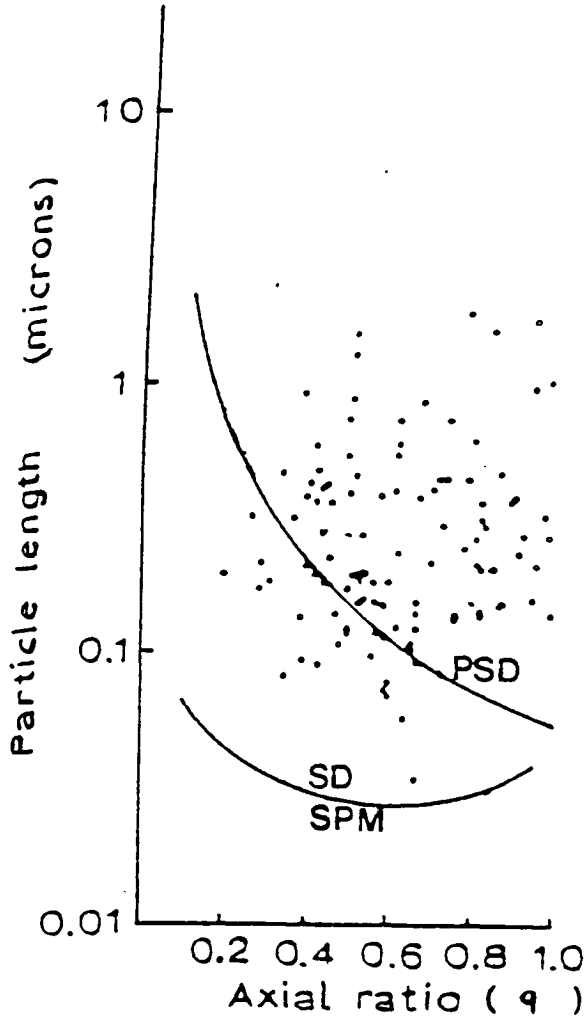


**Figure 7.6** Measured dimensions of 115 discrete magnetite particles from the Modipe gabbro of Botswana plotted on a diagram showing the expected domain stability for SD ellipsoidal particles (Evans and Wayman, 1970).

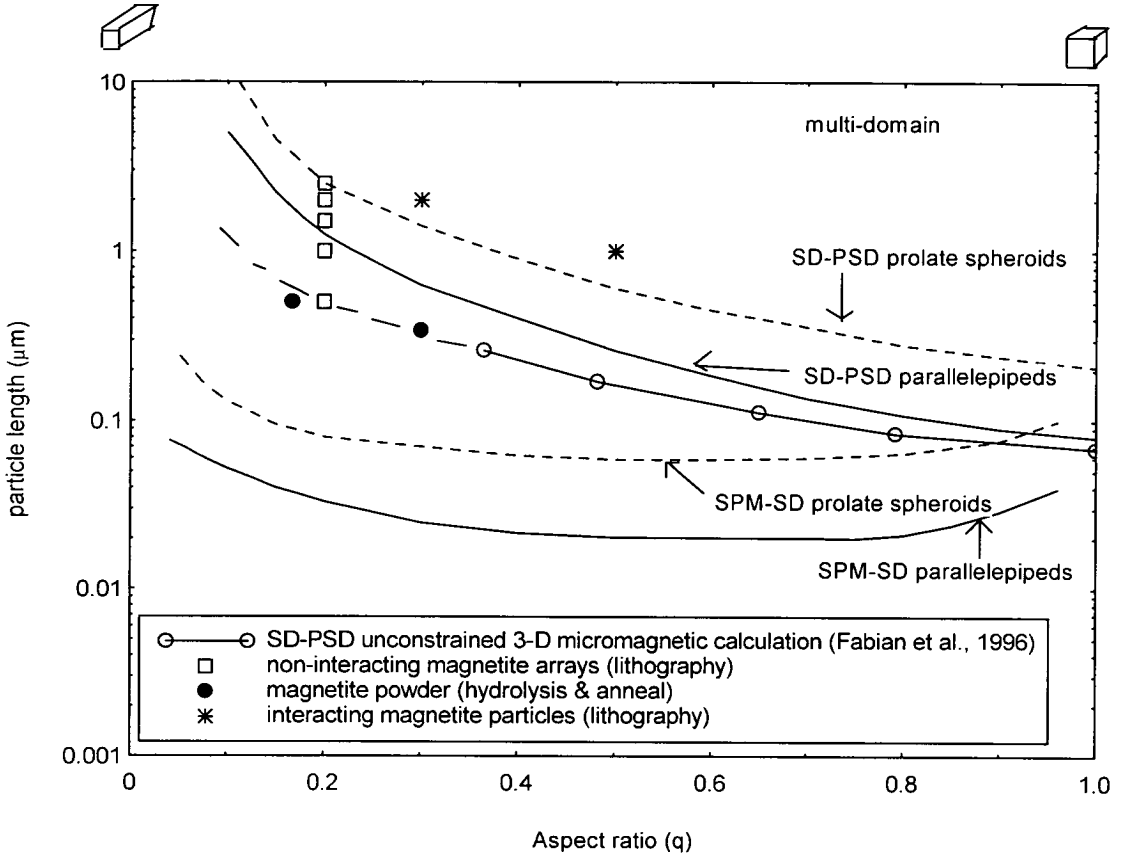


**Figure 7.7** Theoretically calculated single-domain stability region for elongated magnetite particles compared to plotted points for samples of this study. All the domain region boundaries shown, with the exception of that for 3-D micromagnetic calculations (data from Fabian et al., 1996), were calculated from hypothetical based domain configurations as explained in the text.

$$N_b = N_b = 0.5(4\pi - N_a) \quad (7.3)$$

and

$$N_a = 4\pi/(q^2-1)\{q/(q^2-1)^{1/2}\ln[q+(q^2-1)^{1/2}]-1\} \quad (7.4)$$

For the calculation of the coercivity of a parallelepiped magnetite particle, the reader is referred to a paper by Diaz Ricci and Kirschvink (1992).

The calculations for the single-domain to two domain (or PSD) boundary for a prolate spheroid are achieved by equating the exchange energy involved in a circular spin configuration to the magnetostatic energy of a SD particle according to Morrish and Yu, 1955. The expression used is given by Diaz Ricci and Kirschvink (1992) as

$$a^2/\ln[2.38.10^7.(a/q)-1] = 24.72 \times 10^{-12}.(q^2/N_a) \quad (7.5)$$

For parallelepipeds, the SD-2D boundary line was determined by comparing the SD energy to magnetostatic and domain wall energies. Unlike in Kittel's (1949) derivation, where the energy contribution due to free magnetic poles of domain walls was assumed to be negligible, here it was included. Also included is the dependence of domain wall energy on the wall width. For details of the calculations the reader is again referred to Diaz Ricci and Kirschvink, (1992).

It should be noted here that these calculations are based on hypothetical structures for reasons of simplicity of calculations. Relatively unconstrained 1-D micromagnetic formulations have been used by Enkin and Dunlop (1987) to calculated the SD-2D boundary. Their results showed an increase in the SD-2D boundary with magnetite particle aspect ratio in agreement with that shown in Figure 7.7 for parallelepiped particles. In contrast, the lower boundary for SD-PSD from 3-D micromagnetic calculations of Fabian et al., 1996, has lower values than that of Enkin and Dunlop (1987), and as well those calculated from hypothetical domain configurations. In Figure 7.7, the boundaries showing the domain stability are shown.

It can be seen from Figure 7.7, that the samples JKL0.1x0.5 and JKL0.2x1 and as well JG3 should contain SD particles according to the curves for parallelepiped particles calculated from hypothetical domain configurations while according to the lower boundary for SD-PSD prediction from 3-D micromagnetic calculations, these samples may not contain SD particles. The measured magnetic properties of the samples used in this chapter will be compared to these contrasting predictions.

## 7.3 Hysteresis loops for arrays of non-interacting parallelepiped magnetite particles

Figure 7.8 shows hysteresis loops for samples of non-interacting parallelepiped magnetite particles with the field applied along (curve marked by unbroken line) and perpendicular (curve marked by symbols) to particle's length respectively. Only the narrowest sample (JKL0.1x0.5) shows a visible difference between the loop obtained with the field applied along and perpendicular to the particle's length. However this difference is still much smaller than that expected for SD particles (Stoner and Wohlfarth, 1948). For SD the loop for the field perpendicular to the major axis should be a straight line from the positive saturation field through the origin to the negative saturation field. Hence the hysteresis loop of this sample and that of JKL0.2x1 is not consistent with the prediction based on hypothetical domain configurations which shows both these particles to be SD but is in agreement with that of 3-D micromagnetic calculations (see Figure 7.7).

## 7.4 Hysteresis loops for interacting elongated magnetite particles

Figure 7.9 (a) and (b) shows loops for lithographically produced arrays of interacting magnetite particles. These samples JKL0.5@0.6, and JGL0.5@0.1, (see Table 7.1 for dimensions), have inter-particle spacing along the particle's length of 0.6 μm and 0.1 μm respectively. Their inter-particle spacing along minor axis of the particles is 2 μm and 0.8 μm for sample JKL0.5@0.6, and JGL0.5@0.1, respectively (see Figures 7.4 & 7.5 for SEM pictures). The loop obtained with a field direction in the major axis of the particle is indicated by unbroken line while those obtained with the field in the direction perpendicular to the particle's major axis is shown by

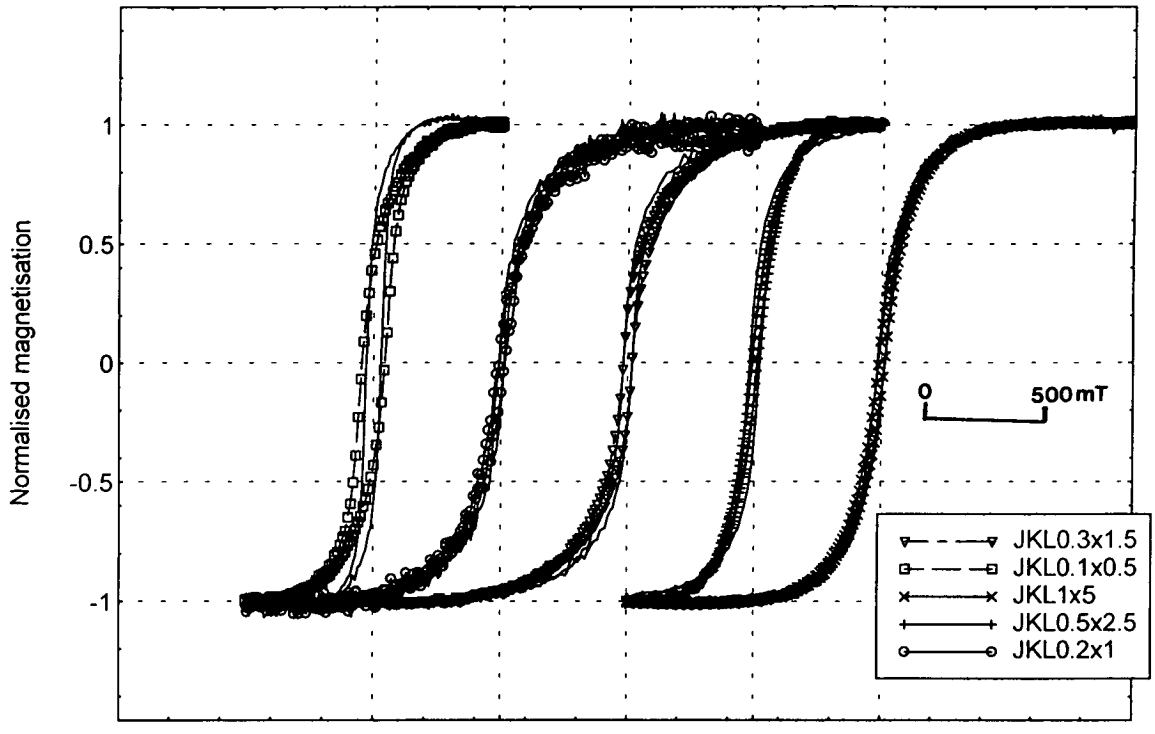


**Figure 7.8** Hysteresis loops for lithographically produced arrays of non-interacting parallelepiped magnetite particles.

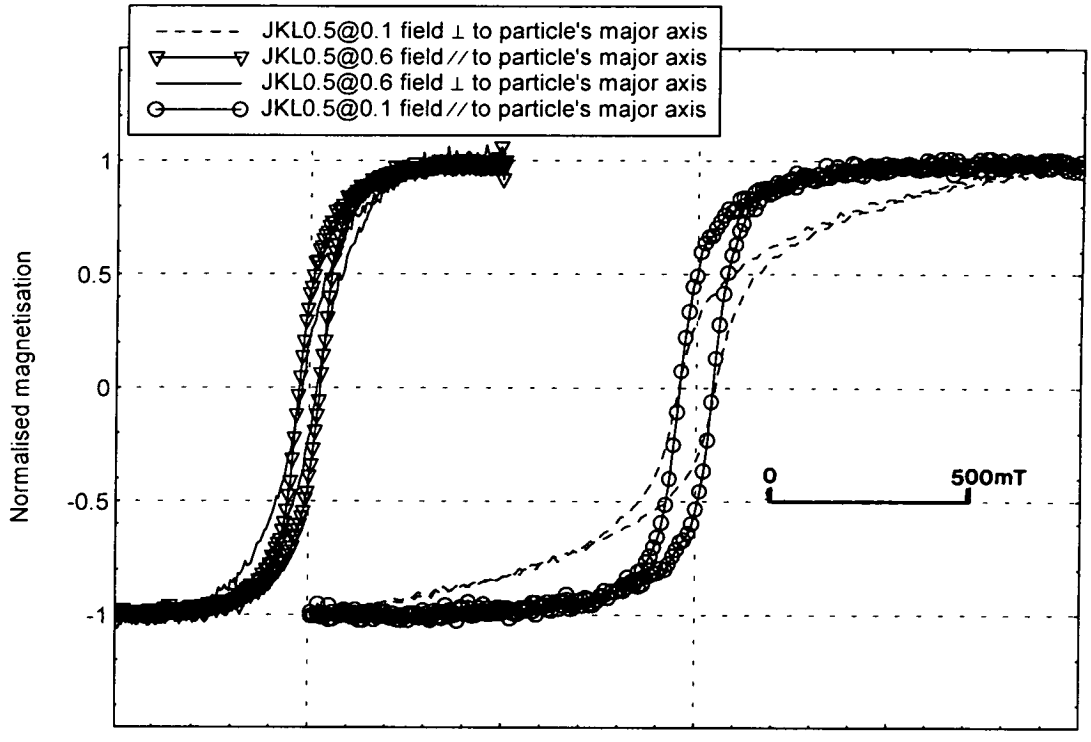


**Figure 7.9** Hysteresis loops for interacting arrays of parallelepiped magnetite particles. The loops for the samples with the smallest interparticle spacing (i.e. sample JKL0.5@0.1) is much wider than that for sample JKL0.5@0.6.

dashed lines. It can be seen from this figure that a decrease in inter-particle spacing lead to a widening of the loop. Thus particle interactions significantly affect hysteresis loops.

## 7.5 Coercivities of elongated non-interacting magnetite particles

In Figure 7.10, the coercivity of non-interacting lithographically produced magnetite particles is plotted as a function of magnetite particle width. The aspect ratio (length/width) for this particles is 5. Also plotted in Figure 7.10 are the coercivities of cubic particles shown in Figure 6.4, chapter 6. In general, the coercivities of elongated magnetite particles are larger than those for equant particles. Figure 7.10 (inset curve, dashed line marker), shows the expected coercivity plot for these samples assuming SD particles controlled by shape anisotropy according to SW theory. Equation 7.2 was used to calculate the coercivity for this curve. It can be seen from this figure that the measured coercivities for these samples are far smaller than those expected from coherent rotation theory. Hence none of the samples is SD. This observation is not consistent with domain prediction based on hypothetical domain configurations, but is consistent with unconstrained 3-D micromagnetic calculations (Figure 7.7).

A gradual decrease in coercivity with increase in particle width is evident in Figure 7.10. This behaviour is consistent with 3-D micromagnetic calculations but is inconsistent with magnetic properties based on hypothetically domain configuration which predicts a sharp transition in magnetic properties at the supposed SD to 2 domain boundary.

Figure 7.11 shows the angular dependence of coercivity for the sample with the smallest particle size (i.e. sample JKL0.1x0.5). It can be seen from this figure that as the angle the field makes with the major axis of the particle increases, so does the coercivity.

There are no unconstrained 3-D micromagnetic calculations showing the mechanism of reversal for a range of elongated magnetite particles in the PSD size range as the field is applied from one saturation direction to the opposite saturation direction in the literature.

From the observed behaviour of the samples of this chapter, it may be concluded that the mechanism of reversal of magnetisation is non-coherent rotation of atomic magnetic moments. A possible mechanism of reversal is that of vortex nucleation and propagation similar to that obtained by Schabes

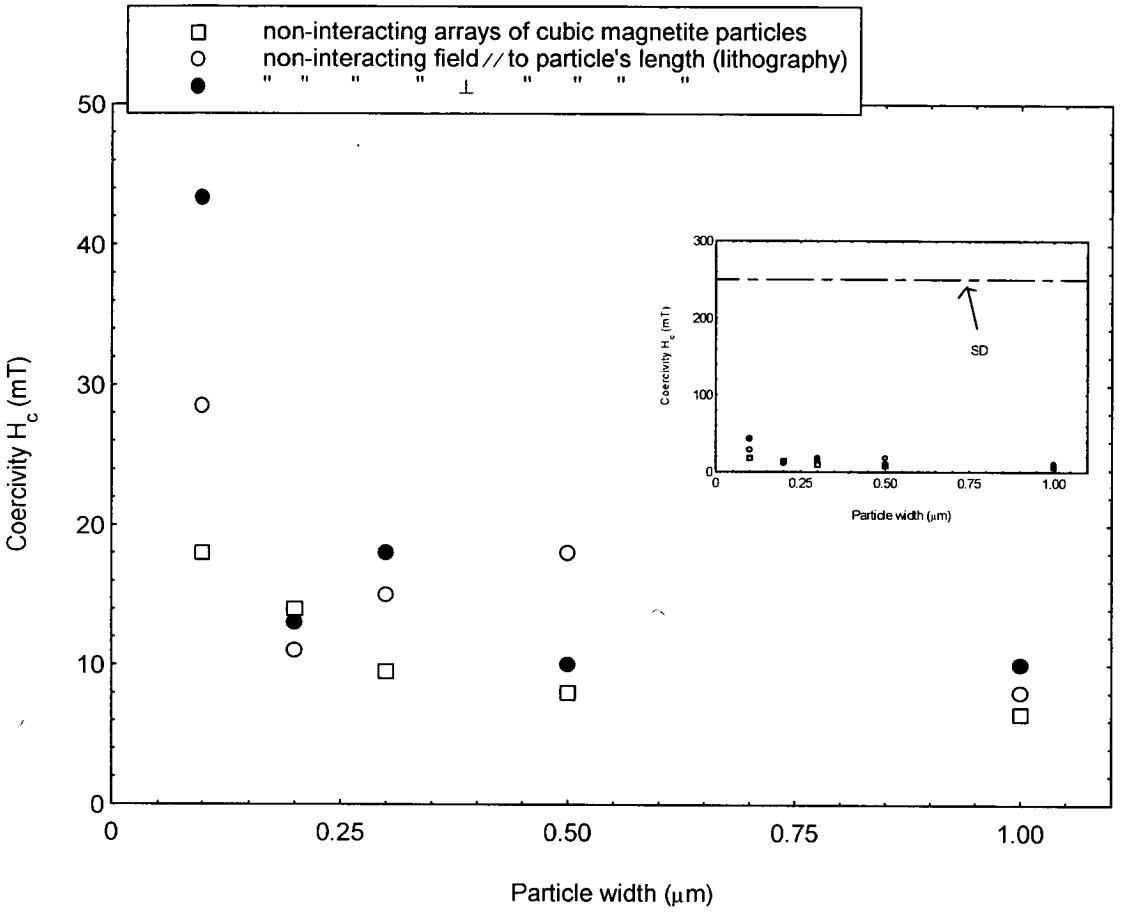


**Figure 7.10** Coercivities as a function of particle width for lithographically produced non-interacting arrays of parallelepiped magnetite particles. The particles have an aspect ratio of 5. Insert is the same figure compared to the coercivity calculated assuming the particles to be single-domain (dashed line). The Stoner and Wohlfarth (1948) theory was used in this calculation.

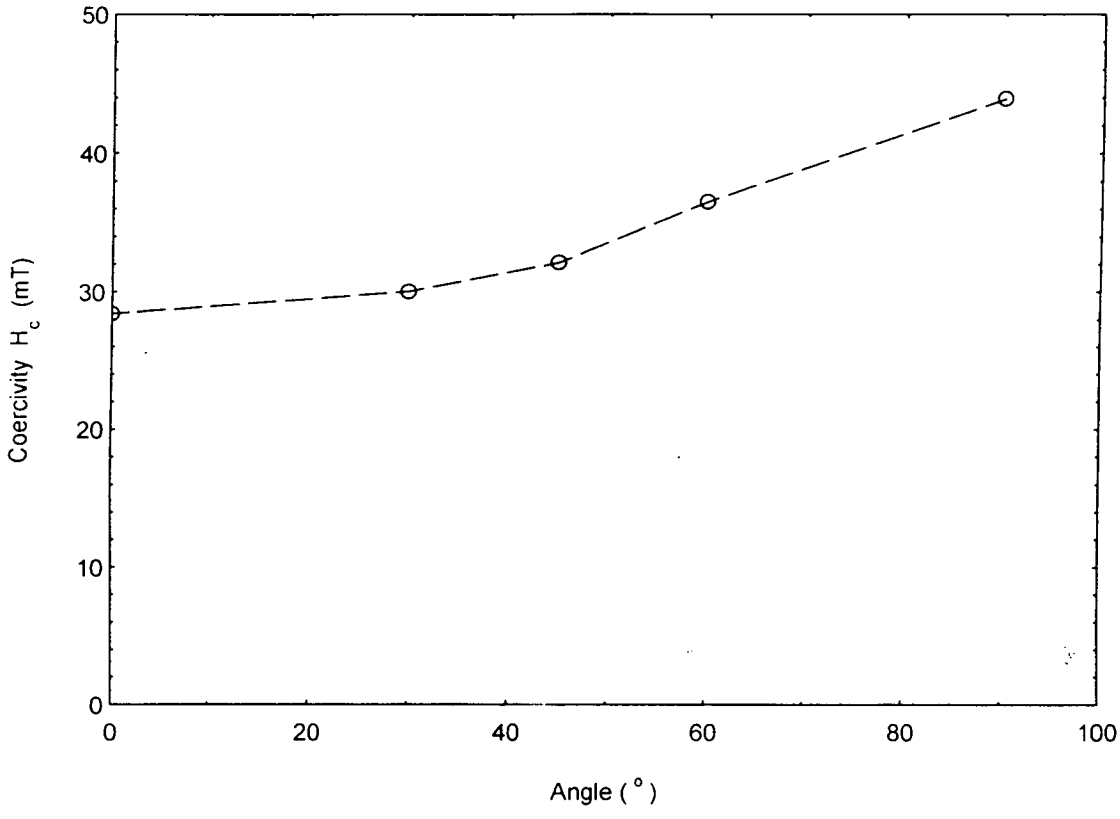


**Figure 7.11** Coecivity as a function of the angle between the field direction and the particle's major axis for sample JKL0.1x0.5.

& Bertram (1988) and Schabes (1991) for rectangular parallelepiped maghemite particles with an aspect ratio of 5. Their unconstrained 3-D micromagnetic calculations revealed that upon application of an increasing reverse field to a previously saturated maghemite particle, a vortex structure is formed at either end of the particle. This vortex region expands from the particle's ends towards its centre as the reverse field is increased (Figure 5 of the paper by Schabes, 1991).

Schabes interpreted the observed gradual decrease in the coercivity with increasing particle width as being due to the weakening of the exchange interaction and hence allowing a large fraction of the particle to be occupied by the vortices at the end of the particle at a smaller value of the applied field. Such a mechanism may explain the observed coercivity data for the samples of this chapter.

## 7.6 Coercivities of elongated interacting magnetite particles

Figure 7.12 shows a plot of coercivities as a function of particle width for lithographically produced arrays of interacting particles and as well magnetite powders obtained by annealing maghemite. The points marked with plus signs for sample JG6, are for various concentrations of magnetite dispersed in $CaF_2$. An increase in coercivity with decreasing magnetite concentration from 24.5 mT (10% magnetite by weight) to 26 mT (magnetite by weight 0.01%) was observed. It is clear from this observation that inter-particle interactions has an effect on the observed coercivities of elongated particles in the PSD size range.

The coercivity for sample JG3 which has an aspect ratio of 3 has a smaller value than that of JG6 whose aspect ratio is 6. Although the width of the particles in these two samples differ slightly (0.12 μm for JG3 and 0.084 μm for JG6), it is most likely that this observed coercivity difference is a reflection of the difference in the aspect ratio.

In contrast to the behaviour of magnetite powder, the coercivity of lithographically produced samples (Figure 7.12), increases with decreasing particle spacing along the particle's length. This observed difference is most likely a reflection of particle arrangement which is chain-like for lithographically produced arrays of magnetite particles and random for

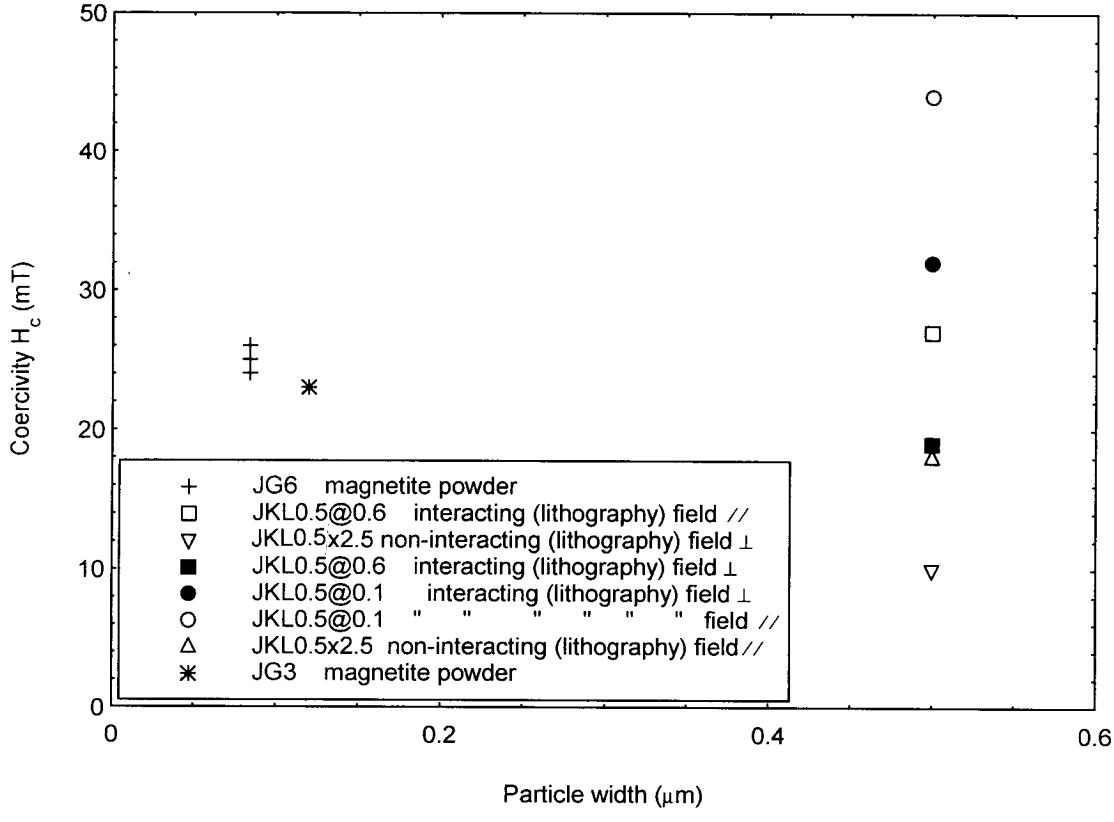


**Figure 7.12** Coercivities plotted as a function of particle width for elongated interacting magnetite particles. The points for sample JG6 are explained in the main text.

magnetite powder. Thus the paleomagnetic stability of magnetosomes may be partly due to their chain arrangement.

## 7.7 Saturation remanence of elongated non-interacting magnetite particles

In Figure 7.13, normalised saturation remanence for non-interacting lithographically produced parallelepiped magnetite particles is plotted as a function of particle width. The largest value of normalised saturation remanence of 0.53 for sample JKL0.1x0.5 is smaller than the expected value from the Stoner and Wohlfarth (1948) theory. For SD oriented particles controlled by shape anisotropy, the expected normalised saturation remanence when the field is along the particle's major axis, is 1. The observed value for this sample is, however, higher than that expected from the same theory for randomly oriented particles with uniaxial anisotropy which should have a value of 0.5. Since the samples used are shape oriented, the later does not apply in the present case. Thus both sample JKL0.1x0.5 and JKL0.2x1 do not contain single domain particles. This observation is contrary to domain classification based on hypothetical domain structures, but is consistent with predictions of 3-D micromagnetic calculations (see Figure 7.7).

The rest of the samples plotted in Figure 7.13 have normalised saturation remanence values which are much lower than 0.5. It can be concluded from this observation that the mechanism for reversal of magnetisation for these samples involves non-uniform rotation of atomic moments.

In general, normalised saturation remanence decreases gradually with increasing particle width. Unconstrained 3-D micromagnetic calculations done by Schabes (1991), for rectangular parallelepiped maghemite particles with an aspect ratio of 3, also show a gradual decrease in normalised saturation remanence with increasing particle width (Figure 11 of his paper). Although the normalised saturation remanence values obtained by Schabes (1991) are much higher than those of the present study (e.g. 0.53 for this study compared to >0.8 from Schabes for a particle of width is 0.1 μm), from the similarities in the trend of remanence decrease with increasing particle width, it may be possible that the mechanism of reversal is similar.

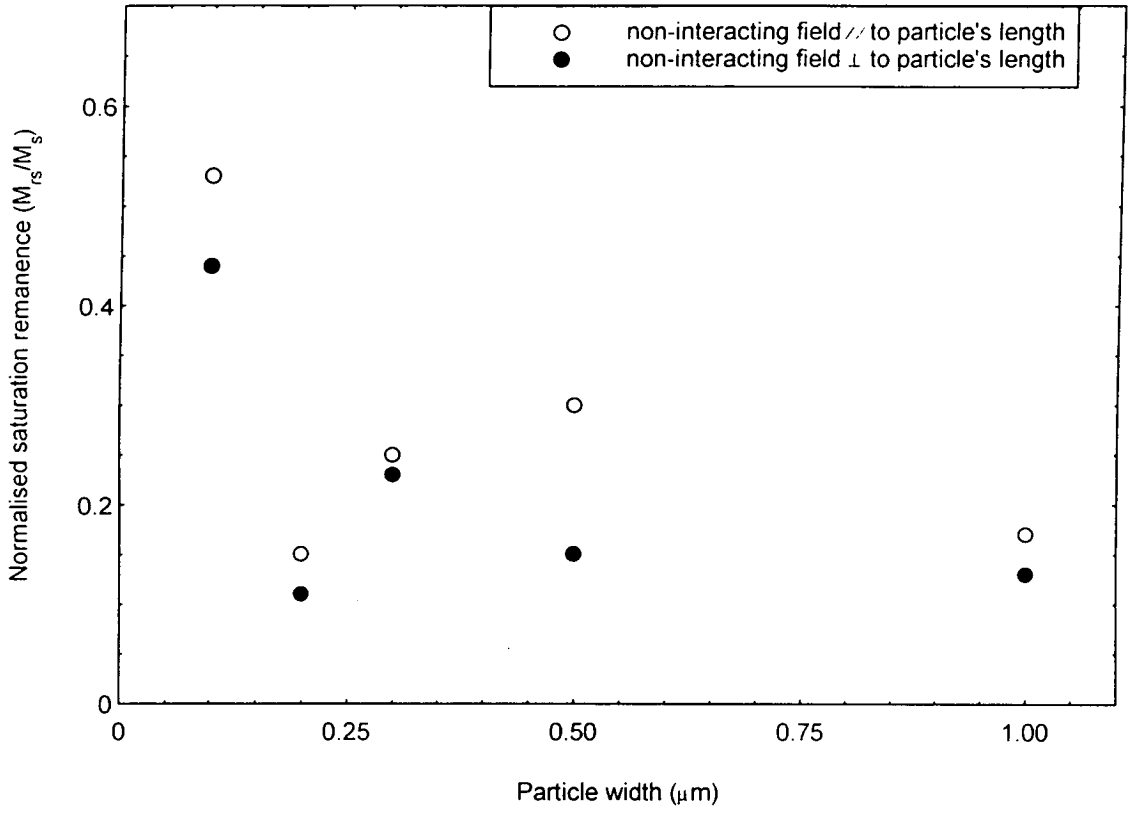


**Figure 7.13** Normalised saturation remanence ($M_{rS}/M_S$) plotted as a function of particle width. A gradual decrease in $M_{rS}/M_S$ with increase in particles width is evident from this figure. The particles have an aspect ratio of 5.

Figure 7.14 shows a plot of normalised saturation remanence for interacting particles. For magnetite powder (sample JG6), a small increase in normalised saturation remanence with decreasing magnetite concentration can be seen in this figure. The point with the lowest value of saturation remanence for this sample, is for 10% by weight magnetite dispersed in $CaF_2$ while the highest plotted point is 0.01%.

In contrast, lithographically produced samples shows an increase in normalised saturation remanence with increasing concentration (i.e. decreasing inter-particle spacing). It could be expected that elongated magnetite particles of paleomagnetic interest (e.g. magnetosomes), would have higher normalised saturation remanence as a result of inter-particle interactions.

## 7.8 IRM curves

As pointed out in chapter 6, the point where the isothermal acquisition remanence ($M_r(H)$) curve crosses the DC demagnetisation remanence ($M_d(H)$) curve (hereafter referred to as 'crossover point'), is used in rock and paleomagnetic studies to infer the nature of particle spacing in a sample. The crossover points are tabulated in Table 7.1. All the samples shown in this table exhibit crossover points which are smaller than 0.5, hence none of the samples contain SD particles. This observation is inconsistent with hypothetical domain configuration calculated boundaries shown in Figure 7.7, but is consistent with that obtained using unconstrained 3-D micromagnetic calculations.

In Figure 7.15, the coercivity ($H_c$) values for lithographically produced arrays of parallelepiped magnetite particles are plotted as a function of the remanence coercivity ($H_{cr}$). The boundaries for different domain regions are indicated by straight lines. Most of the samples plot on the region expected for single domains. This observation which agrees with hypothetical domain configuration based predictions (see Figure 7.7), is contrary to observed coercivities and normalised remanence which showed that none of the particles is SD. Again as with the observed plot for cubic particles, (chapter 6, Figure 6.10), the results do not fit into this classification scheme. This is mainly a reflection of the mechanism of reversal of magnetisation which is vortex nucleation and propagation which is not accounted for in the determination of these boundaries.

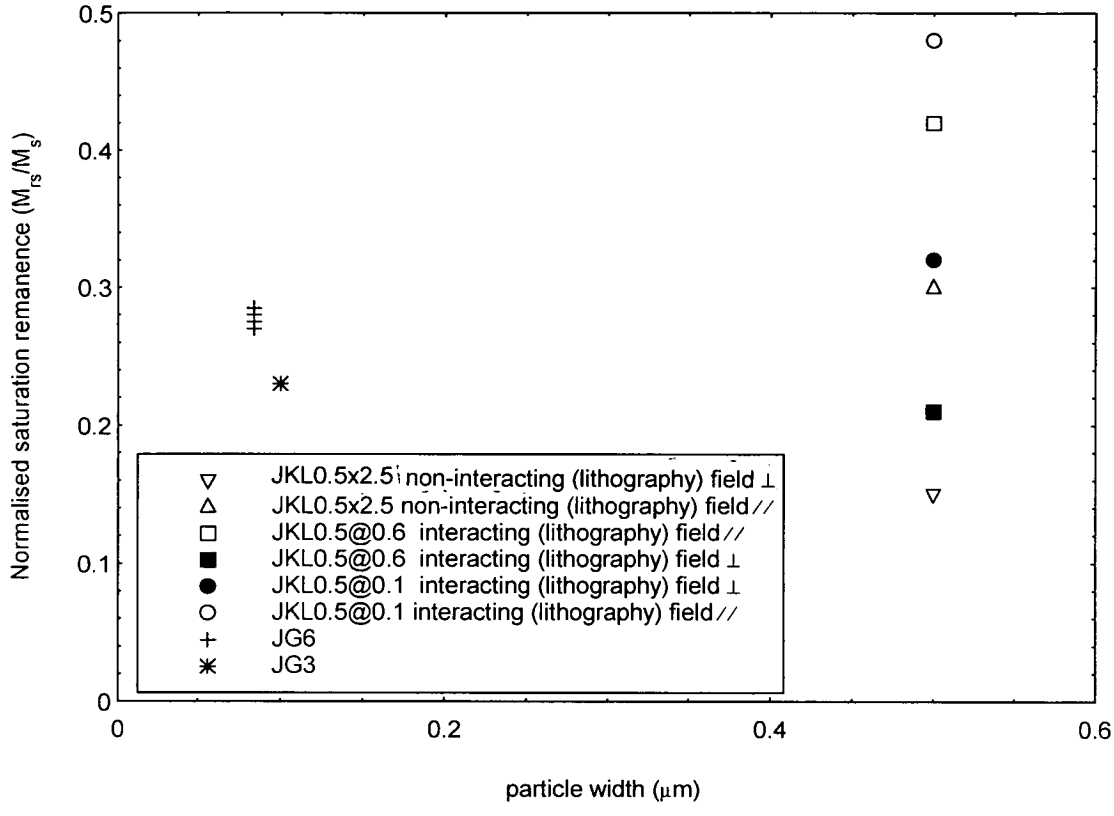


**Figure 7.14** Normalised saturation remanence ($M_{rs}/M_s$) plotted as a function of particle width for interacting samples compared to that for a non-interacting sample. The points for sample JG6 are explained in the main text.

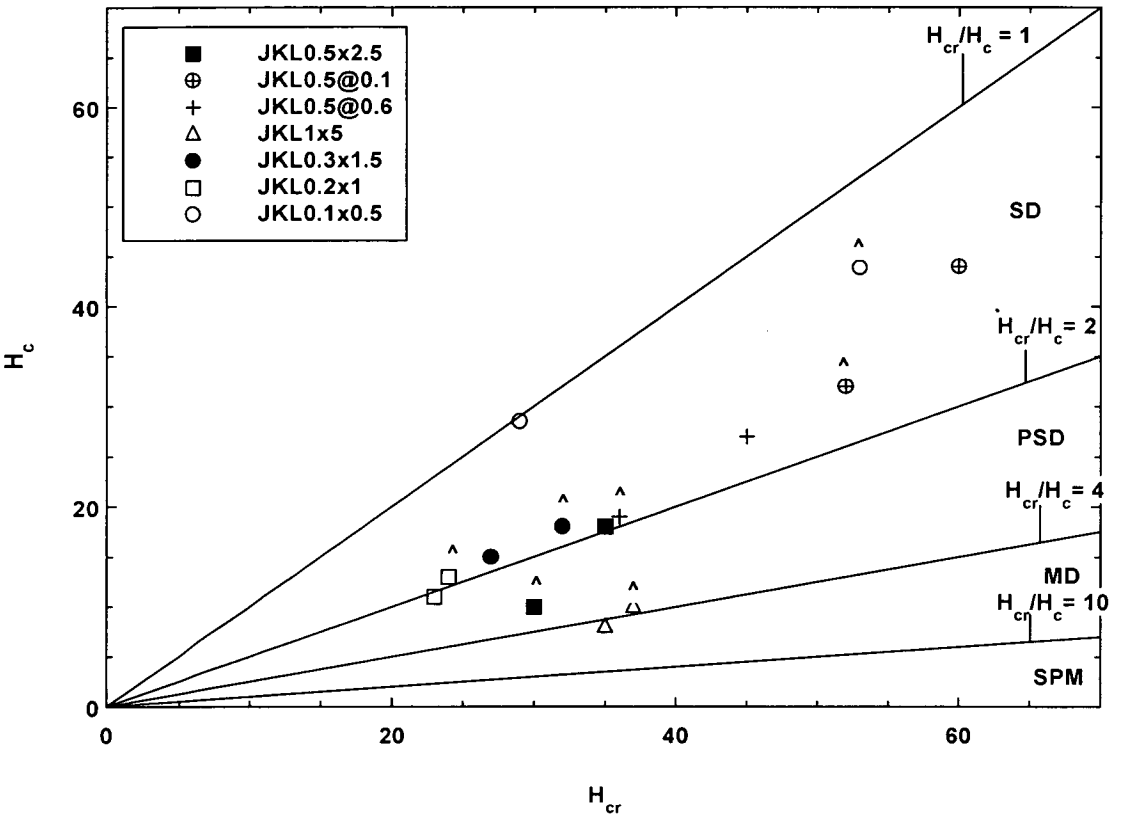


**Figure 7.15** A plot of the coercivity as a function of coercivity of remanence for lithographically produced rectangular parallelepiped magnetite particles. The plot shows domain state expected for these samples. The points marked with the symbol ^ on top were obtained with the field perpendicular to the particle's length.

## 7.9 Summary

Magnetic properties of rectangular parallelepiped magnetite particles are more complex than expected from the hypothetical domain configurations based on simple demagnetisation shape anisotropy contributions. According to such predictions, some of the particles used in this chapter should have been single domain as shown in Figure 7.7. But none of the samples exhibited magnetic properties consistent with SD particles. However, the magnetic properties observed were consistent with data obtained from 3-D micromagnetic calculations.

In contrast with magnetic results of ellipsoidal magnetite powders, interacting arrays of parallelepiped magnetite particles exhibit coercivities and remanences which are higher than those of non-interacting arrays. This inter-particle magnetostatic effect may perhaps partly explain observed high coercivities of magnetite/ilmenite intergrowths, such as those of Modipe gabbros of Botswana and magnetosome fossils.

# Chapter 8 Conclusions and suggestions for further work

## 8.1 Results summary

By utilising the electron beam lithography techniques, arrays of parallelepiped magnetite particles in the submicron size range were produced. The quality of these particles was checked by electron microscopy and XRD patterns. The magnetite particles were found to be of well defined parameters including inter-particle spacing, a task which cannot be achieved using magnetite powders often used in rock magnetic studies. The error in the dimensions was in general less than 5%. The XRD patterns obtained for thin magnetite films co-produced with these particles matched those for stoichiometric magnetite. A Curie temperature of $580^{o}$ +/- $12^{o}$ C measured for co-produced magnetite thin films is in good agreement with the literature value for stoichiometric magnetite.

A sharp drop of SIRM near 120 K was observed for the arrays of magnetite particles produced in this study and hence confirming the particles as stoichiometric magnetite. The observed relatively small drop in the SIRM lost at the Verwey transition for these samples compared to those for magnetite powders is most likely due to particle clumping in the latter. The observed particle dependence of the amount of SIRM lost at the Verwey transition for magnetite particles of this and other studies (e.g. Özdemir, et. al., 1993), may be a reflection of the vortex domain structure. Such a structure is predicted to occur in submicron grains greater than about 0.05 μm (e.g. Williams and Dunlop, 1989).

None of the unstressed samples exhibited any 'true' magnetic memory. In contrast, magnetic memory was exhibited by all stressed samples. This shows that magnetic memory is a stress related phenomenon. An increase in normalised saturation magnetisation at the Verwey transition was observed.

## 8.2 Application of study to paleomagnetism

In chapter 5, section 5.3 the amount of SIRM lost at the Verwey transition for stoichiometric magnetite samples was shown to be a function of grain size. The larger the grain size the bigger the SIRM drop at $T_V$. This

observed experimental result could be used to infer particle size of magnetite in rocks of paleomagnetic interest such as basalts and gabbros (Dunlop, 1983). In order to reveal fine magnetite particles in such rocks, paleomagnetists often crush and grind the samples (e.g. Bailey and Dunlop, 1983). Such a process often induce stresses in samples which results in high coercivities (see chapter 6, section 6.5).

The process of inferring particle size from the amount of SIRM lost at $T_V$ described above can also be applied to rocks which contain mixed grain sizes of magnetite. This could be achieved by observing the drop in SIRM at $T_V$ followed by heating the sample in air to about $400^o$ C (i.e. oxidising fine grained magnetite particles to hematite or maghemite) and again measuring the drop in SIRM at $T_V$. If a large drop in SIRM at $T_V$ is still observed after this process then the magnetite particles are large crystals (several microns in size).

According to Thompson and Oldfield, 1986, burning fires can convert non-ferrimagnetic iron minerals in soils to magnetite. The magnetite produced by this process is non-stoichiometric, and it may end up being part of lake sediments. In cases where the major paleomagnetic carriers in lake sediments is due to magnetosomes from bacteria fossils, it is possible to check if magnetite produced by burning of soils is present since non-stoichiometric magnetite exhibits lower than 120 K Verwey transition (see chapter 5, Figure 5.3).

In chapter 5, section 5.11, it was observed that 'true' magnetic memory is a stress related phenomenon. This observation could be useful in assessing changes in natural tectonic stresses important to earth quakes and volcanic eruption monitoring. In chapter 6, Figure 6.5, stressed samples were shown to exhibit higher coercivities than unstressed samples. Thus tectonic stresses could also be monitored by measuring coecivities of rock samples. Apart from being natural hazards, volcanic eruptions are important to paleomagnetic studies since it is during such eruptions that paloemagnetic field is recorded.

An increase in the saturation magnetisation measured when the sample was in a constant field of 1 T occurred at the Verwey transition. This transition may be used to identify the presence of magnetite in rocks. Such a method will have the advantage of not requiring an essentially field free environment as Verwey determination by measuring SIRM since it is a high field process. A less sophisticated equipment may be used the check if

there is an $M_S$ transition at $T_V$ since no magnetic shielding from transient fields associated with buildings (e.g. from lifts) is necessary.

## 8.3 Implications of thesis results on domain theory

The coercivities of arrays of cubic magnetite particles obtained in this study gradually decreases with increasing particle size (chapter 6, Figure 6.10). This observed behaviour is not consistent with the expected sharp transition in magnetic properties at the supposed one domain to two domain boundary predicted from theories based on hypothetical domain configurations (e.g. Kittle, 1949) or 1-D micromagnetic calculations (e.g. Einkin and Dunlop, 1987). However, in general, the magnetic properties of lithographically produced samples of this study are in good agreement with data obtained from 3-D micromagnetic calculations which shows that the mechanism of reversal of magnetisation is vortex nucleation and propagation (e.g. Williams and Dunlop, 1995).

The observation that stressed samples have higher coecivities than unstressed samples (chapter 6, Figure 6.10) means that magnetic domain structure of PSD magnetite particles can be changed by stress. Hence a magma intrusion which solidify to form igneous rocks composed of unstressed PSD magnetite particles (i.e. vortex mechanism of magnetisation reversal), could become SD (i.e. coherent rotation of atomic moments mechanism of magnetisation reversal) as a result of tectonic stresses. A rock which has been subjected to such stresses would give a false natural remanent stability since its coercivity at the time of formation of the rock (vortex domain structure) would not be the same as that obtained at the time of magnetic measurements (SD structure).

In chapter 7 it was observed that elongated magnetite particles which are supposed to be single domain according to domain boundaries calculated based on hypothetical domain configurations, exhibits magnetic properties which are contrary to this prediction. However, the magnetic properties were consistent with domain prediction from 3-D micromagnetic calculations of Fabian et al., 1996. The magnetic properties were consistent with the mechanism of magnetisation reversal described by Schabes, 1991, which involves nucleation of magnetic vortex at particle edges and then propagation of these vortex towards the particle centre.

## 8.4 Suggestions for further work

The arrangement of arrays of magnetite particles produced in this study was a two dimensional (2-D) array. The magnetic properties for a three dimensional (3-D) magnetite particle arrangement is not expected to be different from that of a 2-D arrangement for the non-interacting case. However for interacting particles, the magnetic properties for the 3-D case may be different from that of the 2-D case. A magnetite 3-D array arrangement may be produced using the electron beam lithography method by alternately depositing layers of Fe and a non-magnetic material before applying the lift-off process described in chapter 3.

Due to the difficulties encountered in attempting to produce suitable samples on silicon nitride membranes for domain observations with a TEM, it may be useful to try other membranes or other high resolution domain observation techniques such as MFM in further work since no thin membranes are required in the latter case.

The arrays of magnetite produced in this study can easily be converted to maghemite and hematite by annealing in air at the appropriate temperature. In addition the method of production of arrays of magnetite particles via the used of electron beam lithography can be used to produce titanomagnetites, titanomaghemites or titanohematites. This may be achieved by simultaneous evaporation of Fe and Ti from different crucibles (since these two elements have different melting points) followed by annealing in an appropriate environment.

# References


Abel, P.B., A.H. Heuer and R.W. Hoffman, Measurement of oxidation growth stress on thin iron films, **J. Vac., Sci., Technol., 1, 260 - 262, 1983.**

AlMawlawi, D., Coombs, N. and M. Moskovits, Magnetic properties of Fe deposited into anodic aluminium oxide pores as a function of particle size. **J. Appl. Phys., 70, 442-4425, 1991.**

Anderson, K.D. Leaver, R.D. Rawlings and J.M. Alexander, *Materials Science*, **The Thetford Press Ltd, 1985.**

Aragón, R., J.B. Buttrey, J.P. Shepherd and J.M., Honig, Influence of nonstoichiometry on the Verwey transition, **Phys. Rev. 31, 430-436, 1985.**

Argyle K.S., and D.J. Dunlop, Low -Temperature Hysteresis of small multidomain magnetites (215 - 540 nm), **J. Geophys. Res., 95, 7069 - 7083, 1990.**

Argyres, P.N., Theory of the Faraday and Kerr effects in ferromagnetics, **Phys. Rev., 97, 334-345, 1955.**

Bailey M. E. and D. J. Dunlop, Alternating field characteristics of pseudo-single-domain (2-14 μm) and multidomain magnetite, **Earth Planet. Sci. Letters, 63, 335-352, 1983.**

Bando, Y., S., Horrii, and T.Takada, Reactive condensation and magnetic properties of Iron oxide films, **J. J. Appl. Phys. 17:1037-1042, 1978.**

Belov, P.K., Electronic processes in magnetite (or, "Enigmas of magnetite"), **Physics-Uspekhi, 35, 380-391, 1993.**

Bickford, L. R., J. M. Brownlow, and R. F. Penoyer, Magnetocrystalline anisotropy in cobalt-substituted magnetite single crystals, **Proc. Inst. Electr. Eng., B104, 238-244, 1957.**

Bitter, F., On inhomogeneities in the magnetization of ferromagnetic materials, **Phys. Rev., 38, 1903, 1931.**

Bitter, F., Experiments on the nature of ferromagnetism, **Phys. Rev., 41, 507, 1932.**

Blakemore, R.P., Magnetotactic bacteria, **Science, 190, 377-379, 1975.**

Borrellie, N.F., S.L. Chen and J.A. Murphy, Magnetic and optical properties of thin films in the system $1\text{-}xFe_3O_4 \bullet xFe_{8/3}O_4$, **IEEE Trans. Magn., 8, 648-651, 1972.**

Brunhes, B., Recherches sur le direction d'aimantation der roches volcaniques, **J. Phys., 5, 705-724, 1906.**

Butler, R.F., and S.K., Banerjee, Theoretical single-domain grain size range in magnetite and titanomagnetite, **J. Geophys. Res., 80, 4049-4058, 1975.**

Chapman, J.N., The investigation of magnetic domain structures in thin foils by electron microscopy, **J. Phys., 17, 623-647, 1984**.

Creer, K.M., A.C. demagnetization of unstable triassic kenper marls from S.W. England, **Geophys. J. R. Astro. Soc., 2, 261-275, 1959.**

Creer, K.M., and C.B. Like, A low temperature investigation of natural remanent magnetisation of several igneous rocks, **Geophys. J. R. astr. Soc., 12, 301-312, 1967.**

Dahlberg, E.D. and J. Zhu, Micromagnetic microscopy and modelling, **Physics Today, 48, 34-40, 1995.**

Daiz Ricci, J.C., and J.L. Kirschvink, Magnetic domain state and coercivity predictions for biogenic greigite ($Fe_3O_4$): a comparison of theory with magnetosome observations, **J. Geophys. Res., 97, 17309-17315, 1992.**

Dankers, P. and N. Sugiura, The effects of annealing and concentration on the hysteresis properties of magnetite around the PSD - MD transition, **Earth Planet. Sci. Lett. 56, 422-428, 1981.**

David, P., Sur la Stabilitié de la Direction d'aimantation dans quelques Roches Volcaniques, C.R. **Acad. Sci. Paris, 138, 41, 1904.**

Davis, P.M. and M.E. Evans, Interacting single-domain properties of magnetite intergrowths, **J. Geophys. Res., 81, 989-994, 1976.**

Day, R., M. Fuller and V. A. Schmidt, Hysteresis properties of titanomagnetites: grain size and compositional dependence, **Phys. Earth Planet. Inter. 13, 260-267, 1977.**

Dunlop, D. J., Determination of domain structure in igneous rocks by alternating filed and other methods, **Earth Planet. Sci. Letters, 63, 353-367, 1983.**

Dunlop, D. J., Hysteresis properties of magnetite and their dependence on particle size: a test of pseudo-single-domain remanence models, **J. Geophys. Res., 91, 9569-9584, 1986.**

Dunlop , D. J., and K. S. Argile, Separating multidomain and single-domain-like remanences in pseudo-single-domain magnetites (215-540 nm) by low-temperature demagnetization, **J. Geophys. Res., 96, 2007-2017, 1991.**

Dunlop, D.J., The rock magnetism of fine particles, **Phys. Earth Planet. Inter., 26, 1-26, 1981.**

Dunlop, D.J., The hunting of the "psark", **J. Geomagn. Geoelectr., 29, 293-318, 1977.**

Dunlop, D.J., On the demagnetizing energy and demagnetizing factor of a multidomain ferromagnetic cube, **Geophys. Res. Lett., 10, 79-82, 1983.**

Dunlop, D.J., Özdemir, Ö., AlMawlawi, D. and M. Moskovits, Magnetic properties of arrays of oriented iron particles as a function of particle size, shape and spacing, **Phys. Earth Planet. inter., 76, 113-121, 1993.**

Enkin, R.J., and D.J. Dunlop, A micromagnetic study of pseudo-single-domain remanence in magnetite, **J. Geophys. Res., 92, 12 726-12740, 1987.**

Enkin, R.J., and W. Williams, Three-dimensional micromagnetic analysis of stability in fine magnetic grains, **J. Geophys. Res., 99, 611-618, 1994.**

Evans, M.E. and M.L. Wayman, An investigation of small magnetic particles by means of electron microscopy, **Earth Planet. Sci. Letters, 9, 365-370, 1970.**

Evans, M.E. and M.W. McElhinny, An investigation of the origin of stable remanence in magnetite-bearing igneous rocks, **J. Geomag. Geoelect., 21, 757-773, 1969.**

Fabian, K., Kirchner, A., Williams, W., Heider, F., Leibl, T. and A. Huber, Three-dimensional micromagnetic calculations for magnetite using FFT, **Geophys. J. Int., 1996.**

Feng, J.S.Y., C.H., Bajorek, and M.A., Nicolet, Magnetite thin films. **IEEE Trans. Magn., 8, 277-278, 1972.**

Ferris, F.G., T.J. Beveridge and W.S. Fyfe, Iron-silica crystallite nucleation by bacteria in a geothermal sediment, **Nature, 320, 609-611, 1986.**

Fujii T., Takano R. and Bando Y., Preparation and characterization (111) - oriented $Fe_3O_4$ deposited on Sapphire, **J. Appl. Phys., 66, 3168 - 3172. 1989**

Fujii T., Takano, M., Katano, R., Isozumi, Y. and Bando, Surface and interface properties of epitaxial $Fe_3O_4$ films studied by Mossbauer spectroscopy, **J. Magn. Magn. Mater., 130, 267 - 274, 1994.**

Gault, P., A magnetic study of precipitation in a gold-cobalt alloy, **Philos. Mag., 5, 1127-1145, 1960.**

Haigh, G., Observations on the magnetic transition in hematite at -15 $^{o}$C, **Phil. Mag., 2, 877-800, 1957.**

Halgedahl, S. and Fuller, M., The dependence of magnetic domain structure upon magnetisatization state with emphasis upon nucleation as a mechanism for pseudo-single-domain behaviour, **J. Geophys. Res., 88, 6505-6522, 1983.**

Hatzakis, M., Materials and processes for microstructure fabrication, **IBM J. Res. Develop., 32, 441- 453, 1988.**

Hefferman S.J., Chapman, J.N. and S. McVitie, In-situ magnetising experiments on small reguarly shaped permalloy particles, **J. Magn. Magn. Mater., 95, 76-84, 1991.**

Heider, F. and L. T. Bryndzia, Hydrothermal growth of magnetite crystals (1 μm to 1 mm), **J. Crystal Growth, 84, 50-56, 1987.**

Heider, F., D. J. Dunlop and H. C. Soffel, Low-temperature and alternating field demagnetization of saturation remanence and thermoremanence in magnetite grains (0.037 μm to 5 mm), **J. Geophys. Res., 97, 9371-9381, 1992.**

Heider, F., Dunlop, D.J., and Sugiura, N., Magnetic properties of hydrothermally recrystallised magnetite crystals, **Science, 236, 1287-1290, 1987.**

Heisenberg, W., On the theory of ferromagnetism, **Z. Physik, 49, 619, 1928.**

Henkel, O., Remanenzerhalten und Wecheselwirkungen in hartmagnetischen teilchenkollkiven, **Phys. Stat. Sol., 7, 919-924, 1964.**

Hodych, J.P., Evidence for magnetostrictive control of intrinsic susceptibility and coercive force of multidomain magnetite in rocks, **Phys. Earth Planet. Inter., 42, 184-194, 1986.**

Hoffmann, R., Schäfer, E. Appel, A., Hubert and H. Soffel, First domain observations with the magneto-optical Keer effect on Ti-ferrites in rocks and their synthetic equivalents, **J. Magn. Magn. Mater., 71, 90-94, 1987**.

Ishii, Y., Terada, Alshii, O., Ohta, S., Hattori, S. and K. Makino, A new preparation process for δ-$Fe_2O_3$, **IEEE Trans. Magn., 16, 1114-1116, 1980.**

Kim, Y.K. and M. Olivera, Magnetic properties of reactively sputtered $Fe_{1-x}$-O and $Fe_3O_4$ thin films, **J. Appl. Phys., 75, 431- 437, 1994.**

King, J.G., W. Williams, C.D.W. Wilkinson, S. McVitie and J.N. Chapman, Magnetic properties of magnetite arrays produced by the method of electron beam lithography, **in press.**

Kittel, C., Physical theory of ferromagnetic domains, **Rev. Mod. Phys., 21, 541, 1949.**

Kobayashi, K. and M. Fuller Stable remanence and memory of multid-domain materials with special references to magnetite, **Philos. Mag., 18, 601-624, 1968.**

Lax, B. and K. J. Button, Microwave ferrites and ferrimagnetics, **McGraw-Hill BookCompany, Inc., 1962.**

Levi, S., and R.T. Merrill, Properties of single-domain, pseudo-single-domain, and multidomain magnetite, **J. Geophys., Res., 83, 309-323, 1978.**

Levi S., and R. T. Merrill, A comparision of ARM and TRM in magnetite, ***Earth Planet. Sci. Lett. 32, 171-184, 1976.***

Lowrie, W., and M. Fuller, On the alternating field demagnetization characteristics of multidomain thermoremanent magnetization in magnetite, **J. Geophys. Res., 74, 2698-2710, 1969.**

Margulies, D.T., F.T. Parker and A.E. Berkowitz, Magnetic anomalies in single crystal $Fe_3O_4$ thin films, **J. Appl., Phys., 75, 6097-6099. 1994**

Margulies, D.T., F.T. Parker, F.E. Spada, R.S. Goldman, J. Li, R. Siclair and A.E. Berkowitz, Anomalous moment and anisotropy behaviour in $Fe_3O_4$ films, **Phys. Rev., 53, 9175-9187, 1996.**

Mercer I.F., *Crystals*, **British Museum, London, 1990.**

Merrill, R.T., Low temperature treatments of magnetite and magnetite-bearing rocks, **J. Geophys. Res. 75, 3343-3349, 1970.**

Morales, M.P., de Julián, C., González, J.M. and C.J. Sema, The effect of the distributionn of vacancies on the magnetic properties of $\delta$-$Fe_2O_3$ particles, **J. Mater. Res., 9, 135-141, 1994.**

Morin F. J., Magnetic susceptibility of $\alpha Fe_2O_3$ and $\alpha Fe_2O_3$ with added titanium, **Phys. Rev., 78, 819-820, 1950.**

Morrish, A.H., and L.A. Watt, Coercive force of iron oxide micropowders at low temperatures, **J. Appl. Phys., 29, 1029-1034, 1958.**

Morrish, A.H., The physical principles of magnetism, **John Wiley & Sons, Inc., 1965.**

Moskowitz, B. M., R. B. Frankel and D. A. Bazylinski, Rock magnetic criteria for the detection of biogenic magnetite, **Earth. Planet. Sci. Lett., 120, 283-300, 1993.**

Moskowitz, B.M., S.L. Halgedahl and C.A., Lawson, Magnetic domains on unpolished and polished titanomagnetite, **J. Geophys. Res., 93, 3372-3386, 1988.**

Muan, A. and E.F. Osborn, *Phase Equilibria among oxides in steel making,* **Addison-Wesley, Massachusetts, 1965.**

Nagata, T., K. Kobayashi and M.D. Fuller Identification of magnetite and Hematite in rocks by magnetic observation at low temperature, **J. of Gephys. Res., 69, 2111-2121, 1964.**

Néel, L., Some theoretical aspects of rock magnetism, **Adv. Phys., 4, 191-242, 1955.**

O'Reilly W., *Rock and mineral magnetism*, **Blackie & Son, Glasgow, 1984.**
Özdemir, Ö., D.J. Dunlop and B.M. Moskowitz, The effect of oxidation on the Verwey transition in magnetite, **Geophys. Res. Lett., 20, 1671-1674, 1993.**
Ozima M., M. Ozima and S. Akimoto Low temperature characteristics of remanent magnetisation of magnetite, **J. Geomag. Geoelec., 16, 165-177, 1964.**
Parry, L.G., Magnetic properties of dispersed magnetite powders, **Phil. Mag., 11, 303-312, 1965.**
Petersen, N., T. von Dobeneck and H. Vali, Fossil bacteria magnetite in deep-sea sediments from the South Atlantic Ocean, **Nature, 320, 611-615, 1986.**
Pulliam, G.R., Chemical vapor growth of single - crystal magnetic oxide films, **J appl. Phys. 38, 1120 - 1126, 1967.**
Radhakrishnamurty, C., S. D. Likhite, E. R. Deutsch and G. S. Murthy, A comparison of the magnetic properties of synthetic titanomagnetites and basalts, **Phys. Earth Planet. Inter., 26, 37-46, 1981.**
Sato, M., G. Nakajima, T. Namikawa and Y. Yamazaki, Magnetic properties and microstructures of $Fe_3O_4$-$\gamma Fe_2O_3$ intermediate state, **IEEE Trans. Magn., 26, 1825-1827, 1990.**
Schabes, M.E. and H.N. Bertram, Magnetization processes in ferromagnetic cubes, **J. Appl. Phys., 64, 1347-1357, 1988.**
Schabes, M.E., Micromagnetic theory of non-uniform magnetization processes in magnetic recording particles, **J. Magn.Magn. Mater., 95, 249-288, 1991.**
Schmidbauer, E. and N. Schembera Magnetic hysteresis properties and anhysteretic remanent magnetisation of spherical $F_34O_4$ particles in the grain size range 60-160 nm, **Phys. Earth Planet. Inter., 46, 77-83, 1987.**
Shigematsu, T., Ushigome, H., Bando, Y. and T. Takada Epitaxial growth of magnetite on rock salt by reactive evaporation. **J. Crystal Growth 50:**
Soffel, H.C., Aumüller, C., Hoffmann, V. and E. Appel, Three-dimensional domain observations of magnetite and titanomagnetites using the dried colloid SEM method, **Phys. Earth Planet. Inter., 65: 43-53, 1990.**
Stephenson, A., Distribution anisotropy: two simple models for magnetic lineation and foliation, **Phys. Earth Planet. Infer., 82, 49-53, 1994.**
Stoner, E.C. and E.P. Wohlfarth, Mechanism of magnetic hysteresis in heterogeneous alloys, 1948, **IEEE Trans. Magn., 27, 3475-3518, 1991.**

Strangway, D.W., Larson, E.E. and M. Goldstein, A possible cause of high magnetic stability in volcanic rocks, **J. Geophys. Res., 73, 3787, 1968.**

Sugimoto, T. and E. Matijevic, Formation of uniform spherical magnetite particles by crystallization from ferrous hydroxide gels. **J. Colloid and Interface Sci., 74, 227-243, 1980.**

Thompson R. and F. Oldfield, *Environmental magnetism,* **Allen & Unwin, London, 1986.**

Thomson, L.C., R.J. Enkin, and W. Williams, Simulated thermoremanent magnetisation, **J. Geophys. Res., 99, 603-609, 1994**.

Tsuno, K. and T. Taoka, Magnetic-field-free objective lens around a specimen for observing fine structure of ferromagnetic materials in a transmission electron microscope, **J. Appl. Phys., 22, 1041-1047, 1983.**

Vali, H., O., Förster, G. Amarantidis and N. Peterson, Magnetotactic bacteria and their magnetofossils in sediments, **Earth Planet. Sci. Lett., 86, 389-400, 1987.**

Verwey, E. J. W., Electronic conduction of magnetite ($Fe_3O_4$) and its transition point at low temperatures, **Nature, 144, 327-328, 1939.**

Wasilewski, P.J., Magnetic hysteresis in natural materials, **Earth Planet. Sci. Lett., 20, 67-72, 1973.**

Williams, W. and D.J. Dunlop, Simulation of magnetic hysteresis in pseudo-single-domain grains of magnetite, **J. Geophys. Res., 100, 3859-5871, 1995.**

Williams W., Hoffmann, V., Heider, F., Göddenhenrich, T. and C. Heiden, Magnetic force microscopy imaging of domain walls in magnetite, **Geophys. J. Int., 111, 417-423, 1992.**

WIlliams, W., and D.J., Dunlop, Three-dimensional micromagnetic modelling of ferromagnetic domain structure, **Nature, 337, 634-637, 1989.**

Wohlfarth, E.P., Relations between different modes of acquisition of remanence magnetization of ferromagnetic particles, **J. Appl. Phys., 29, 595-596, 1958.**